Aus dem Institut für Virologie
des Fachbereichs Veterinärmedizin
der Freien Universität Berlin

The role of a cholesterol consensus motif in HA and of an amphipathic helix in M2 for replication of influenza A virus

Inaugural-Dissertation
zur Erlangung des Grades eines
PhD of Biomedical Sciences
an der
Freien Universität Berlin

vorgelegt von
Bodan Hu
aus Hunan, Volksrepublik China

Berlin 2019
Journal-Nr.: 4161

Gedruckt mit Genehmigung
des Fachbereichs Veterinärmedizin
der Freien Universität Berlin

Dekan:	Univ.-Prof. Dr. Jürgen Zentek
Erster Gutachter:	PD Dr. Michael Veit
Zweiter Gutachter:	Prof. Dr. Benedikt Kaufer
Dritter Gutachter:	Univ.-Prof. Dr. Marcus Fulde

Deskriptoren (nach CAB-Thesaurus): Influenza A virus, hemagglutinins, sialidase, cholesterol, cell culture, mutations, polymerase chain reaction, SDS-PAGE, western blotting, immunofluorescence microscopy.

Tag der Promotion: 22.08.2019

Table of contents

List of figures

Abbreviations

aa	Amino acids
AChR	Acetylcholine receptor
AH	Amphipathic helix
ALPS	Amphipathic lipid packing sensor
APP	Amyloid precursor protein
β_2AR	β2-adrenergic receptor
CCM	Cholesterol consensus motif
CHO	Chinese hamster ovary cell
CPP	Cell-penetrating peptide
CRAC	Cholesterol recognition/interaction amino acid consensus pattern
CRM1	Chromosome region maintenance 1
CT	Cytoplasmic tail
DIG	Detergent-insoluble glycolipids complex
DMEM	Dulbecco's Modified Eagle Medium
DMSO	Dimethyl sulfoxide
DRM	Detergent resistant membrane
ENTH	Epsin N-Terminal Homology domain
FP	Fusion peptide
FCS	Fetal calf serum
FPV	Fowl plague virus
GPCR	G protein-coupled receptor
GPI	glycosylphosphatidylinositol
GUV	Giant unilamellar vesicles
HA	Hemaglutinin
HAT	Human airway trypsin-like protease
HEK	Human embryonic kidney cell
IAV	Influenza A virus
LUV	Large unilamellar vesicles
MβCD	Methyl-β-cyclodextrin
MDCK	Madin-Darby canine kidney cell
NA	Neuraminidase
NEP	Nuclear export protein
NES	Nuclear export signal
NP	Nucloprotein
NS1	Non-structural protein 1
PA	Polymerase acidic protein

PB1	Polymerase basic protein 1
PB2	Polymerase basic protein 2
PBR	Peripheral benzodiazepine receptor
PtdIns(4,5)P2	Phosphatidylinositol-4,5-bisphosphate
R18	Octadecylrhodamine B chloride
rER	rough Endoplasmic Reticulum
RNP	Ribonucleoprotein complex
TMD	Transmembrane domain
TSPO	Translocator protein
SUV	Small unilamellar vesicles
SP	Signal peptide
SRP	Signal recognition particle
UTR	Untranslated regions
VLP	Virus like particles
vRNA	Viral RNA
vRNP	Viral Ribonucleoprotein complex
WT	Wild type

Amino acids

A	Ala	Alanine	N	Asp	Asparagine
C	Cys	Cysteine	P	Pro	Proline
D	Asp	Aspartic acid	Q	Gln	Glutamine
E	Glu	Glutamic acid	R	Arg	Arginine
F	Phe	Phenylalanine	S	Ser	Serine
G	Gly	Glycine	T	Thr	Threonine
H	His	Histidine	V	Val	Valine
I	Ile	Isoleucine	W	Trp	Tryptophan
K	Lys	Lysine	X	Xaa	any random amino acid
L	Leu	Leucine	Y	Tyr	Tyrosine
M	Met	Methionine			

1 Introduction

1.1 Influenza A virus

Influenza A virus (IAV) belongs to the Orthomyxoviridae family. There are three other types of influenza viruses, influenza B, C and D virus, classified on the basis of antigenic differences in the nucleoprotein (NP) and the matrix protein (M1) (1, 2). This thesis mainly focuses on influenza A virus. Based on the antibody response to their two major surface glycoproteins, hemagglutinin (HA) and neuraminidase (NA), IAVs are further classified into 18 different HA subtypes (H1 to H18), and 11 different NA subtypes (N1 to N11) (3, 4). The recently identified HA subtypes (H17 and H18) and NA subtypes (N10 and N11) were isolated from bats while the other 16 HA and 9 NA subtypes all could be isolated from aquatic birds, the natural reservoir for IAVs. Nevertheless, IAVs can infect a broad range of other host species, including poultry, human, pigs, horses, cattles and seals. IAV is a major threat to human health, having resulted in several pandemics with millions of deaths (5). As a RNA virus, the error-prone RNA polymerases leads to a high mutation rate in the viral genome such that the virus can escape from neutralizing antibodies against the antigenic proteins HA and NA (antigenic drift). On the other hand, when one host cell is infected by two viruses, reassortment between 8 segments from different viruses could produce a completely new virus (antigenic shift) (1, 6). The continuing evolution due to antigenic drift and shift makes it difficult to produce effective vaccine or antiviral reagents to protect from infection.

1.1.1 Genome and structure

Influenza A viruses (Fig. 1.1) are enveloped viruses with a spherical or filamentous morphology (3). Spherical IAVs have an average diameter of 80-100 nm; the width of filamentous ones is similar, but the length varies greatly from 100 nm to several micrometer. They are segmented RNA viruses with eight negative-sensed single-stranded gene segments, which encode 10 or more proteins. The first three segments encode polymerase basic protein 1 (PB1), protein 2 (PB2) and polymerase acidic protein (PA), together forming the RNA-dependent RNA-polymerase complex. Nucleoprotein (NP), translated from segment 5, is surrounded by the viral RNA (vRNA), constituting the ribonucleoprotein complex (vRNP) together with the polymerase complex (7). The viral genome is protected by the matrix protein (M1) which is the product of the segment 7. Outside is the lipid bilayer derived from the host's cell membrane, which carries the three important membrane proteins: hemagglutinin (HA), neuraminidase (NA) and the proton channel M2. Hemaglutinin, a trimer and encoded by segment 4, binds to the receptor sialic acid on the cell surface and mediates membrane fusion in the endosome. Neuraminidase, a tetramer and translated from segment 5, cleaves the sialic acid to release progeny viruses from cell surface. The M2 protein, a tetramer and the product from a spliced mRNA of segment 7, functions as ion channel to transport proton from the endosome into virions leading to disassociation between the viral matrix protein (M1) and viral ribonucleoprotein complexes (vRNP) during virus entry. The last segment, using a similar scheme as segment 7, also encodes two proteins. The non-structural protein 1 (NS1) is the antagonist of host's antiviral innate immune response and the nuclear export protein (NEP) exports vRNPs out of the nucleus (3). A small amount of the latter protein is also found in the virions. In some subtypes, a second ORF in PB1 segment encodes another protein PB1-F2, which induces apoptosis and promotes viral polymerase activity. There are several additional proteins, such as PB1-N40, PA-X, PB-S1, NS3 and M42 encoded by some virus strains, but knowledge about their function is lacking (6). Among all the proteins incorporated into the virions, M1 is the most abundant protein, while HA is the most abundant in the membrane (4, 8).

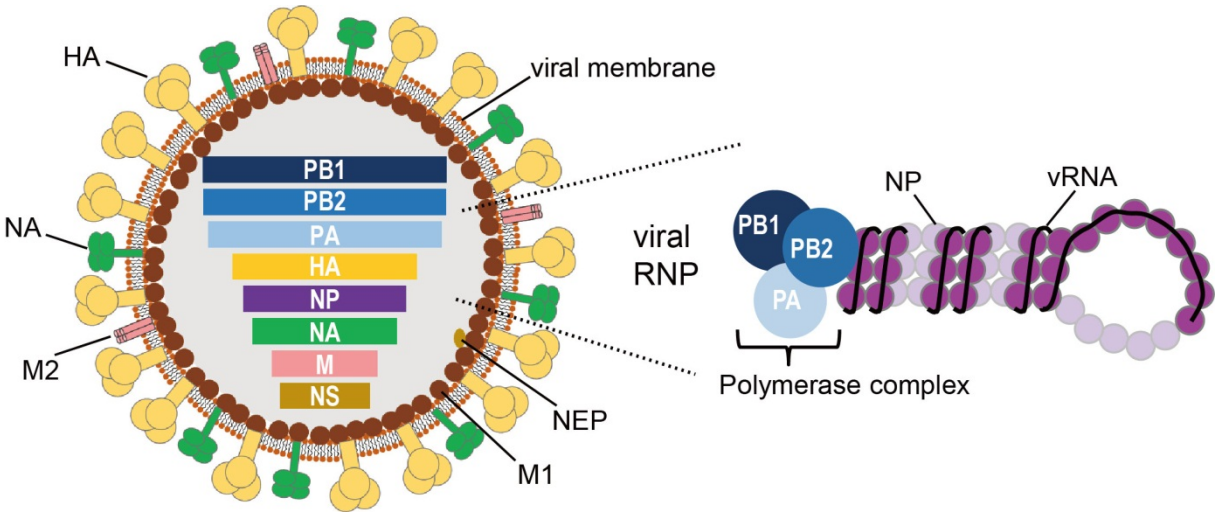

Fig. 1.1: Scheme of influenza A virus (a spherical one). Influenza A viruses are enveloped viruses with a genome of eight negative single-stranded gene segments, each encoding one or more proteins(1). Each individual segment is made up by the heterotrimeric polymerase complex [consisted of polymerase basic protein 1 (PB1), protein 2 (PB2) and polymerase acidic protein (PA)], viral RNA (vRNA), nucleoprotein (NP) that is loosely wrapped by the vRNA. The genome is protected by the matrix protein (M1). The outer layer is the viral membrane derived from host cells, which contains three integral membrane proteins, hemagglutinin (HA), neuraminidase (NA) and M2. HA is the most abundant membrane protein. Minor amounts of the nuclear export protein (NEP) are also incorporated into the virions (3), which is encoded by the segment NS together with non-structural protein 1 (NS1, not present in the virus particles).

1.1.2 Replication cycle

The replication of IAVs (Fig. 1.2A) starts when HA binds to the receptor, i.e. terminal sialic acid (SA) in a glycoprotein or glycolipid at the host cell surface. The presence of a suitable receptor is the first barrier for transmission across species (6). Human influenza A viruses mainly use α2-6 SA as receptor, which is present in the upper respiratory tract, while avian influenza viruses bind predominantly to α2-3 SA. In swine, both α2-3 and α2-6 SA are present in their trachea where IAVs establish infection. Therefore, they are considered as the mixing vessel for the possible reassortment of human and avian viruses, producing a new virus with high pathogenicity, which causes pandemic infection. After attachment to the receptor, viruses enter into host cells through endocytosis. In the late endosome, the acidic pH triggers the irreversible conformational change in cleaved HA, which mediates the membrane fusion between the viral and cellular membrane (details are described in 1.5) (9). The acidic pH also allows the ion channel of M2 to transport protons into virions for disassembly of the M1 layer and of the interactions between M1 and vRNPs (10). These two processes release vRNPs into the cytosol, which are then actively transported using the importin pathway into the host's nucleus for genome replication (4). In the nucleus, the viral mRNA is directly transcribed from the vRNPs by the viral RNA-dependent RNA polymerase complex. The protein components of vRNPs (NP, PB1, PB2 and PA) are firstly translated in the cytosol using the host's translation machinery and then transported back to the nucleus for further transcription of complementary positive-sensed RNAs, which are the intermediate templates for transcription of virus RNAs. The newly synthesized vRNA and the other four proteins form the vRNPs, which are exported from the nucleus through an interaction with the viral protein M1 and NEP (Fig. 1.2). NP plays an important role in maintaining the structure and stability of RNPs; without vRNAs NP plus the heterotrimeric polymerase complex is sufficient to assemble into the rod-shape RNP structure (7). The RNP binds to the C-terminus of the M1 protein, while the latter interacts with the protein NEP that contains a nuclear export signal (NES). The chromosome region maintenance 1 (CRM1) protein is then responsible for the nuclear export of the NES-containing RNP-M1-NEP complex (7). It is yet unknown whether vRNPs exit from nucleus separately or as a complex of two or more

segments. After exported from the nucleus, vRNPs are transported within the cytosol to the plasma membrane through the microtubule-dependent Rab11-mediated pathway (4).

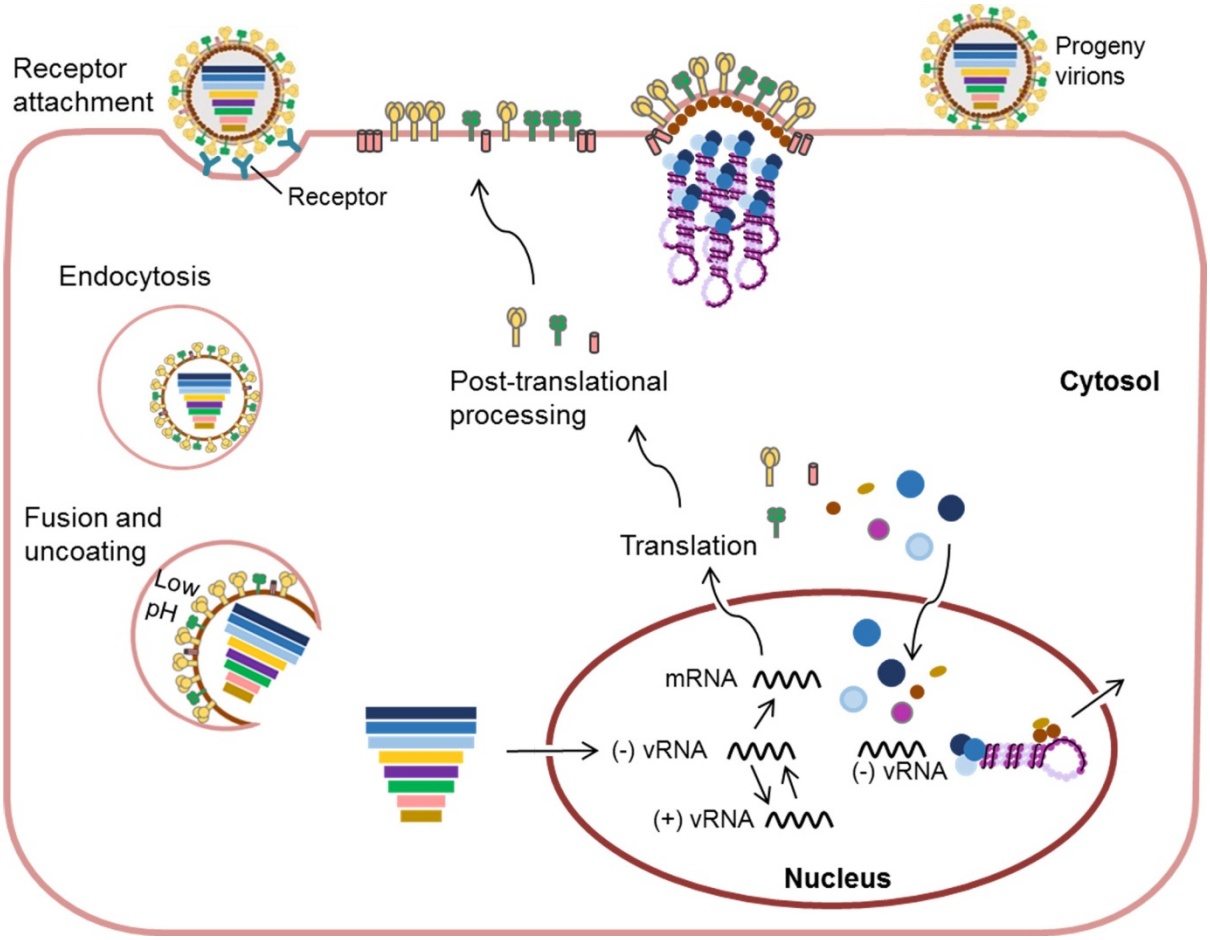

Fig. 1.2: Schematic replication cycle of influenza A virus. The replication cycle starts with virus attachment to the host cell through the binding of HA to the terminal sialic acid (α2-3 and α2-6 SA) in glycoproteins or glycolipids at the host cell surface(6). After entry into cells through endocytosis, the acidic pH of the late endosome triggers the fusion of endosomal and viral membrane and uncoating of the genome. The virus gene segments are released into the cytosol and translocated into the nucleus, where the genome replication happens(7). The viral RNA-dependent RNA-polymerase complex use the negative-sensed vRNAs as template for transcription of mRNAs and synthesis of complemented positive-sensed vRNAs. The latter are then used as template to synthesize new copies of vRNAs. The mRNAs are transported to the cytosol for translation of proteins, some of which are transported back into the nucleus for genome assembly (PB1, PB2, PA and NP). NEP and M1 are also translocated back to the nucleus to facilitate the export of newly assembled vRNPs into the cytosol (4). After translation, the membrane protein HA, NA and M2 undergo post-translational modification and are transported to the plasma membrane through secretory pathway. At the plasma membrane, HA and NA form clusters and initiate the assembly by recruiting other viral components. The eight segments assemble into a specific “1+7” configuration (13). The M2 is located to the edge of the budozone, mediating curvature formation and membrane scission (14). After budding, progeny virions remain attached to the host cells through binding to sialic acid on the cell surface, which is cleaved by NA to release progeny virions from cells.

The three membrane proteins are translated in the rough endoplasmic reticulum (rER), undergo post-translational modifications along the secretory pathway and are transported to the plasma membrane. The other viral proteins are translated in the cytosol and come to the plasma membrane for virus assembly and budding (details are described 1.6). Numerous studies suggest that the virus assembly and budding sites at the plasma membrane are nanodomains enriched in cholesterol and sphingolipids (also called “rafts”) (11, 12). The

accumulation of all the viral components at the assembly site alters membrane curvature and induces the formation of budding virions. Eight gene segments with distinct vRNAs are then selectively packaged into progeny virions. The eight segments assemble into a specific “1+7” configuration (13). After budding, the virus would remain bound to the cell surface due to the interaction between HA and sialic acid. However, the neuraminidase activity of NA cleaves all sialic acid residues from putative cellular receptors (6) (Fig 1.2).

1.2 Hemagglutinin

Hemagglutinin (HA) is a homotrimeric type I integral membrane protein encoded by segment 4. Each HA monomer has a large ectodomain, a short and flexible linker region, connected by one transmembrane domain (TMD) and a short cytoplasmic tail (CT) (Fig 1.3A) (15). Based on genetic homology HAs are divided into two subgroups, the first subgroup contains H1, H2, H5, H6, H8, H9, H11, H12, H13 and H16, the second group has H3, H4, H7, H10, H14 and H15 as members (16).

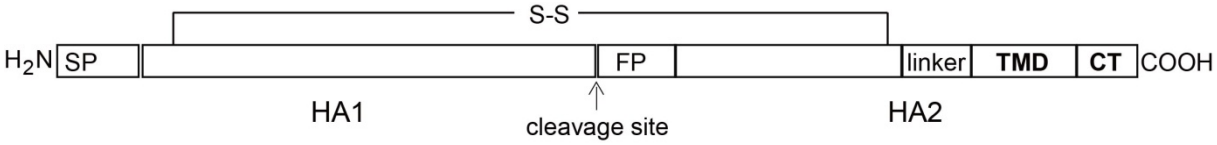

Fig. 1.3: The schematic structure of a HA monomer. The signal peptide (SP) is at the N-terminus, which is cleaved during processing. HA is also cleaved into two subunits, HA1 and HA2, which are linked by a disulfide bond. HA2 contains an N-terminal fusion peptide (FP), a linker region connecting the extracellular part to the transmembrane domain (TMD) and a short cytoplasmic tail (CT).

The HA protein is synthesized as a precursor HA0 which is directed to the lumen of rough endoplasmic reticulum (rER) through its N-terminal signal peptide recognized by signal recognition particle (SRP). The signal peptide is removed by the signal peptidase in the lumen of rER, whereas HA0 stays anchored to the membrane through its C-terminal hydrophobic region. Subsequently HA0 undergoes a series of modifications and is transported along the secretory pathway to the plasma membrane. In the rER the N-glycosylation sites of HA0 are filled with oligosaccharides which together with chaperones promote its proper folding. Misfolded HA0 is degraded while the completely folded ones assemble into a trimer and are released from the rER. S-acylation on conserved cysteine in the cytoplasmic tail happens *en route* to the cis-Golgi and the oligosaccharide chains are trimmed and then elongated to more complex glycans in the medial-Golgi and the trans-Golgi network (17).

To be fully functional, HA0 needs to be cleaved into two subunits, HA1 and HA2, but they remain linked by a disulfide bond (Fig. 1.3) (18). The cleavage site is at the arginine-glycine bond of a loop structure in the stem region of HA (Fig. 1.5A), but the sequence and size of the loop varies among IAV strains (18). A small loop with a monobasic cleavage site, predominantly an arginine (R), or rarely a lysine (K), is found in most virus strains. These HAs are cleaved by trypsin-like proteases that vary in strain specificities and expression level and distribution in tissue. Viruses having an HA with a monobasic cleavage site are low pathogenic in birds since virus replication is constricted to certain tissue with available enzymes. Cleavage of HA can happen within intracellular compartments as well as at the plasma membrane. In cell culture exogenous trypsin has to be added to the culture medium to facilitate the replication of influenza A virus with monobasic cleavage site. In contrast, a multibasic cleavage site, usually containing an R-X-R/K-R motif, exists in the highly pathogenic HA subtypes of H5 and H7. They are recognized by the proteases furin and PC5/6, which are ubiquitously expressed in host cells. The cleavage mainly happens in the TGN where the enzymes are preferentially located (19). Thus, virus with multibasic cleavage site can spread through all tissue, causing a systematic infection in poultry (“bird Flu”), which is usually fatal to host.

1.3 M2 protein

M2 of influenza A virus is a type III transmembrane protein and exists as a homotetramer in the viral membrane. Each monomer (Fig. 1.4) of M2 consists of a short N-terminal ectodomain (aa 1-24), a single-pass transmembrane domain (aa 25-43) and a long cytoplasmic tail (aa 44-97) which is highly conserved among virus subtypes (20). The membrane-proximal part of the cytoplasmic tail forms an amphipathic helix (aa 48-62) (21, 22).

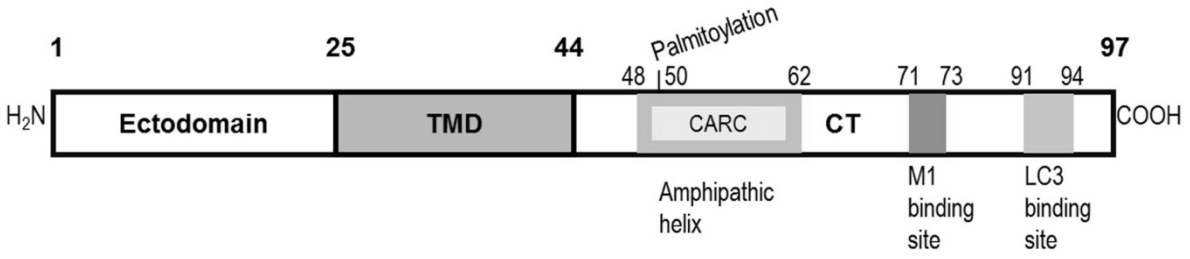

Fig. 1.4: Schematic structure of a M2 monomer. Each M2 monomer has a short ectodomain (aa 1-24), a single-span transmembrane domain (TMD, aa 25-43) and a long cytoplasmic tail (CT). An amphipathic helix (aa 48-62) is located at the N-terminal part of the CT. Within the region are the CARC motif and the conserved cysteine at positon 50 attached to palmitic acid. The C-terminal part contains a M1 binding site (aa 71-73) and a LC3 binding site (aa 91-94).

M2 is encoded by gene segment 7 together with M1 as a product of a spliced mRNA transcript. They share the same initiation codon for protein synthesis and the first 9 amino acid residues. M2 is synthesized at the late stage of the replication cycle (23) and the ratio of M2 mRNA to M1 mRNA increases during the infection process (24). Similar to HA, M2 is also synthesized at the ER and transported to the plasma membrane through the secretory pathway (25). During transport to the plasma membrane, M2 undergoes folding, tetramer formation and post-translational modifications. Two conserved cysteine residues in the ectodomain of M2 at position 17 and 19 form an intermolecular disulfide-bond, which is, however, not required for tetramer formation. Non-covalent interactions between the monomers is sufficient to stabilize the M2 homotetramer (26, 27). Another conserved cysteine at position 50 is attached to palmitic acid, which helps M2 insertion into cholesterol-rich nanodomains. Furthermore, several serine residues are modified with phosphate (20). The C-terminal part of the cytoplasmic tail contains a LC3 binding site (aa 91-94) and a M1 binding site (aa 71-73), whereas the N-terminal part possesses four repeats of potential cholesterol binding CARC motif (20). They will be discussed later.

1.4 The influence of cholesterol on membranes

Various studies suggest that the virus assembly and budding sites at the plasma membrane are nanodomains enriched in cholesterol and sphingolipids. Upon interaction with HA they are suggested to coalesce into a larger domain, providing a platform to recruit all the viral components and to promote their interactions (12). Quantitative lipid analysis by mass spectrometry verified that the envelope of influenza A virus contains higher content of cholesterol and sphingolipids than the plasma membrane of host cells (or apical membrane of polarized epithelial cells) (28). Thus, cholesterol is of significant importance to influenza A virus and I will give some introduction to cholesterol here.

Cholesterol is a major lipid component of the plasma membrane of animal cells. It is synthesized in the ER but is rapidly transported to the membrane of other organelles (29). The cholesterol amount in the cell increases along the secretory pathway, ~90% of cholesterol is in the mammalian cell surface whereas the other 10% are in internal membranes (30). The molar ratio of cholesterol to phospholipids in the ER is only 0.1, but it increases to 0.2 in the Golgi and reaches 0.5 in the plasma membrane (29). In polarized

epithelial cells the apical membrane has a higher cholesterol as well as glycosphingolipid content than the basolaterol membrane (31).

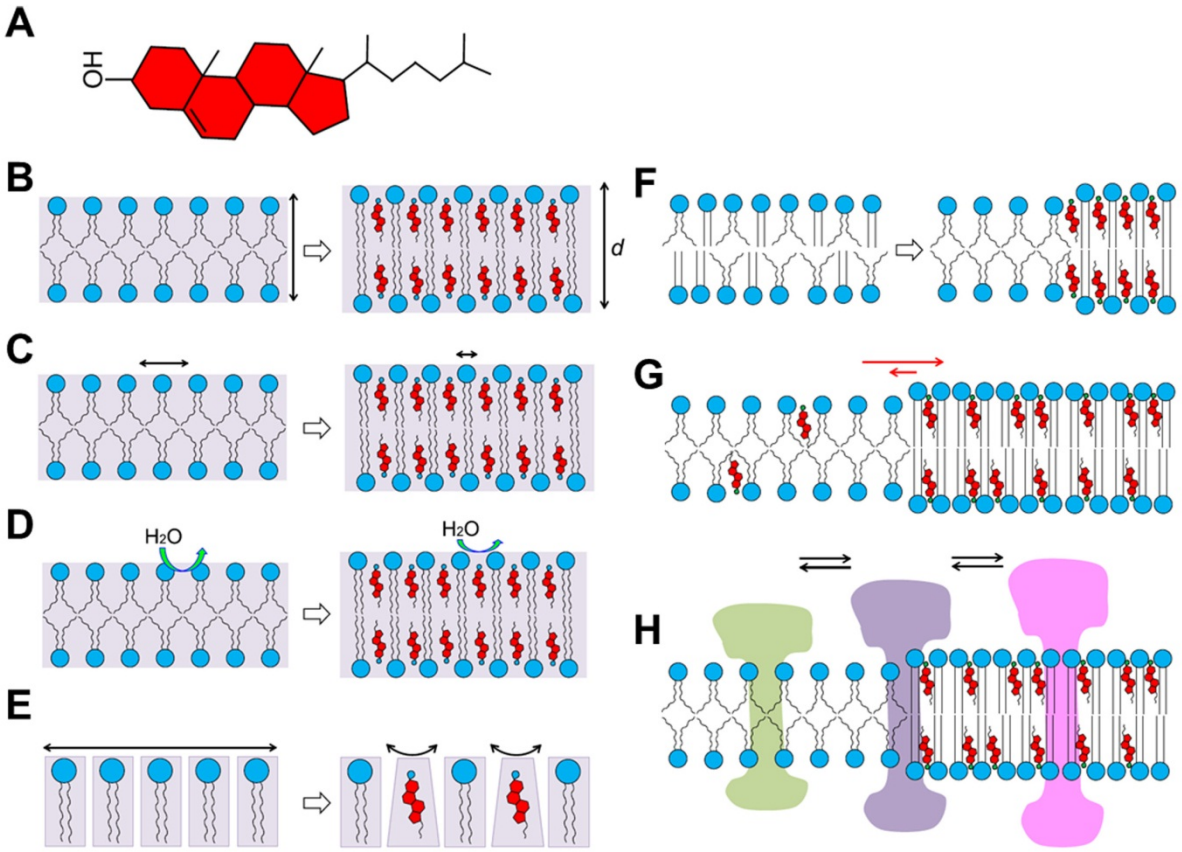

Fig. 1.5: The structure of cholesterol and its effects on lipid bilayers. Cholesterol **(A)** affects the thickness **(B)**, fluidity **(C)**, water penetration (hydrophobicity) **(D)**, and intrinsic curvature **(E)** of lipid bilayers. Cholesterol also induces phase separations in multicomponent lipid mixtures **(F)**, partitions selectively between different coexisting lipid phases **(G)** and causes redistribution of membrane proteins **(H)** in the bilayer. The figure is adapted from (34) with permission.

Cholesterol has a unique shape: a very small hydroxyl group is the hydrophilic head group, a rigid bulky steroid ring and a short hydrocarbon chain are the hydrophobic parts (Fig. 1.5A). It plays an important role in modifying the main properties of biological membranes. Lipids are not homogenously and symmetrically distributed in the membrane. They show phase behaviors with different spatial arrangement and motional freedom of each lipid in comparison to its neighbors (29). Phospholipids with unsaturated hydrophobic fatty acyl chains induce a liquid disordered phase characterized by fast diffusion and low acyl chain order. Sphingolipids tend to have a long and saturated hydrocarbon chain, therefore they are more likely to adopt a solid gel phase with slow movement and high chain order (32). Due to the small headgroup and rigid hydrophobic part, cholesterol interacts with phospholipids by locating its hydroxyl group in between the polar headgroups of phospholipids. Its steroid ring reaches the depth of the C9-C10 carbon atoms of the acyl chains of phospholipids, and the isooctyl chain is located in the membrane center (33). The insertion of cholesterol gives rise to a new phase, i.e. the liquid ordered phase, with relatively high diffusion and high chain order (Fig. 1.5F) (32). In fact, in model membranes two types of phospholipids together with cholesterol are able to induce the coexistence of two phases, liquid disordered and ordered (29, 32). Cholesterol preferentially binds to lipids having saturated acyl chains and the hydroxyl group can form hydrogen bond with the amide of sphingolipids (34). Such raft domains enriched in cholesterol and sphingolipids are supposed to exist in the plasma membrane due to their high content. The phase formation and different membrane domains in the membrane affect the diffusion and distribution of lipids and membrane proteins, and

accordingly membrane associated process and protein functions (34). When inserted into the lipid bilayer, cholesterol straightens the neighboring lipid acyl tail and thus increases the membrane thickness (Fig. 1.5B).

On the other hand, the biological membrane shows fluidity and the lipids and proteins are in constant motion. Cholesterol affects the membrane fluidity by its insertion more into the membrane surface or center (33) (Fig. 1.5C). In a similar mechanism, it also modulates the membrane hydrophobicity (or water penetration through membrane) (Fig. 1.5D). Cholesterol also induces membrane negative curvature due to its shape, a small hydrophilic head group but a large hydrophobic tail (Fig. 1.5E). These properties makes cholesterol involved in membrane associated activities, such as clathrin- and caveolin-mediated endocytosis, membrane fusion and scission (35).

1.5 Cholesterol binding motifs in proteins

Although less than a handful of viral proteins have been reported to bind to cholesterol, many cellular cholesterol-binding proteins have been characterized. In 1998 Li and Papadopoulos demonstrated that translocator protein (TSPO) may function as a channel to transport cholesterol from the outer to the inner mitochondrial membrane (36). Through sequence comparison with other TSPOs and cholesterol binding proteins, they proposed a cholesterol recognition/interaction amino acid consensus pattern (CRAC) responsible for recognizing cholesterol (one example shown in Fig. 1.5A). The CRAC pattern is L/V-X_{1-5}-Y-X_{1-5}-R/K and therefore consists of three groups of amino acids: neutral, apolar amino acids, such Leucine (Leu, L) or Valine (Val, V), interacting with the hydrophobic side chain of cholesterol; a neutral and polar residue, such as Tyrosine (Tyr, Y), interacting with cholesterol polar hydroxyl group; a basic amino acid, such as Arginine (Arg,R) or Lysine (Lys, K), probably helping to create a pocket. Since this motif is not highly strict in its composition, it exists in many proteins, such as the viral protein gp41 of human immunodeficiency virus (HIV-1) (37) and M2 of influenza A virus (38). But not all the motifs found in proteins are directly involved in binding to cholesterol (39). In 2011 Baier et. al. reported an inverted CRAC motif (K/R)-$X_{1–5}$-(Y/F)-$X_{1–5}$-(L/V), thus called CARC motif, in the transmembrane domain of a subunit of the nicotinic acetylcholine receptor (AChR) (40). Although they also found CRAC motif in the AChR subunits, they claimed that the CARC is more likely to bind cholesterol. Results from molecular modeling suggest three cholesterol molecules could be on the TMD of each AChR subunit. Similar to CRAC, the CARC motif is also common in proteins such as members of the Cys-loop family and of F-protein coupled receptors family. However, there is very limited value in prediction of cholesterol binding by either CRAC or CARC motif, since only 2 out of 20 proteins from the protein data base with an available crystal structure show association with cholesterol through this motif (41). In addition, Palmer showed that the CARC motif appears more than 5000 times in the proteome of a bacterium which has no cholesterol (42).

Sanders' group found that the C99 protein, a β-secretase-cleaved product of the amyloid precursor protein (APP) and the precursor of amyloid-β polypeptides that are associated with Alzheimer's diseases, interacts with cholesterol (43). The cholesterol-binding pocket locates at the extracellular end of the TMD together with the N-helix and N-loop, both adjacent to the TMD. Although there is no high-resolution structural data of C99 bound with cholesterol, they performed alanine scanning mutagenesis in these region and showed that certain amino acids are essential for cholesterol binding. Given that mutation at each glycine of the motif $G_{700}XXXG_{704}XXXG_{708}$ severely affect cholesterol binding, they speculate this motif is highly important for association of C99 with cholesterol. It creates a flat surface for cholesterol docking at this site through Van der Waals forces and entropy (Fig. 1.6B).

Another cholesterol binding motif, the "cholesterol consensus motif", is conserved in G protein-coupled receptors (GPCRs) (45). It was discovered when structural analysis showed that cholesterol was packed into crystals of the human β_2-adrenergic receptor (β_2AR) (Fig. 1.6C). In this structure, the aromatic Try158 interacts with the sterol ring of cholesterol through CH-π interaction. The hydrophobic Ile154 interacts with the sterol rings A and B

through hydrophobic interaction. The basic Arg151 forms hydrogen bonds with the hydroxyl group of cholesterol. Tyr70, from another helix, interacts with the sterol ring A through van der Waals interaction. After sequences comparison between G protein-coupled receptors, the CCM motif was defined as R/K-X_{2-6}-I/V/L-X_3-W/Y on one helix and F/Y interacting with cholesterol from another helix, although the latter contributes the least binding energy. The strict CCM motif is found in over 21% of human class A GPCRs. However, 44% of human class A GPCRs contain the relaxed form that excludes the F/Y which contributes very little to cholesterol binding (45).

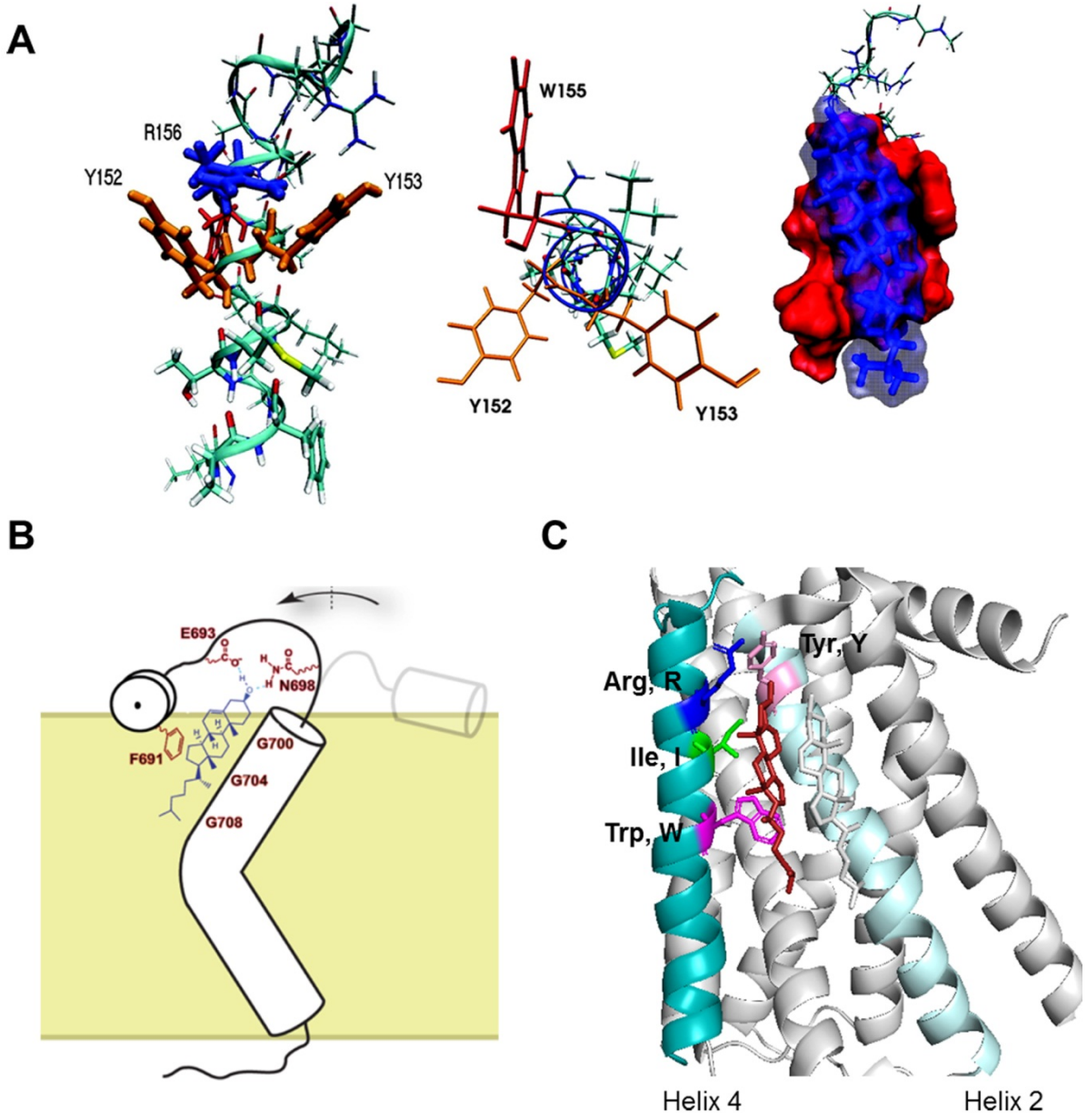

Fig. 1.6: Cholesterol binding motif. (A) The CRAC motif in a translocator protein (TSPO). Side (left) and top (middle) view of a TSPO peptide containing the CRAC and the docking model (right) of cholesterol to the CRAC domain. This figure (A) is adapted from (44) with permission. **(B)** Rough model for the proposed cholesterol binding to GXXXG motif in C99 protein and its related conformational change in C99. This figure (B) is modified from (41). **(C)** The CCM motif in human β_2ARdrenergic receptor. The Arginine (dark blue), Isoleucine (green) and Tryptophan (violet) are indicated and located in the helix 4 (light blue) binding to a cholesterol (red) from the same direction. The Tyrosine (pink) is located in the helix 2 (cyan), contributing the binding energy from the other side. The other five helices and another cholesterol are gray. This figure is generated with Pymol. (PDB: 3D4S).

Although CCM differs from CRAC or CARC in the linear sequence, the amino acids contacting cholesterol are quite similar, i. e. a positively charged residue and hydrophobic and aromatic residues.

1.5 Virus entry

1.5.1 HA and cholesterol in virus entry

HA plays an important role in virus entry since it mediates receptor binding and membrane fusion. The 3D structure reveals that the HA1 subunit forms a globular head of antiparallel β-sheet (15) (Fig. 1.7A). The receptor binding site is a shallow depression at the top of the globular head, which is constituted of amino acids conserved among all subtypes of influenza virus (46) (Fig 1.7B). Neutralizing antigenic epitopes are found in the membrane distal HA1 surface, one covers the receptor binding site (18). But constant amino acid substitutions in HA occur during evolution, preventing virus neutralization by antibodies.

The extracellular part of HA2 folds into a short and a long α-helix (15) (Fig. 1.7A). In the trimeric structure, the three long helices pack together as a triple-stranded coiled-coil, which stabilizes the trimer (Fig. 1.7B). The hydrophobic region at the N-terminus of HA2 is the fusion peptide, which is buried inside the molecule at neutral pH (Fig. 1.7F). After entry into the cells through endocytosis, the low pH of late endosomes activates the HA-mediated membrane fusion activity. The fusion pH triggers an irreversible conformational change in the HA, which expose the fusion peptide, while maintaining the structure of the HA1 receptor binding domain (47). The long helix of the HA2 stem domain extends by recruiting at least 36 additional residues to deliver the fusion peptide over 100 Å from its previous position, thus inserting into the target membrane (Fig. 1.7C). Since the C-terminal transmembrane domain of HA2 still inserts inside the viral membrane, the HA2 forms the bridge between viral and target membrane, which is designated as “pre-hairpin” structure (Fig. 1.7F) (9, 18). The HA2 trimer would then fold back to bring the two membranes in close proximity to form a hemifusion stalk where only the outer layer of the membranes are in contact. The trimer collapses further with the ectodomain parallel to the membranes creating a hemifusion diaphragm where the two outer leaflets fuse already while the inner leaflets contact each other. This process seems to be very fast (could be within 1 minute), so it is difficult to obtain the structure of the intermediates. However, with cryomicroscopy, the snapshot of hemifusion stalk and hemifusion diaphragm with HA parallel to the membrane have been observed (48, 49). Afterwards, the collapse of HA completes and the fusion peptide and the transmembrane domain form a 6-helix bundle. This drives the mixing of two inner leaflets to form a fusion pore, which expands wider during the fusion process so that vRNPs are released into the cell cytosol to start viral genome replication. One question would be how many HA trimers participate in this fusion process. Data from single virus fusion suggested that three to four neighboring HA trimers are needed for a successful fusion (50), while snapshots from cryomicroscopy revealed 6-8 HA trimers are involved in the fusion pore formation (48).

The C-terminal transmembrane domain of HA also contributes to membrane fusion. When HA is anchored in the membrane via a glycosylphosphatidylinositol (GPI) tail instead of its transmembrane helix, it only promotes hemifusion but is not able to mediate full fusion (51). Further analysis revealed that a TMD of 17 amino acids is required to efficiently induce the formation of a fusion pore (52). The linker region, which connects TMD to the ectodomain also affects HA fusion activity. To maintain efficient membrane fusion, the linker region can tolerate relatively small deviations in length with insertions or deletions of at most eight residues (53). A recent cryo-EM structure for the first time revealed the structure of the TMD of a H1 subtype HA and the flexible linker which connects the former to the ectodomain (Fig. 1.7D+E) (54). The helical bundle of TMD adopts different orientation, either straight following the symmetry axis of the ectodomain (Fig. 1.7D) or tilted with a minor to large angle (20-52°) (Fig. 1.7E). In line with this, the linker region also exhibits different orientation and structure, the flexibility of which might be important to facilitate the substantial refolding event of HA at

low pH.

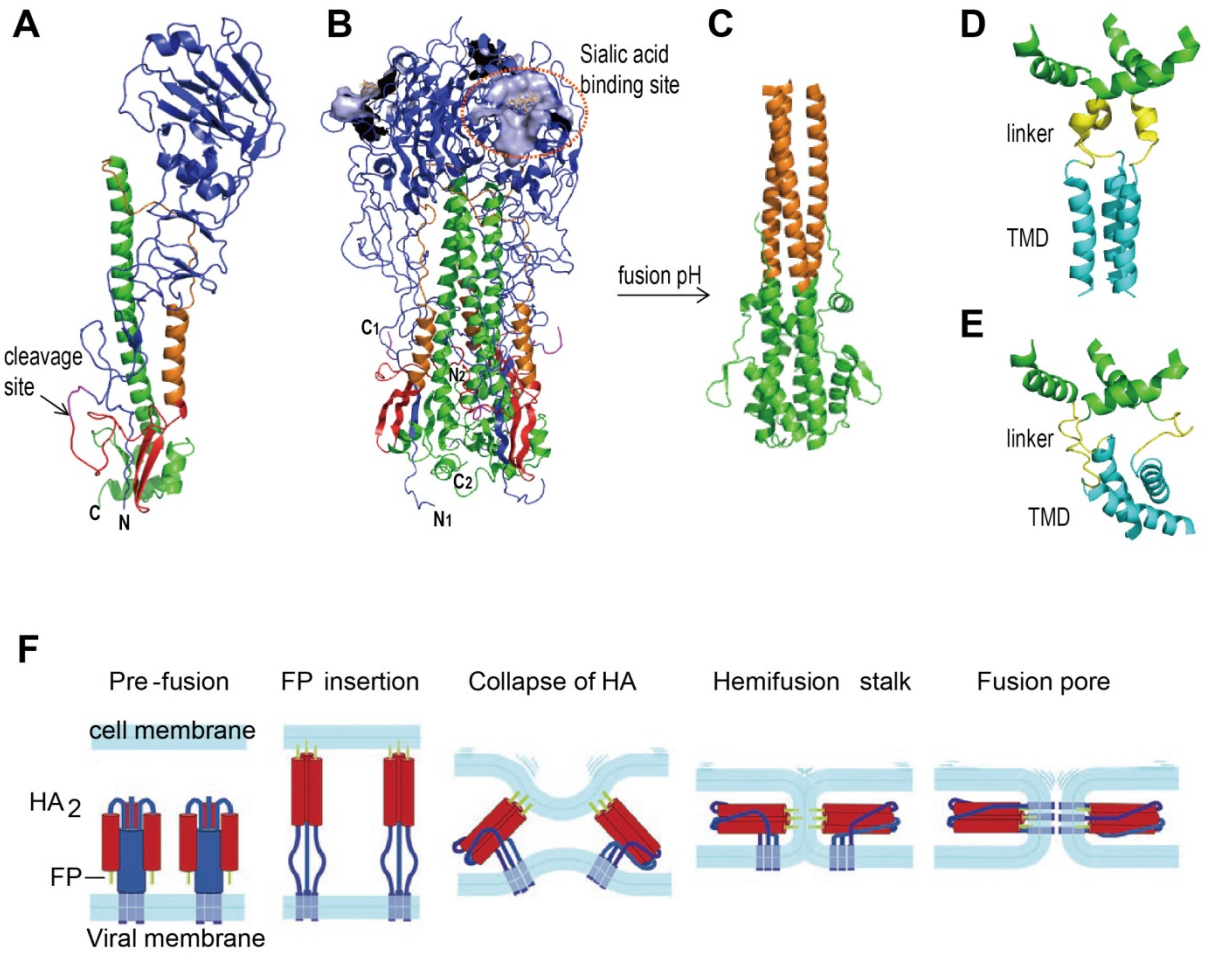

Fig. 1.7: 3D structure of hemaglutinin and the scheme of HA-mediated membrane fusion. **(A)** Uncleaved monomeric precursor HA0 without TMD and CT. The cleavage site is indicated. (PDB: 1HA0) **(B)** Cleaved HA trimer. HA1 is colored with blue and the encircled region is the sialic acid binding site bound with a receptor analogue. The part corresponding to FP is red, the HA2 stalk is shown in green and orange (PDB: 1HGE). **(C)** HA2 structure at the pH of fusion. The color scheme is the same as (B) (PDB: 1HTM). **(D)+(E)** Structure of the linker region (yellow) and 19 aa of the TMD (cyan) of a H1 subtype HA. One has a straight TMD following the symmetry axis of the ectodomain (E, PDB: 6HJQ) and the other tilted (F, PDB: 6HJR). Figures A-E are generated with Pymol. **(F)** HA-mediated membrane fusion in the endosome. Before fusion, the fusion peptide (FP) at the N-terminus of HA2 is hidden inside the stalk structure. After lowering the pH, the FP is released and inserts into the endosomal membrane, which forms a bridge between viral and target membrane. The extended intermediate then collapses, pulling the two membranes in close proximity. This is followed by the formation of hemifusion stalk where the outer layers of both membranes are in contact. Further collapse of HA drives the formation of a fusion pore and the FP and TMD of HA2 form a 6-helix bundle. The figure (F) is adapted from (9) with permission.

The cytoplasmic tail plays a role in fusion pore formation. The S-acylation at the conserved cysteine of cytoplasmic tail is essential for full fusion of a H7 subtype HA (55). On the other hand, the HA chimera with CT from other proteins showed defects in fusion pore formation or pore enlargement (56, 57).

Fusion requires the dramatic bending of two membranes to merge into one bilayer, thus lipids with an intrinsic curvature, i.e. those with a small headgroup but a large tail (or vice versa), would largely affect membrane fusion. As described before cholesterol has negative

curvature, therefore it might move to bended regions to stabilize highly curved fusion intermediates. In fact, the importance of cholesterol in membrane fusion has been reported. Various studies support that the presence of cholesterol is required for entry into cells of enveloped viruses, such as HIV-1, HCV and influenza A virus (34, 58, 59). Evidences supporting a direct effect of cholesterol on HA-mediated membrane fusion have also been obtained. Chlanda et.al demonstrated that cholesterol prevented unphysiological ("leaky") fusion reactions; high cholesterol concentration decreased the frequency of membrane rupture during fusion (60). Domanska et.al. reported that cholesterol levels in the viral membrane cause different effects on fusion kinetics. Strong depletion of cholesterol slows down the fusion rate, whereas moderate depletion speeds up the process (61). The latter is highly likely due to the increase of HA's lateral density in the viral membrane, since cholesterol depletion decreases the space between HA trimmers (62). On the other hand, their group as well as Zimmerberg's group (63) showed evidence that increasing cholesterol content in the membrane promotes both hemifusion (lipid mixing) and full fusion (content mixing). Cholesterol is suggested to act at two stages of membrane fusion (63): 1) at the earlier lipidic stage prior to the opening of a fusion pore, where the spontaneous negative curvature and head group condensation property of cholesterol could play an important role, promoting the contact between two lipid monolayers and stabilizing the pre-pore structure; 2) at the later fusion pore expansion stage, where the existence of cholesterol might decrease the fluid membrane viscosity to allow higher mobility of HA in the membrane.

1.5.2 The role of M2 in virus entry

M2 plays a role in virus entry due to its proton channel activity. The acidic pH in the endosome activates the proton channel to mediate the influx of protons from endosome into virions (10). This disrupts the interaction between M1 and vRNPs, so vRNPs are no longer encapsided by M1. Structure analysis of M2 revealed that the proton channel is formed by the tetrameric transmembrane helices (aa 21-43) (Fig. 1.8). It is also the target of the antiviral agents amantadine and rimantadine, which block the ion channel activity, hence inhibiting virus replication. Structure data obtained from different methods, such as solution NMR (21), solid state NMR (64, 65) and X-ray diffraction (66) showed that four transmembrane helices of M2 assemble into a left-handed parallel bundle. The N-terminal half of the helix tilts 30-35° in most cases, while the C-terminal half differs in the tilt angle of 10° between low pH and high pH (67). The heart of acid activation and proton conductance in M2 is the tetrameric His37-Trp41 cluster (Fig. 1.8). At neutral pH, the proton channel is locked by the histidine tetrad. At acid pH, the high concentration of proton leads to orientation changes of His37, to exchange protons with the surrounding water molecules and conduct proton inwards into the virions. Trp41 acts as the proton gate, which opens up due to the transient conformational change at acidic pH so that protons diffuse into virions.

M2 has a long cytoplasmic tail (CT), but the C-terminal end of the CT has no effect on proton channel activity (68). Structural data of M2 reveals that the N-terminal part of the CT, which is just next to the transmembrane ion channel forms an amphipathic helix (AH, aa 48-62) oriented parallel to the membrane (Fig. 1.8) (22, 65). The post AH part of the CT adopts a dynamic random coil at the membrane surface, which is not sensitive to the lipid composition (69). Studies (70) trying to identify the functional core of the proton channel reported that the fragment 21-61 maintains the full proton transport activity. Residues 21-51, transport protons at 50% reduced rates compared to full-length M2's activity. Alanine substitution of five hydrophobic residues in the C-terminal helix does not reduce the full proton channel activity of fragment 21-62 (70). Nor do any two mutations of these five residues affect the proton transport activity of full length M2 (71). These suggest that the interchain or helix-membrane association for this C-terminal helix does not affect transmembrane's proton channel function. However, the presence of the amphipathic helix has been suggested to stabilize the structure of transmembrane tetramer by insertion into the membrane (21, 70). Indeed, a trunctated M2 without this region showed severe reduction in proton transport (68). Although M2 is abundantly expressed in host cells, but only a few molecules are incorporated into virions

(72). This indicates that only a small number of M2 molecules are sufficient to transport protons for efficient virus replication.

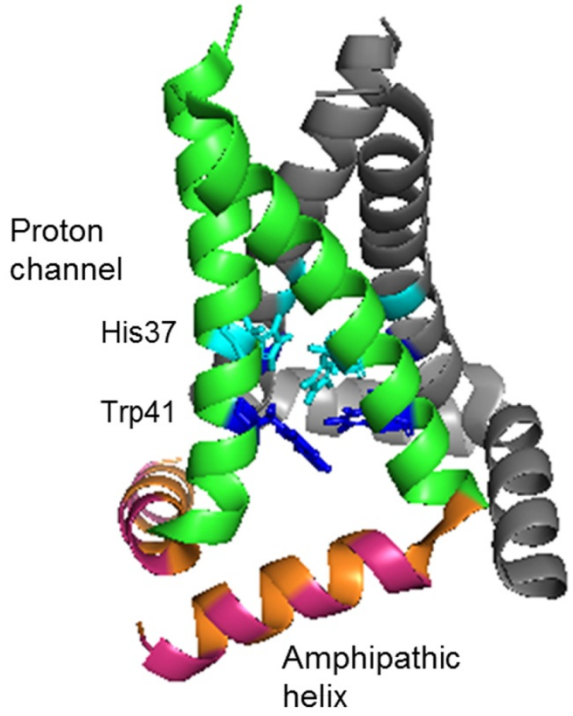

Fig. 1.8: NMR structure of M2 domain (aa 22-62) in a lipid bilayer. Two of the tetrameric helices (the proton channel) in front are colored in green. The two residues His37 (cyan) and Trp41 (blue) forming the heart of the proton channel are indicated. The amphipathic helix in the N-terminal of cytoplasmic tail is colored with orange. The charged residues at the hydrophilic side are in pink. This figure is generated with Pymol (PDB: 2L0J).

1.6 Virus assembly and budding

1.6.1 The role of HA in virus assembly and budding

IAVs assemble at and bud from the plasma membrane of infected cells, in polarized epithelial cells specifically from the apical membrane. In the plasma (apical) membrane, the assembly and budding site of influenza viruses are rafts, nanodomains enriched in cholesterol and sphingolipids. They coalesce into a larger domain, providing a platform to recruit all the other viral components and to promote their interactions (12). These nanodomains are defined by their insolubility in cold nonionic detergent (73). Indeed, the detergent resistant membranes (DRMs) are isolated from the viral membrane of some enveloped viruses, such as influenza A viruses (73) and HIV-1 (74). Their envelope contains high amount of cholesterol and sphingolipids. Furthermore, their amount is even higher than that in the plasma membrane of host cells, whereas some non-raft viruses such as Semliki forest virus and vesicular stomatitis virus have a lipid composition that highly resembles the host cell plasma membrane (35). The cholesterol amount in the viral membrane of influenza A viruses determined by quantitative lipid analysis is around 52% mol of total lipids, which is higher than in the apical membrane (~45%) of polarized MDCK cells and much higher than in total membranes (~28%) of MDCK cells (28).

It is widely accepted that the assembly process is initiated by HA located in raft domains, since this major membrane protein can be isolated from DRMs. HA's association with membrane rafts was also observed when using fluorescence resonance energy transfer (FRET) to analyze the association between a HA-Cer (cytoplasmic tail of HA fused with the fluorophore Cerulean) and Myr-Pal-YFP, an established raft marker (75). Furthermore, HA is not randomly distributed at the cell surface, but accumulated in clusters with different sizes (58). Fluorescence photoactivation localization microscopy (FPALM) revealed that the size of HA clusters varies from 40nm up to several micrometer, covering the size range of pleomorphic virus particles (76). Co-cluster of HA with other viral proteins such as M2 and NP were observed by immunogold staining of planar membrane sheets from infected cells

(77). Furthermore, expressing HA alone could induce formation of virus like particles (VLPs) (78).

The transmembrane domain (TMD) and cytoplasmic tail (CT) of HA are important for virus assembly and budding. Hemagglutinin contains two signals for association with nanodomains enriched in cholesterol. On the one hand, the three conserved S-acylated cysteine residues, one located at the cytoplasmic end of the TMD and the other two in the cytoplasmic domain (75). On the other hand, the hydrophobic amino acids in the TMD facing the outer leaflet of the plasma membrane, especially the conserved amino acids VIL at the beginning of the TMD (58). The latter were identified by alanine scanning mutagenesis throughout the whole TMD of HA to identify residues that confer incorporation of HA into DRMs. Alanine substitution of residues at the beginning of TMD also decreased HA association with cholesterol-enriched raft domains observed by FRET with a double-acylated raft-marker (79). Previous work in our lab has identified a cholesterol consensus motif (CCM) in phylogenetic group 2 HAs, which includes the hydrophobic residue Leucine of VIL (80). The CCM is composed of four amino acids Y-K-L-W and they are located in two transmembrane helices of the HA trimer, which is similar to the one found in human β2-adrenergic receptor (45). According to this idea (which is one part of my work) the basic amino acid arginine (K) should interact with the hydroxyl group of cholesterol. The hydrophobic Leucine (L) and the aromatic Tryptophan (W) sit on the same helix as K and interact with the hydrophobic part of cholesterol. The other aromatic Tyrosine (Y) located on another helix contributes binding from other side. In fact, mutations in the CCM also reduced HA's insertion into the cholesterol-enriched nanodomains and retarded HA transport through the Golgi to the cellular plasma membrane (80). For influenza A virus, it might affect HA's lateral distribution in the membrane. Indeed, HA mutants with substitutions of hydrophobic residues, which do not insert into raft domains, were distributed mostly randomly instead of as clusters and exhibited reduced fusion activity. Moreover, less HA was incorporated into the mutant virions (58). The transmembrane region has not only raft association signal, but also apical targeting signal. Nevertheless, they are not completely overlapped since mutations affecting HA's insertion into rafts do not change HA transport to the apical membrane and vice versa (81-83). The cytoplasmic domain contains apical targeting signals as well, since mutations in CT re-directed HA transport to the basolateral membrane in polarized cells (84-86). On the other hand, deletion of CT reduced HA insertion into raft domains and decreased cholesterol incorporation into the mutant virions (86). Furthermore, CT truncation in HA decreased M1 incorporation into DRMs or VLPs and altered the morphology of both virus like particles (VLPs) (78, 86) and influenza A virus (87).

1.6.2 The role of M2 in virus assembly and budding

M2 expressed alone does not insert into raft domains, despite that it contains raft targeting signals (38). However, it is present in the DRMs when co-expressed with HA and/or NA (78). Studies also revealed strong colocalization of M2 with HA in the plasma membrane both in virus infected cells and in cotransfected cells (77, 88). Therefore, M2 might come to the assembly site through an interaction with HA or NA, especially to the edge of the assembly site, since it is predominantly located at the neck of budding virions where it induces negative membrane curvature (89).

The cytoplasmic tail of M2 (Fig. 1.4) contains several features which have effects on virus assembly and budding. The C-terminal domain is important for virus morphology and the production of infectious virus particles. Truncations of the C-terminal region changes the shape of virions from spherical into filamentous and decreases NP protein incorporation into virions (90, 91). Residues 91-94 at the C-terminus contain a LC3 interacting site, which bind to the autophagy protein LC3 and relocalize it to the membrane, thereby preventing the fusion between autophagosomes with lysosomes (20). A M1 binding site (residues 71-73) is located in the middle of the cytoplasmic tail (90, 92). M1, without intrinsic signals for membrane association (93, 94), is recruited to the assembly site through binding to these residues of M2. In the N-terminal domain there are two raft-targeting features: one is a (not

completely) conserved palmitoylated cysteine (C50); the other a cholesterol recognition / interaction amino acid consensus (CRAC) motif (38). It is proposed that the two raft targeting features target M2 to the edge of the viral assembly site, to bind to cholesterol in the raft structure (95). However, deletion of the acylation site, of the CRAC motif and of both raft-targeting features together did not affect virus replication in cell culture (96, 97). On the other hand, a recent NMR structure data revealed that cholesterol binds to the C-terminal part of the transmembrane domain and maintains an orientation parallel to the lipids bilayer, requiring no CARC motif (97).

Both the acylation site and the CRAC motif are located in the amphipathic helix (AH) at the N-terminus of the cytoplasmic tail. The helix has been shown to play a critical role in budding of filamentous virions and efficient membrane scission (89). Full-length M2 protein induced membrane curvature in large unilamellar vesicles (LUVs), whereas no change in the LUV morphology was observed for a M2 mutant, in which the five bulky hydrophobic residues of the AH were changed to alanine. The amphipathic helix alone as well as full-length M2 protein were able to cause vesicle budding into giant unilamellar vesicles (GUVs). In contrast, neither the mutated AH peptide nor the mutant M2 protein showed the ability to induce vesicle release in GUVs. M2 is located at the neck of budding virions and facilitates the membrane scission. However, this process was blocked by mutations in the helix, consequently virus mutants exhibited a so-called “beads on a string” morphology where individual virion fails to be separated from each other and/or from the plasma membrane and as a consequence virus growth was impaired (98, 99). In fact, exchanging any two of the five hydrophobic residues led to defects in virus growth and membrane scission (71). This amphipathic helix senses membrane curvature and preferably binds to highly curved membrane domains comparable to that seen at the center neck of budding virions (100, 101) , which indicates that the helix might facilitate M2 targeting to the virus assembly site. Detailed studies revealed that the peptide forms a helix upon binding to membrane through hydrophobic interaction with lipid tails. It also induces membrane curvature (100), thus M2 might insert into the edge of budding zone like a wedge and cause membrane scission.

1.7 Amphipathic helices as a general feature of proteins that sense or induce membrane curvature

Amphipathic helices (AHs) are characterized by the spatial segregation of hydrophobic and polar residues that form two opposing faces in an α-helix (102, 103). They are a common feature of various cellular proteins involved in membrane deformation. AH is usually oriented parallel to the lipid bilayer, partially penetrating the membrane through its hydrophobic face, which is well suited for membrane deformation and curvature sensing. Their interaction with lipids are mostly reversible and limited to certain cellular membranes in order to support the respective protein to fulfill a specific cellular function.

One type of AH induces membrane curvature by inserting into one leaflet of a bilayer like a wedge. One example is the α0-helix found in the Epsin1 protein, a member of the epsin family which contributes to clathrin-mediated endocytosis (104). One important feature of the epsin family is the conserved N-terminal Epsin N-Terminal Homology (ENTH) domain that contains several amphipathic helices. The ENTH domain binds to the plasma membrane lipid phosphatidylinositol-4,5-bisphosphate (PtdIns(4,5)P2), thus targeting Epsin1 to the areas of endocytosis. The C-terminal region of epsin is essential for recruiting clathrin coat component. The ENTH domain itself and epsin1 protein are capable to induce membrane curvature and tubulation of liposomes. Structure analysis revealed that the residues 3-15 at the N-terminus of ENTH domain form an additional α-helix namely α0 upon binding to PtdIns(4,5)P2 (105). Three charged amino acids of α0 interact with the head group of phosphoinositol, which provides opportunity for it binding to the membrane. Then the folded helix0 inserts into the inner leaflet of plasma membrane resulting in separation of lipid polar heads and therefore membrane deformation (104).

Instead of inducing membrane curvature, another type of AH senses curvature through inserting its bulky hydrophobic amino acids between loosely packed lipid molecules. The most notable example is the ALPS (Amphipathic Lipid Packing Sensor) motif found in ArfGAP1 protein (106), which is involved in disassembly of the COPI coat that surrounds vesicles involved in protein transport from the Golgi apparatus to the endoplasmic reticulum. The ALPS motif preferably binds to highly curved membranes, such as vesicles with small radius rather than to flat membranes (103). ALPS of ArfGAP1 has many uncharged serine and threonine residues in the polar face of its helix, through which it inserts into the external leaflet of lipid bilayers. After binding to the membrane of vesicles, ArfGAP1 promotes GTP hydrolysis in Arf which promotes disassembly of the COPI coat from vesicles, which could then participate in a new round of vesicle formation (102).

Amphipathic helices can also function as cell-penetrating peptides (CPPs), which are applied as a promising approach to deliver membrane impermeable therapeutic agents into cells. CPPs penetrate both leaflets of a membrane and enter the cells either by direct translocation through the plasma membrane or by endocytosis (107). The first CPP was found in Tat protein of HIV-1, which is able to enter the cell and trans-activate viral RNA production (108, 109). Although this first identified CPP is composed of only basic amino acids, further investigation showed that peptides containing both multiple basic amino acids and hydrophobic residues that form an amphipathic helix exhibit higher membrane permeability (110). Amphipathic CPPs cause not only invaginations of GUV membranes in the form of tubules and vesicles and lipid domain separation but also changes in membrane fluidity and cholesterol distribution (111, 112).

2 Objectives of the study

Hemagglutinin and M2 are two integral membrane proteins of influenza A virus, both of which are crucial for virus entry and assembly. The thesis focuses on the two proteins and is divided into two parts.

The first part is about the cholesterol consensus motif (CCM) Y-K-L-W in HA. Our group previously identified a conserved CCM in phylogenetic group 2 HAs and reported that mutations in the CCM retarded intracellular transport of HA and reduced its association with cholesterol-rich nanodomains. In this study I aim to investigate the interaction of cholesterol with the CCM and its effects on virus replication, especially the virus assembly and virus entry mediated by HA. To achieve these, I made single (LA), double (YK2A, LW2A) and quadruple (YKLW4A) mutated HA and used click-labeling with photocholesterol, a cholesterol analogue, to analyze their interaction. I then introduced these mutations into the virus genome and tried to rescue individual mutant viruses. For successfully generated viruses, I analyzed their replication by growth kinetics, viral protein composition, morphology and fusion activity of HA protein with three different methods.

The second part is about the amphipathic helix located in the cytoplasmic tail of M2. Given its importance in induction of membrane curvature and virus budding and given that various amphipathic helices in cellular proteins are also capable to induce membrane deformation, I asked whether other helices could replace M2's helix within the context of a virus infection. To answer this, I either deleted this helix region from M2 or exchanged it with five different helices, two helices (Epsin and ALPS) from cellular proteins, one artificial cell-penetrating peptide (RW16) and two scrambled M2 helices from two different virus strains (sWSN and sUdorn). Replication of recombinant viuses were anaylzed in growth experiments, and virus budding by transmission EM. Furthermore, M2's expression at the cell surface and its incorporation into virions were investigated.

With all these experiments, I hope to provide more detailed information about the role of HA and M2 in virus entry and assembly to better understand the replication of influenza A virus.

3 Materials

3.1 Cells

	Cells	Manufacturer
Eukaryotic	CHO-K1 (Chinese hamster ovary cells)	ATCC CCL-61
	MDCK II (Madin-Darby canine kidney cells)	ATCC CCL-34
	HEK-293T (human embryonic kidney-293T cells)	ATCC CRL-1573
	Chicken erythrocytes (25%)	Merk
	Human erythrocytes	DRK-Blutspendedienst Nord-Ost
	Embryonated chicken eggs	VALO BioMedia
Prokaryotic	*Escherichia coli* DH5α	Life technologies
	Stellar Competent cells	Takara Bio, Japan

3.2 Antibodies

	Name	Manufacturer
Primary antibody	Rabbit anti-HA2 antiserum	Gift from Dr. Klenk
	Mouse anti-β-catenin antibody	Sigma-Aldrich
	Mice anti-M2 antibody (14C2)	Santa Cruz
	Goat anti-M1 antibody	Abcam
Secondary antibody	Anti-Rabbit IgG, HRP	Sigma-Aldrich
	Anti-mice IgG, HRP	Sigma-Aldrich
	Anti-goat IgG, HRP	Sigma-Aldrich
	Anti-rabbit Alexa Fluor 568	ThermoFisher
	Anti-mouse Alexa Fluor 488	ThermoFisher

3.3 Reagents

Name	Manufacturer
Phusion polymerase	ThermoFisher
XhoI restriction endonuclease	NEB
BglII restriction endonuclease	NEB
T4 ligase	NEB
DMEM (Dulbecco’s Modified Eagle Medium)	PAN Biotech
Opti-MEM	Gibco
MEM (Minimal Essential Medium), 2X	Biozym
FCS (fetal calf serum)	Perbio, Bonn
35% Bovine serum albumin (BSA)	Sigma-Aldrich

Trypsin (TPCK treated)	Sigma-Aldrich
Penicillin/Streptomycin (10,000 U/mL)	PAN Biotech
PBS w and w/o calcium/magnesium	PAN Biotech
EDTA-Trypsin	PAN Biotech
Dimethyl sulfoxide (DMSO)	AppliChem
TurboFect transfection reagent	ThermoFisher
Lipofectamine 3000 Reagent	ThermoFisher
cOmplete™, EDTA-free Protease Inhibitor Cocktail	Roche
Avicel	FMC BioPolymer
Crystal Violet	CarlRoth
DEAE-Dextran	Sigma-Aldrich
Octadecylrhodamine B chloride (R18)	ThermoFisher
Calcein-AM	ThermoFisher
Laurdan	ThermoFisher
Pico-azido picolyl sulfo cy3	Jena Bioscience
Protein-G-Sepharose	GE Healthcare
Cholesterol powder	Sigma-Aldrich
Photocholesterol	Gift
Methyl-β-cyclodextrin (MβCD)	Sigma-Aldrich
Chloroform	Sigma-Aldrich
Methanol	Fluka
D(+)-Sucrose	CarlRoth
30 % acrylamide and bisacrylamide stock solution (37.5:1)	CarlRoth

3.4 Prepared Solutions

Purpose	Name	Composition
	PBS	0.8% (w/v) NaCl, 0.02% (w/v) KCl, 0.02% (w/v) KH2PO4, 0.135% (w/v), Na2HPO4·2H2O
	PBST	PBS with 0.1% Tween-20
Click labeling with photocholesterol	IP buffer	500 mM Tris-HCl, 20 mM EDTA, 30 mM sodium pyrophosphate decahydrate, 10 mM sodium fluoride, 1 mM sodium orthovanadate, 2 mM benzamidine, 1 mM PMSF, 1 mM NEM and 1X protease inhibitor cocktail
Click labeling with photocholesterol	Lysis buffer	1% NP40 in IP buffer
Regular cell lysis	Lysis buffer	1% Triton in ddH_2O
Cell fixation	Fixation solution	4% formaldehyde in PBS
	1X TNE buffer	10 mM Tris, 100 mM NaCl und 1 mM EDTA, pH 7.4
Hemolysis assay	Citric acid buffer	20 mM citric acid, 150 mM NaCl

Ghost preparation	Hypotonic buffer	4.7 mM Na2HPO4, 1.1 mM NaH2PO4, 1 mM EDTA, pH7.4
Fluorescence dequenching assay	Fusion buffer	150 mM NaCl, 10 mM Na-acetate x 3 H2O, pH 7.4
Coomassie staining	Coomassie solution	45% (v/v) ethanol, 10% (v/v) acetic acid, 0.25% (w/v) Coomassie Brilliant Blue G-250
SDS-Gel	Stacking-gel solution	5% (w/v) acrylamide/bisacrylamide, 0.1% SDS, 125 mM Tris·HCl (pH 6.8), 0.075% (w/v) APS, 0.15% (v/v) TEMED
SDS-Gel	Seperating-gel solution	12% (w/v) acrylamide/bisacrylamide stock solution, 0.1% (w/v) SDS, 375 mM Tris·HCl (pH 8.8), 0.05% (w/v) APS, 0.1% (v/v) TEMED
SDS-PAGE	1X non-reducing loading buffer	62.5 mM Tris·HCl, 2% (w/v) SDS, 10% (v/v) glycerin, 0.01% (w/v) bromophenol blue, pH 6.8
SDS-PAGE	1X reducing loading buffer	1X non-reducing buffer + 5% (v/v) β-Mercaptoethanol
Western blot	Blocking buffer	5% skimmed-milk powder in PBST
Immunofluorescence	Blocking buffer	3% BSA in PBS
Virus infection	Infection medium	DMEM, 0.1% FBS, penicillin/streptomycin (100 units/mL), 0.2% BSA and 1 µg/ml TPCK-Trypsin
Cell culture	Growth medium	DMEM, 10% (v/v) FCS, penicillin/streptomycin (100 units/mL)
Plaque assay	Overlay medium	1XMEM, 0.6% avicel, 0.2% BSA, 0.1% FBS, penicillin/streptomycin, 2 µg/ml TPCK-Trypsin, 0.5% DEAE-Dextran, 5% NaHCO3

3.5 Kits

Name	Manufacturer
In-Fusion® HD Cloning Kit	Takara Bio, Japan
Invisorb Fragment Cleanup Kit	Stratec Biomedical AG
Invisorb Spin Plasmid Mini Two	Stratec Biomedical AG
PureYield™ Plasmid Maxiprep System	Promega GmbH
RTP® DNA/RNA Virus Mini Kit	Stratec Biomedical AG
QIAGEN® OneStep RT-PCR Kit	QIAGEN
SensiFAST™ Probe Lo-ROX One-Step Kit	Bioline
Amplex™ Red Cholesterol Assay Kit	Thermo Fisher
Roti-Quant universal kit	Carl Roth
CuAAC Biomolecule Reaction Buffer Kit (THPTA based)	Jena Bioscience
Pierce™ ECL Plus Western Blotting Substrate	Thermo Fisher

3.6 Primers

Purpose	Name	sequence
CCM mutants for reverse genetics and RT-PCR	HA (pHH, Fo)	TGAAAATGGTTGGGAAGGTCTGG
	HA (pHH, Re)	CGCATGTTTCCGTTCTTCACAC
	pHH (Fo)	GAACGGAAACATGCGGTGCAC
	pHH (Re)	TCCCAACCATTTTCAATAAACCCTG
CCM mutants for expression	HA (pCA, XhoI, Fo,)	CCGCTCGAGATGAACACTCAAATCCTGG
	HA (pCA, BglII, Re)	GAAGATCTTTATATACAAATAGTGCACCGC
HA(FPV) sequencing	HA(H7, Fo)	ATGAACACTCAAATCCTGG
M2 RT-PCR and sequencing (WSN)	M2 (pHW, Fo)	GAACGGAGATCCAAATAACATG
	M2 (pHW, Re)	GCTCTATGTTGACAAAATGACC
RT-qPCR (M, WSN)	M (Fo)	AGATGAGYCTTCTAACCGAGGTCG
	M (Re)	TGCAAANACATCYTCAAGTCTCTG
	M-probe	TCAGGCCCCCTCAAAGCCGA
RT-qPCR (NA, WSN)	NA (Fo)	TGGGTCAATCTGTATGGTAGTC
	NA(Re)	GCTGCCTTGGTTGCATATT
	NA-Probe	TGGATTAGCCATTCAATTCAAACCGGA

3.7 Plasmids

Purpose	Name
Reverse genetics (FPV*)	PB1, PB2, PA, HA, NP, NA, M, NS-pHH21 Exp-PB1, Exp-PB2, Exp-PA, Exp-NP-pcDNA LA, YK2A, LW2A, YKLW4A-pHH21
Reverse genetics (WSN)	PB1, PB2, PA, HA, NP, NA, M, NS-pHW2000 ALPS, Epsin, RW16, sUdorn, sWSN-pHW2000
Expression	LA, YK2A, LW2A, YKLW4A, HA-pCAGGS

3.8 Sequences of amphipathic helices

Name	Sequence
AH-M2	RLFFKCIYRRFKYGLKRG
sUdorn	RLFKYGCFRYFIKRGKLR
sUdorn	RFFKLGYLEFKIFRGCRH
ALPS	RLFFLNSAMSSLYSGWSSFTTGASKFAS
Epsin	RLFSSLRRQMKNIVHN
RW16	RLFRRWRRWWRRWWRRWRR

3.9 Equipments

Device	Manufacturer
Thermo cycler	Eppendorf
Cell culture consumes (plates, flasks, pipettes)	Sarstedt
24 mm Transwell with 0.4 µm pore polyester membrane insert	Costar
Heracell 240i CO2 incubator	Heraeus
Gradient master 108	Biocomp
Tabletop centrifuge 5417R, 5804R	Eppendorf
Potima XPN-80 Ultracentrifuge	Beckman Coulter
Blacklight Blue (UV) Lamp	Sankyo Denki
Power pack p25	Biometra
Semidry membrane blotting machine	Peqlab
Chemiluminescence Imaging - Fusion SL	PeqLab
Typhoon FLA 9500 scanner	GE Healthecare
CytoFlex S BA31094	Beckman Coulter
AE30 Inverted microscope	Motic
Axio Vert.A1 fluorescence microscope	Zeiss
Live cell imaging with VisiScope confocal FRAP System	VisiScope system
FEI Tecnai F20 electronic microscope	FELMI-ZFE
Spectrometer “NanoDrop”	PeqLab
Cary Eclipse Fluorescence Spectrophotometer	Varian
Synergy H1 Hybrid Multi-Mode Reader	BioTek

3.10 Computer applications

Purpose	Software or website
Graphs, plots	Microsoft Excel 2010, GraphPad Prism 5.01
Image processing and Intensity quantification	Image J (Fiji)
Figures	Pymol, Microsoft Powerpoint, Adobe illustrator
Nucleotide sequence analysis	Lasergene
Helical wheel plot	http://heliquest.ipmc.cnrs.fr/
Flow cytometry	CytExpert
RT-qPCR	StepOne software v2.3

4 Methods

4.1 Molecular cloning

4.1.1 Construction of HA mutants for reverse genetics

To rescue FPV* mutant viruses LA, YKL2A, LW2A and YKLW4A, the sequences of HA mutants were inserted into the plasmids pHH21 for reverse genetics. The HA mutants in the plasmid pECerulean were used as template. Individual sequence containing the specific mutations was cloned by PCR and inserted into plasmid pHH21 with In-Fusion® HD Cloning Kit. This kit contains the Clontech's proprietary In-Fusion Enzyme, which fuses DNA fragments e.g. PCR-generated sequences and linearized vectors efficiently and precisely by recognizing a 15 base pair overlap at their ends, thus no additional restriction site would be introduced into the target sequence. Experiments was done according the provided instruction.

Step 1: PCR

To get desired HA DNA fragments and linearized vector, two pairs of primers have been synthesized. HA (pHH21, Fo) and HA (pHH21, Re) are for HA fragments, pHH (Fo) and pHH (Re) are for vector (sequences of primers are in 3.6). The DNA fragments of HA mutants and vector were amplified by PCR. The mixture of PCR reaction and the cycling conditions are listed below.

Component	Amount
Buffer (5X)	10μL
Template	0.5μL
Primer (Fo, 20μM)	1.25μL
Primer (Re, 20μM)	1.25μL
dNTPs (10 mM)	1μL
Phusion(polymerase)	0.5μL
ddH_2O	to 50μL

Cycle step	Tm	Time	Cycles
Initial Denaturation	98°C	30s	1
Denaturation	98°C	30s	30
Annealing	55°C	30s	
Extension	72°C	30s/kb	
Final extension	72°C	10min	1
cooling	16°C	hold	

Step 2: In-fusion

The DNA fragments were verified by DNA electrophoresis in an 1% agarose gel and extracted from the gel using Invisorb Fragment Cleanup Kit according to the manufacturer's instruction. The purified HA fragments and vector fragments were fused together at the presence of In-Fusion HD Enzyme at 50°C for 15min. The mixture of the reaction are listed below.

Component	Amount
5X In-Fusion HD Enzyme Premix	2μL
HA mutant fragment	50ng
Linearized pECerulean	100ng
ddH_2O	to 10μL

Step 3: Transformation

After cooling on ice, the In-Fusion products were transformed into Stellar Competent cells (provided in the In-Fusion® HD Cloning Kit). The transformation procedure was done

according to the manufacturer's instruction. Briefly, 5µL of the reaction was added to 50µL of competent cells together with 50µL SOC medium (provided in the kit too) to bring the volume to 100µL. 50µL of the mixture was then plated on a LB plate containing 100 µg/ml of ampicillin and the plates were incubated overnight at 37°C.

Step 4: Plasmid isolation

After overnight culturing competent cells grew as individual colonies on the plate. Several colonies were picked up from the plate and further cultured in 5ml fresh liquid LB medium containing 100 µg/ml of ampicillin and grown at 37°C for 8-16h, so that there would be enough cells for plasmid isolation. The Invisorb Spin Plasmid Mini Two Kit was used to isolate plasmids and all the procedures were done according to the manufacturer's instruction. In principle, the bacteria were pelleted by low speed centrifugation and resuspended in alkaline lysis solution in the presence of RNase to digest RNA. The mixture was then neutralized and adjusted to the binding conditions so that plasmid DNA binds to the membrane of the spin filter while chromosomal DNA, denatured proteins and cellular debris were clarified. Other contaminations were further removed after washing and ultra pure plasmid DNA was eluted in ddH_2O. The concentration of the plasmids was measured by analyzing the absorbance at 260nm with a NanoDrop spectrometer, which were then sent for sequencing to confirm successful insertion.

4.1.2 Construction of HA mutants for expression

To get high expression of HA protein in transfected cells, the full sequences of HA WT and CCM mutants were individually inserted into the vector pCAGGS through introducing the restriction site XhoI and XbaI to the upper and down stream of the sequence respectively. The plasmid construction was done through regular molecular cloning with PCR, restriction digest, ligation, transformation and plasmid purification. Each step will be described as following.

Step 1: PCR

The primer pair HA (pCA, XhoI, Fo,) and HA (pCA, BglII, Re) (sequences of primers are in 3.6) were used to amplify HA fragment. The reaction mixture and cycling conditions are the same as described in 1.4.1.

Step 2: Digestion with restriction enzymes

After gel extraction both the purified HA fragments and the vector were digested by the restriction enzyme XhoI and BglII for 1h at 37°C. The reaction mixture is listed below.

Component	Amount
DNA (HA fragment / pCAGGS)	30µL / 1µg
XhoI	1µL
BglII	1µL
10X Buffer	5µL
ddH_2O	to 50µL

The reaction mixtures were then loaded into an 1% agarose gel for the identification of DNA fragments by DNA electrophoresis, which were then extracted and purified using Invisorb Fragment Cleanup Kit.

Step 3: Ligation

Each digested HA fragment will have complementary sticky ends with digested vector. They were then mixed together with T4 ligase and incubated at 8°C overnight to allow successful ligation of HA fragment and linearized vector. The reaction mixture are listed below.

Component	Amount
HA fragment	50ng
pCAGGS	100ng
T4 ligase	1µL
10X Buffer	2µL
ddH_2O	to 20µL

Step 4: Transformation

5µL of the ligation product was added to 50µL competent cells DH5α and incubated on ice for 30min. They were then treated with a "heat shock" at 42°C for 45s to allow the competent cells to take up ligation product. After cooling on ice for 5min, 950µL fresh LB medium was added and incubated at 37°C for 1h. 100µL of the culture cells was then spread on a LB plate containing 100 µg/ml of ampicillin and incubated overnight at 37°C.

The following steps are the same as described in 1.4.1.

4.1.3 Construction of M2 mutants for reverse genetics

The replacement of amphipathic helix region in M2 by other peptide sequences in the plasmid pHW2000 which expresses the segment 7 of WSN strain was done by a former colleague Stefanie Siche. Details have been described in her dissertation.

4.2 Cell culture

4.2.1 Cell culture

Madin-Darby canine kidney (MDCK II), Chinese hamster ovary (CHO) and human embryonic kidney 293T cells were grown in DMEM (Dulbecco's modification of Eagle's medium, PAN, Aidenbach, Germany) supplemented with 10% FCS (fetal calf serum, Perbio, Bonn, Germany) and penicillin/streptomycin (100 units/ml and 100 µg/ml, respectively) at 37 °C and 5% CO_2. Cells were passaged every 2-3 days when they reached nearly 100% confluence in tissue culture flask. To passage cells, trypsin/EDTA were added to detach after washing once with PBS. The reaction was stopped by adding fresh growth medium and cells were passaged at a ratio of 1:5-1:10.

4.2.2 Cell thawing and freezing

To thaw cells, an aliquot of cell stock stored in liquid nitrogen tank was thawed in 37 °C water bath for no more than 2 min. Cell were then transferred to the 15ml Falcon tube filled with 10 ml fresh growth medium and centrifuged at 1200g for 5min to pellet cells, which were then resuspended in fresh growth medium and transferred to the T25 or T75 culture flask.
To freeze cells, cells grown to nearly 100% confluence were trypsinized, resuspended in growth medium, centrifuged at 1200g for 5min and resuspended in 8 ml growth medium. The suspension was then added with 1ml FCS (final concentration 20%) and 1ml DMSO (final concentration 10%). After thoroughly mixing, the cell mixture was aliquoted to cryo tubes for storage in liquid nitrogen.

4.2.3 MDCK polarized cell culture

6.5mm membrane filter (24-well plate) having pores with a diameter of 0.4µm was used to grow polarized MDCK II cells. The membrane filter was firstly pre-incubated with growth medium (1.5 ml growth medium in the upper and 2.6 ml in the lower chamber) for more than 30min. Then the medium was removed, 2.6ml fresh growth medium was added to the lower chamber and $5X10^5$ cells in 1.5ml fresh growth medium were seed onto the membrane filter in the upper chamber. The medium in both chamber were changed daily and 4 days later cells were polarized and thus ready to be used.

4.3 Virology methods

4.3.1 Reverse genetics

293T cells were seeded into 60mm culture dishes one day before so that they reached 80% confluence for transfection the next day. Cells were washed once with DMEM and changed to 4ml Opti-MEM. The tranfection mixture was prepared by adding 6µg DNA, either 12 plasmids (0.5µg each, FPV/H7N1) or 8 plasmids (0.75µg each, WSN/H1N1), together with 12µl TurboFect transfection reagent into 600µl Opti-MEM. After incubating for 15-20min at room temperature, the mixture was added drop-wise to the cells, which was then incubated in the 37°C incubator. 4-6h later, the cells were washed once with fresh DMEM and added with 4ml infection medium. 48h post transfection, some cells died due to virus production and the culture supernatant could be harvested and centrifuged at 4000g for 5min to remove cell debris. They were divided into small aliquots, some stored at -80°C, whereas the other directly passaged onto MDCK II cells for further amplification. When 50-80% of the MDCK II cells died from infection, the viruses in the culture supernatant were harvested, purified, separated into small aliquots and stored at -80°C as virus stocks.

4.3.2 Virus propagation in embryonated chicken eggs

When the embryonated chicken eggs grew to 9 to 11 days old, they were inoculated with FPV* WT and CCM mutants from the allantoic cavity. The air sac was marked by drawing a pencil line and the inoculation site should be 0.5mm above this line. A hole was made at the marked inoculation site and also the top of the air sac. An 1.0 mL syringe fitted with a 22.5 gauge needle was used to suck virus solution (10000 pfu in PBS), which was injected through the inoculation hole into the allantoic cavity without sticking the embryo. PBS without virus was used as negative control. The holes were then sealed with wax and the eggs were incubated in the incubator. 2-4 days post inoculation, the embryo was no longer viable due to infection, so they were put into -80°C for 20min. The egg shell above the air sac was removed carefully so the allantoic fluid could be observed clearly, which was then harvested with a pipette and stored at -80°C for further analysis.

4.3.3 TCID50 tests

MDCK II cells were seeded into one 96-well plate A one day before so that they were nearly 100% confluence the next morning. The cells in each well were washed once with DMEM and changed to 100µl fresh infection medium. Viruses were three-fold serially diluted in infection medium in another 96-well plate B. Briefly 120µl infection medium was added to each well of 96-well plates and the first row were added with another 60µl virus (8 replicates per virus). After mixing by pipetting, 60µl mixture was then transferred to the next row. This dilution was repeated until row 11 since the last row should be used as negative control. 100µl diluted virus (or medium) was then transferred from plate B onto the MDCKII cells in the plate A, which was then incubated in 37°C incubator. 3 days post infection, the plate A were washed once with PBS to remove dead cells, while the living cells were fixed with 4% formaldehyde in PBS for 5 min and stained with 0.1% crystal violet. The number of positive wells and negative wells were counted and the TCID50 titer was calculated by Reed & Muench Method.

4.3.4 HA test

Chicken erythrocytes were washed with PBS for several times until no redness was seen in the supernatant after centrifugation at 1000g for 5min. The erythrocytes were then resuspended in PBS to make a 10% solution as a stock, which was further diluted to 1% for HA test. Viruses were two-fold serially diluted in PBS in U-bottom 96-well plates, each well containing 50µl virus solution. Another 50µl 1% chicken erythrocytes was then added to the virus and incubated for 30 minutes at room temperature. 50µl PBS was used as negative control. Positive wells show a uniform reddish color across the well, whereas negative results appear as dots in the center of the well.

4.3.5 Plaque assay

MDCK II cells were seeded into 6-well plates one day earlier and they were nearly 100% confluence the next day. Virus samples were 10-fold serially diluted in infection medium in 1.5ml Eppi tubes. 500µl diluted virus were added to the MDCK II cells after washing once with DMEM. After binding for 1h with occasionally shaking, cells were washed once with DMEM to remove unbound viruses. Then cells were added with 2 ml overlay medium and left in 37°C incubator for 2 days. The overlay medium was fluidly so it could be removed by sucking with pipet. After washing once with PBS, cells were then stained with 0.1% crystal violet for 10min so that plaques could be seen and counted.

4.3.6 Growth curve

MDCK II cells were seeded into 6-well or 24-well plates one day before infection so they could be nearly 100% confluent the next day. Cells were washed once with DMEM and then infected with virus at an moi of 0.001 (for multiple replication cycle) or 1 (for single replication cycle). After binding for 1h, cells were washed once with DMEM to remove unbound viruses and changed to fresh infection medium. For multiple replication cycle, culture supernatant was harvested at 9h, 23h, 34h and 47h post infection. For single replication cycle, supernatant was harvested at 6h and 9h post infection. Cell debris in the culture supernatant was cleared by centrifugation at 4000g for 5min. Virus titers were measured by HA assay, plaque assay or TCID 50 assay.
For virus growth in polarized MDCK II cells, viruses were added to the upper chamber at an moi of 0.001. After binding for 1 h, the culture medium in both the upper and lower chamber were changed to fresh infection medium. The culture medium from both chambers were harvested at 8 h, 24 h, 34 h and 48 h post infection and virus titers were determined by HA assay

4.3.7 Competitive growth

MDCKII cells were seed into 6-well plates and they were nearly 100% confluent the next day. Virus mutant YK2A or LW2A was mixed with virus WT at a ratio of 5 to 1 and MDCK II cells in 6-well plates were then infected with the virus mixture with a total moi of 0.0005 (based on TCID50 titer). Culture supernatant was harvested at 24h and 48h post infection. Viral RNA of these virus samples and virus mixture at the starting point were extracted using the RTP® DNA/RNA Virus Mini Kit according to the manufacturer's instruction. The vRNA concentration was determined by NanoDrop spectrometer. Reverse transcription of HA fragment was done with the specific primers HA (pHH, Fo) and HA (pHH, Re) (see 3.6) using QIAGEN® OneStep RT-PCR Kit. The products were separated in and extracted from 1% agarose gel and sent for sequencing.

4.3.8 RT-qPCR

The copy number of vRNA segment M and NA of the virus WSN WT and M2 mutants at 34h of growth curve analysis was determined by one-step RT-qPCR using SensiFAST™ Probe Lo-ROX One-Step Kit (Bioline) according to the manufacturer's instruction. Viral RNA was extracted as described before and 5µl of vRNA was used for analysis. The probes and primers used for RT-qPCR are listed in section 3.6. The plasmids for reverse genetics were used as standard for calculating the copy number.

4.3.9 Virus stability assay

WSN WT and M2 mutant viruses were diluted to a concentration of 200 000 pfu/ml in infection medium. 500µl diluted viruses were added into each well of 24-well plates, which was then incubated in 37°C incubator. One aliquot was taken out per day and the virus titer was measured again by plaque assay.

4.3.10 Sucrose gradient purification

Viruses harvested from infection in MDCKII cells or embryonated chicken eggs were used for purification. After clearing cell debris or big clucks by low speed centrifugation (4000g, 5min),

viruses were pelleted by ultracentrifugation at 100000 g for 2h and resuspended in 1X TNE buffer. A continuous 20-60% sucrose gradient was made by Gradient Master. The virus suspension was loaded gently on top of the gradient and then centrifuged for 4h at 100000g 4°C. The viral band at density of 35-50% of the gradient was collected, mixed with PBS, subjected to ultracentrifugation again and resuspended in 1X TNE buffer. The purified virus was subjected to SDS-PAGE or negative staining electronic microscopy.

4.3.11 Cholesterol supplement to virus

To add exogenous cholesterol to the viral membrane of FPV* WT and CCM mutants, cholesterol was dissolved in chloroform: methanol (1:1; v:v) to make a 10mM stock solution and methyl-β-cyclodextrin (MβCD) was dissolved in distilled water to a concentration of 2mM. 6µl cholesterol stock was dried under a nitrogen stream and re-dissolved in 150µl MβCD solution, which was incubated overnight at 37°C with shaken to load MβCD with cholesterol. Viruses purified through a 20% sucrose cushion were resuspended in 1X TNE buffer and adjusted an HA titer of 2^8. 100µl virus was then incubated with 100µl cholesterol-MβCD complex for 30min at room temperature. After centrifugation at 100000g for 20 min to remove extra cholesterol, the virus was pelleted and resuspended in 1xTNE buffer. 10µl virus with an HA titer of 2^8 loaded or not loaded with exogenous cholesterol was analyzed again with hemolysis assay.

4.4 Biochemistry and molecular biology

4.4.1 SDS-PAGE (sodium dodecyl sulfate–polyacrylamide gel electrophoresis)

SDS-PAGE is a method to separate proteins based on their molecular weight. SDS is a detergent, having a strong protein-denaturing ability and binding to protein backbone with negative charge, which gives proteins similar charge-to-mass ratios. Under reducing condition, Dithiothreitol (DTT) is added to the loading buffer to cleave the disulfide bond. The polyacrylamide gel is formed by adding the radical initiator ammonium persulfate (APS) and the catalyst TEMED to allow the polymerization of acrylamide so that two acrylamide molecules are cross-linked with each other. The concentration of acrylamide in the stacking gel is 4% while that in the separation gel 12% or 15% depending on the mass of targeted proteins.
Samples of purified viruses or cell lysate were mixed with loading buffer (with or without DTT), incubated at 95°C for 5min, cooled down and loaded onto SDS-Gel.
To analyze the protein composition of purified viruses, the gel was washed twice with distilled water after electrophoresis, stained with coomassie brilliant blue for 1h or overnight, washed with distilled water until a weak background signal and captured by camera.
To analyze a specific protein, the gel was subjected to western blot.

4.4.2 Western blot

After SDS-PAGE, the proteins in gels were blotted onto polyvinylidene difluoride (PVDF) membrane at 200- 220mA for 1h using a semi-dry transfer system. The membrane was firstly incubated with blocking solution [5% skim milk powder in PBS with 0.1% Tween-20 (PBST)] for 30min to block non-specific binding and then with primary antibody for 2h at room temperature or overnight at 4°C. The primary antibody was diluted in blocking solution. The dilution of rabbit-derived antisera against the HA2 subunit of FPV is 1:2000; that of mice-derived anti-M2 monoclonal antibody is 1:1000; that of goat-derived anti-M1 mAb is 1:1000. After washing (4x5 min with PBST), the membrane was incubated with secondary antibody coupled with horseradish peroxidase (diluted 1:5000 in blocking solution) for 1h at room temperature. After washing, the ECLplus reagent was applied to the membrane so that proteins are able to give chemiluminescence signals which was then detected by a Fusion SL camera system. The density of bands was measured by Image J (113).

4.4.3 Immunoprecipitation

HA WT or CCM mutants-expressed CHO cells were lysed in 500µl lysis buffer (1% NP40 in IP buffer) for 1h on ice. After centrifugation at 4°C 15min with 20000g, the supernatant was transferred to a new 1.5ml Eppi tube and incubated with 0.5µl anti-HA2 antisera (1:1000) at 4°C overnight with agitation. 50µl of protein-A-sepharose (1:1 diluted in PBS) was added to the mixture and incubated at 4°C for another 4h, which was pelleted down by short centrifugation (20s 12000g). After washing twice with IP buffer and once with PBS, the protein was resuspended in PBS for downstream experiments.

4.4.4 Determination of protein concentration

The protein concentration in purified viruses was measured using Roti-Quant universal kit according to manufacturer's instruction. Briefly, 10µl purified virus added with 40µl PBS was incubated with 100µl reaction mixture at 37°C for 30min. The Cu2+ ions in the reaction mixture were reduced to Cu+ ions by peptide bonds in protein. The latter binds to the PCA forming a complex exhibiting a strong light absorption with a maximum of 503 nm, which is directly proportional to the concentration of the protein present. BSA was used as standard and diluted in PBS. The light absorbance at the wavelength of 503nm was measured with a micro-plate spectrometer.

4.4.5 Determination of cholesterol concentration

The cholesterol concentration in purified viruses was measured using Amplex™ Red Cholesterol Assay Kit according to manufacturer's instruction. Briefly, 5µl of purified virus was lysed in 45µl 1X reaction buffer (0.1 M potassium phosphate, pH 7.4, 50 mM NaCl, 5 mM cholic acid, 0.1% Triton X-100) and then incubated with 50µl working solution (300 µM Amplex Red reagent, 2 U/mL Horseradish peroxidase (HRP), 2 U/ml cholesterol oxidase in 1X reaction buffer) for 30 min at 37°C in the dark. In this mixture, cholesterol was oxidaized by cholesterol oxidase to produce H_2O_2 that, in the presence of horseradish peroxidase (HRP), reacts with the Amplex Red reagent in a 1:1 stoichiometry to produce highly fluorescent resorufin. The fluorescence was measured by a fluorescence microplate reader with excitation at 555 nm and emission at 590nm. Only cholesterol not cholesterol esters was analyzed since viruses were not treated with cholesterol esterase.

4.4.6 Photocholesterol crosslinking of HA

The click-photocholesterol (6,6'-Azi-25-ethinyl -27-norcholestan-3β-ol) was used here to investigate whether HA-WT and HA with mutations in the CCM interact with cholesterol by click-labeling.
To label HA-expressing cells with photocholesterol, CHO cells in 6-well plates were transfected with 3µg plasmid with 6µl TurboFect transfection reagent. 4-6 h after transfection, cells were washed once with DPBS+ and changed to 1ml DMEM without serum. 5µl photocholesterol (from an 5 mg/ml stock in ethanol, final concentration is 50 µM) was added to the cells and incubated overnight in 37°C incubator. 24h post transfection, cells were chilled on ice, exposed to UV light (wavelength 320–365 nm, power 8W, 60V, 3.5 A) for 10 minutes to activate the diazirine group and then lysed in 500µl 1% NP40 in IP buffer. 50µl (= 10%) of the cell lysate was subjected to western blot for comparing the total expression of HA. The left 450µl (= 90%) of the cell lysate was subjected to immunoprecipitation with anti-HA2 antiserum to pull down HA protein.
To directly label HA protein with photocholesterol, HA was first immunoprecipitated from 450µl cell lysate of transfected CHO cells, resuspended in 100µl PBS, mixed with 0.5µl photocholesterol and then illuminated with UV light for 10 minutes at 4°C. The other 50µl cell lysate was also analyzed by western blot.
HA-photocholesterol complexes were then clicked to Pico-azido picolyl sulfo cy3 using the CuAAC Biomolecule Reaction Buffer Kit according to the manufacturer's instruction. Samples were subjected to SDS-PAGE and HA-photocholesterol in the native (unfixed) gel was visualized using the Typhoon FLA 9500 scanner (Excitation =555 nm; Emission =565 nm). The density of HA bands of the photo-crosslinking (fluorogram) and the western-blot

were measured with Image J software. The ratio of photo-crosslinking (fluorogram) to total protein expression (western blot) were calculated. The results of HA WT in each experiment were set as 100%.

4.4.7 Membrane fusion assays

4.4.7.1 Hemolysis assay with virus particles

To investigate the hemolysis activity of FPV* WT and CCM mutants, virus stocks stored at -80°C were adjusted to an HA titer of 2^6 with infection medium. 100µl virus in U-bottom 96-well plates were incubated with 100µl 2% chicken erythrocytes in PBS for 30 min on ice in order to allow viruses to bind to red blood cells (RBCs). The plates were centrifuged at 250g for 1min to remove unbound viruses. The cell pellets were resuspended in 100µl citric acid buffer adjusted to the desired pH and incubated at 37°C for a desired time length to allow fusion between virus and RBCs. For analysis of pH dependence, citric acid buffer with pH from 5 to 7.5 were used and time length of incubation was 1h. For analysis of hemolysis kinetics, the fusion happened at pH5 with incubation for 0.5 to 4 hours. After another centrifugation at 250g for 1min, 50µl of the supernatant was transferred to a new flat-bottom 96-well plate and mixed with 50µl PBS. The hemoglobin released from RBCs due to fusion was determined using a micro-plate spectrometer to measure its light absorbance at the wavelength of 405nm.

4.4.7.2 R18 fluorescence dequenching assay with virus particles

To analyze the hemifusion activity of FPV* WT and CCM mutants, MDCK II cells grown in T175 flasks were infected with viruses. Culture supernatants were harvested, cleared from cell debris by low-speed centrifugation (2000g, 5 min), pelleted (100000x g, 2h, 4°C) through a 20% sucrose cushion, resuspended in 1X TNE buffer and adjusted to an HA titer of 2^10. To label the viral membrane with octadecyl rhodamine B chloride (R18), 50µl virus was incubated with 0.5µl R18 (2mM stock dissolved in ethanol, the final concentration is 20µM) for 30min on ice protected from light. After centrifugation at 100000g for 15 min at 4°C, the unincorporated R18 was removed and labeled viruses were resuspended in 50µl PBS.
To prepare erythrocyte membrane ghosts, human RBCs were washed three times with PBS. After centrifugation at 2000g for 10min, the RBCs were lysed in ice-cold hypotonic buffer for 30min with occasional agitation. The lysate was then washed again with cold PBS for 5-8 times until no redness in the membrane ghosts. The protein concentration in the ghosts was determined using Roti-Quant universal kit as described before. Freshly prepared erythrocyte ghosts can be used as long as 6 month when stored at 4°C.
For the fusion assay, 10µl R18-labeled virus was mixed with 40µl 1 mg/ml erythrocyte ghosts for 20 min on ice. 1.96 ml fusion buffer was added into a cuvette with a magnetic stir bar and warmed up to 37°C. The cuvette was put into the chamber of a temperature-adjustable fluorescence spectrophotometer. After adding the virus-ghost mixture to the cuvette, the spectrophotometer started to record the fluorescence intensity. When the fluorescence intensity was steady, 7µl citric acid (250 mM) was added to the solution to lower its pH to 5. 10min after lowing the pH, 50µl 1% Triton X-100 was added to the cuvette to achieve the maximal dequenching.
In order to analyze the fusion activity, the percentage of fluorescence dequenching (FDQ) was calculated by the formula FDQ=100×(F(t)-F(0))/(F(max)-F(0)), in which F(0) stands for the fluorescence intensity before adding citric acid, F(max) the maximal dequenching fluorescence intensity after adding Triton X-100 and F(t) the fluorescence intensity at each time point. The equation used for curve fitting is f(x) = a*[1-e^(-kx)].

4.4.7.3 Double-labelled erythrocyte fusion assay with expressed HA

To label erythrocytes with the lipidic dye R18 and the content marker calcein-AM, human erythrocytes were washed and resuspended in PBS to a concentration of 1%. 15ml 1% erythrocytes suspension was added with 20µl of R18 (1 mg/ml in ethanol) and incubated with gentle stirring for 30min at room temperature (RT) in the dark. 25 ml growth medium was added and incubated for 20min at RT in the dark to absorb unbound R18. The erythrocytes

was then washed twice with PBS and resuspended in 2ml PBS. Freshly prepared Calcein-AM (50µg dissolved in 10µl DMSO + 40µl PBS, freshly prepared every time) was added to the suspension and incubated for 45 min at 37°C protected from light. The labelled erythrocytes were washed five times with PBS and resuspended in 5 ml DPBS+ (DPBS with Ca^{2+} and Mg^{2+}).
For the fusion assay, CHO cells grown in 6-well plates were transfected with HA WT or HA YKLW4A cloned into the pCAGGS vector. 24h after transfection, cells were washed twice with DPBS+ and treated with 500µl Trypsin/Neuraminidase solution (Trypsin 5ug/ml, Neuraminidase 0.22mg/ml in DPBS+) for 5min. 2ml growth medium was added to the cells to stop the reaction followed by washing twice with DPBS+. 1ml dual-labeled erythrocytes were added to the monolayer of HA-expressing cells and incubated for 15min at RT in the dark with gentle shaking. Unbound erythrocytes were removed by washing twice with 2ml DPBS+ and cells were added with 2ml DPBS+ adjusted with HCl to pH5 and incubated for 5min at 37°C. The acidic DPBS+ was replaced by 2ml DPBS+ with neutral pH and incubated for another 10min. Cells were then observed with an inverted fluorescence microscope (Zeiss, R18 channel: Excitation = BP 572/625 Emission =BP 629/662; calcein channel: Excitation: band pass filter 470/540, Emission: BP 525/50).

4.4.8 Flow cytometry

To compare the surface expression of M2 WT and mutants, total and surface expression levels of M2 fluorescence intensities were determined by flow cytometry. MDCK II cells grown in 6-well plates were infected with WSN WT and M2 mutants at an moi of 1. After infecting for 4.5h, cells were detached from the plates with trypsin/EDTA, recovered in growth medium for 30min and fixed with 4% formaldehyde for 20min. For measurement of surface M2, cells were directly treated with blocking solution for 30min. For analysis of total M2, cells were additionally permeabilized using 0.1% triton X-100 in PBS for 10 min before blocking. Cells were then incubated with primary anti-M2 mAb14C2 and secondary antibody anti-mouse Alexa Fluor 488 the same as described in immunofluorescence microscopy. The cells were analyzed in flow cytometry with the fluorescence intensity of each single cell was measured. At least 100000 cells were analyzed for each sample. Uninfected cells were used as negative control and its average fluorescence intensity was subtracted from infected cells done in parallel.

4.5 Microscopy

4.5.1 Immunofluorescence microscopy

To investigate the subcellular localization of M2 by immunofluorescence microscopy, MDCK II cells were grown in 6-well plates reaching a 90% confluence and infected with WSN WT and M2 mutants at an moi of 1. 4.5h post infection, cells were washed once with PBS, fixed with 4% (w/v) paraformaldehyde in PBS for 20min and permeabilized with 0.5% Triton X-100 in PBS for 10 min. After incubated with blocking solution for 1h, cells were added with anti-M2 mAb14C2 (1:300 in blocking solution) and incubated for 1h at room temperature. Washing with PBS (3X2min) was done to remove excessive primary antibody and cells were then incubated with fluorescent secondary antibody anti-mouse Alexa Fluor 488 (1:1000 in blocking solution) at room temperature for 30min. After washing, cells were recorded with a Zeiss Axio Vert A1 inverse epifluorescence microscope with emission at 488nm.

4.5.2 Negative staining electronic microscopy

To analyze to virus morphology by negative staining electronic microscopy, MDCK II cells in T175 flasks were infected with FPV* WT and CCM mutants at an moi of 0.001. The culture supernatant at 48h post infection was cleared from cell debris, pelleted through 20% sucrose cushion and resuspended in 1X TNE buffer.
(The following steps were done by Dr. Kai Ludwig at BioSupraMol, Chemistry and Biochemistry, FU Berlin) A copper grid (400mesh) was firstly hydrophilized by 60s glow discharging at 8 W in a BALTEC MED020 device. 5µl virus suspension was pipetted onto the

grid and incubated for 30s. After gently removing excessive fluid with a piece of filter paper, 5µl of the contrast enhancing heavy metal stain solution (1% phosphotungstic acid, pH 7.4) was added onto the grid and blotted for 45s. The excess fluid was removed again and the grid was dried by exposing to air for ~2h. After being transferred into the standard holder, viruses on the grid were imaged by a Tecnai F20 TEM microscope equipped with field emission gun and operating at 160 kV.

4.5.3 Transmission electronic microscope

To analyze the virus budding by transmission electronic microscope, MDCK II cells in T175 flasks were infected with WSN WT and M2 mutant viruses at an moi of 0.001. 24-36h after infection, living cells were scraped off from the flask and harvested together with culture supernatant. Cells were pelleted through centrifugation at 2000g for 5min at 4°C, washed twice with HEPES solution (pH 7.2) and fixed with 2.5% glutaraldehyde in 50 mM HEPES (pH 7.2). (The following steps were done by Dr. Lars Müller at Robert Koch Institute). After washing with HEPES solution, cell pellets were embedded at a ratio of 1:1 in 3% agarose with low melting point, post-fixed with 1% osmium tetroxide for 1h, with tannic acid [0.1 % in 50 mM HEPES (pH 7.2)] for 30min, with 2 % uranyl acetate for 2h, then dehydrated stepwise in a graded ethanol series and finally embedded in epon resin. Around 60nm-thick ultrathin sections were prepared with an ultramicrotome (Leica Ultracut UCT), which were counterstained with 2% uranyl acetate in ddH_2O for 20min, followed by lead citrate (Reynolds' solution for 3min). Ultrathin sections were examined using a JEM-2100 transmission electron microscope (JEOL) at 200 kV. Images were recorded using a Veleta CCD camera (EMSIS).

4.5.4 Confocal microscopy

To study apical transport of HA mutants LA, YK2A and LW2A, MDCK II cells were grown to polarized cells as previously described and infected with both virus WT (as control) and virus mutants at an moi of 1. After washing twice with PBS (both the apical membrane and basolateral surface), cells were fixed with 4% formaldehyde in PBS for 20min at 6h post infection. The membrane filter with cells were cut off from the transwell using a blade and put into 24-well plates. Cells were then blocked with 3% BSA in PBS for 30min, stained with primary anti-HA2 antiserum (1:500) and monoclonal antibody against β-catenin (basolateral marker, 1:500) for 2h, washed with PBS (5X2min), incubated with two secondary antibody anti-rabbit Alexa Fluor 568 (1:1000, for HA, Red) and anti-mouse Alexa Fluor 488 (1:1000, for β-catenin, green) for 1h.

To analyze the apical transport of the HA mutant YKLW4A, $5x10^5$ MDCK II cells were seeded onto the membrane filter of 24-mm transwells. The next day, cells were transfected with HA WT (as control) and HA YKLW4A from the upper chamber using Lipofectamine 3000 Reagent. 6h post transfection, the medium in the upper chamber was replaced by fresh DMEM supplemented with 2% FCS. Cells were cultured for another 4 days and medium was changed daily. 4 days later, cells were washed, fixed and cut off from transwell as described above. Before staining with primary antibody and secondary antibody, cells were additionally permeabilized with 0.5% Triton X-100 for 5 min.

Before imaging, the membrane was mounted on a glass slide by adding 40µl VectaCell™ Trolox Antifade Reagent and covered with a cover slip. Cell were imaged by the VisiScope confocal FRAP System equipped with iXon Ultra 888 EMCCD camera using 100X objective (1.45 NA). The fluorophores were excited via laser lined at 488nm (Alex Fluor 488) and 561nm (Alexa Fluor 568). Z-stacks with 0.5 µm increments were taken for polarized cells and images were analyzed with Image J software.

5 Results

5.1 Effects of CCM on HA's interaction with cholesterol, virus replication, assembly and HA's fusion activity

5.1.1 Reduction of HA cross linking to photocholesterol by mutations in the CCM

HA is composed of a large ectodomain, a flexible linker (9 aa) connecting to the transmembrane domain and a short cytoplasmic tail containing three conserved cysteine attached with fatty acids (15, 54). HAs are phylogenetically classified into two groups and only group 2 HAs accommodate a conserved CCM motif Y-K-L-W, in which YK are localized at the end of the flexible linker and LW at the beginning of the TMD (Fig. 5.1A)(80). The helical wheel plot of interested region suggests that the residues K, L and W are probably located on one helix of the HA trimer to bind cholesterol from one side while the aromatic residue Y on another helix contributing binding from the other side (Fig. 5.1B). This cholesterol binding model then resembles the one in human β2-adrenergic receptor, in which the amino acids R/K-I/V/L-W/Y are on one of the 7 transmembrane helices, whereas an aromatic residue F or Y is on another helix (45).

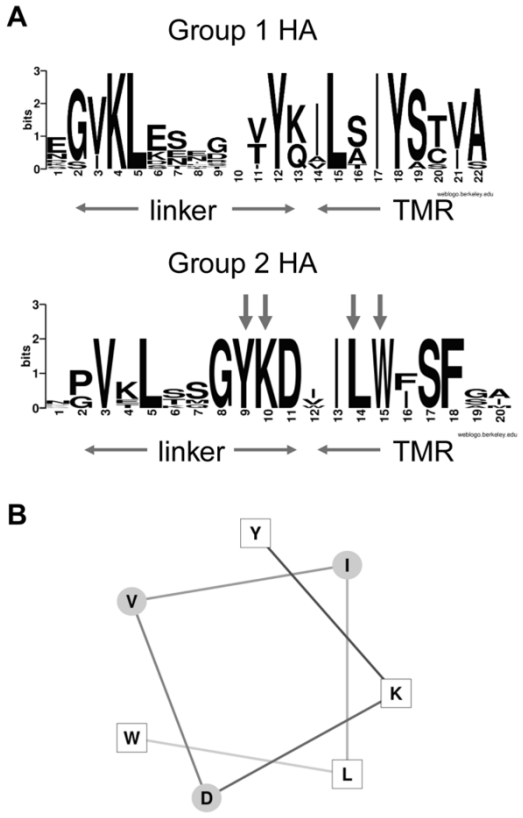

Fig. 5.1: Cholesterol concensus motif (CCM) in group 2 HAs. (A) Conserved CCM (Y-K-L-W) found in phylogenetic group 2 but not group 1 HAs. The sequence of every unique HA in the Flu database was extracted and classified into 2 HA subgroups. The linker region and N-terminal part of transmembrane region was aligned by the WebLogo 3.3 server (http://weblog-o.threeplusone.com/create.cgi) for group 1 and 2 separately. The overall height of the stack represents the sequence conservation, while the height of every letter indicates the relative frequency of one amino acid at that position. **(B)** The helical wheel plot of the amino acid sequence YKDVILW of HA subtype H7 (http://lbqp.unb.br/NetWheels/). The residues of CCM(YK…LW) are displayed as white squares.

Our previous studies (80) demonstrated that mutations in the CCM resulted in delayed transport of HA to the plasma membrane and decreased association with nanodomains enriched in cholesterol and sphingnolipids, but it is yet unknown whether HA interacts with cholesterol through CCM. Therefore I applied click-photocholesterol to our experiments, whose C5=C6 is replaced by a diazirine group at C6 and the terminal methyl group (C26) is changed to an alkyne group (Fig. 5.2A). The diazirine group, a photoactivatable chemical group, upon UV irradiation, would decompose into a nitrogen molecule and a highly active carbene intermediates, which form covalent bonds with side chains of amino acids in close proximity. In order to detect the covalently bound protein, an azide-fluorophore substrate was used here to react with the alkyne group upon catalyzation by copper. This reaction is called copper(I)-catalyzed azide-alkyne cycloaddition (CuAAC) reaction, a type of click reaction.

The photocholesterol-linked proteins were then separated in a SDS-gel and detected by a fluorescence gel scanner.

In this study I used H7 subtype HA from a mutant of fowl plague virus (FPV*) bearing a monobasic cleavage site instead of the original multibasic one. This allows later to work with recombinant viruses in a BSL2 lab instead of a BSL3 lab, which would be required for a highly-pathogenic influenza strain. I wanted to compare the HA wild type with the mutant YKLW4A whose four amino acids of the CCM are all mutated to alanine. Firstly I labeled HA in transfected CHO cells by incubating cells with photocholesterol for 16h followed by UV irradiation for 20 min. Then cells were lysed and divided into two aliquots, one subjected to western blot using anti-HA2 antiserum, another to immunoprecipitation and click reaction. I observed that HA WT was successfully labeled with cholesterol since no protein of the same molecular weight could be detected in mock tranfected cells and the mutant YKLW4A showed similar cholesterol incorporation as WT (Fig. 5.2C). However, YKLW4A had a much higher expression level in cells as shown by western blot (Fig. 5.2B). Therefore I quantified the band intensities and normalized fluorescence signal to total protein expression from this and five other identical experiments, which revealed that the cholesterol-bound HA YKLW4A was only 58% (±13%, mean of six transfections, Fig. 5.2D) of HA WT.

Since HA's association with nanodomains was reduced by mutations in the CCM (75, 80), the decreased incorporation of cholesterol into YKLW4A might be due to its insertion into cholesterol-depleted membrane domains, consequently there is less cholesterol in proximity of YKLW4A for the crosslinking reaction. To preclude this possible unspecific effect, HA WT and YKLW4A were firstly immunoprecipitated from cell lysates and then labeled with photocholesterol by crosslinking followed by click reaction (Fig. 5.2 D+E). Results showed an even higher reduction of cholesterol-bound YKLW4A, only 38% (±5%, mean of four transfections) relative to HA WT.

To investigate whether the smaller changes in the CCM might also affect HA crosslinking with cholesterol, I expressed two double mutated HAs (YK2A and LW2A) and one single mutated HA (LA), all of which showed retarded transport and decreased integration into nanodomains in a previous study (80), in CHO cells and did photocholesterol labeling as described before. However, they did not show significant reduction in binding to cholesterol (Fig. 5.2 F+G), which indicates that in order to decrease the association between HA and photocholesterol, the whole CCM motif needs to be mutated.

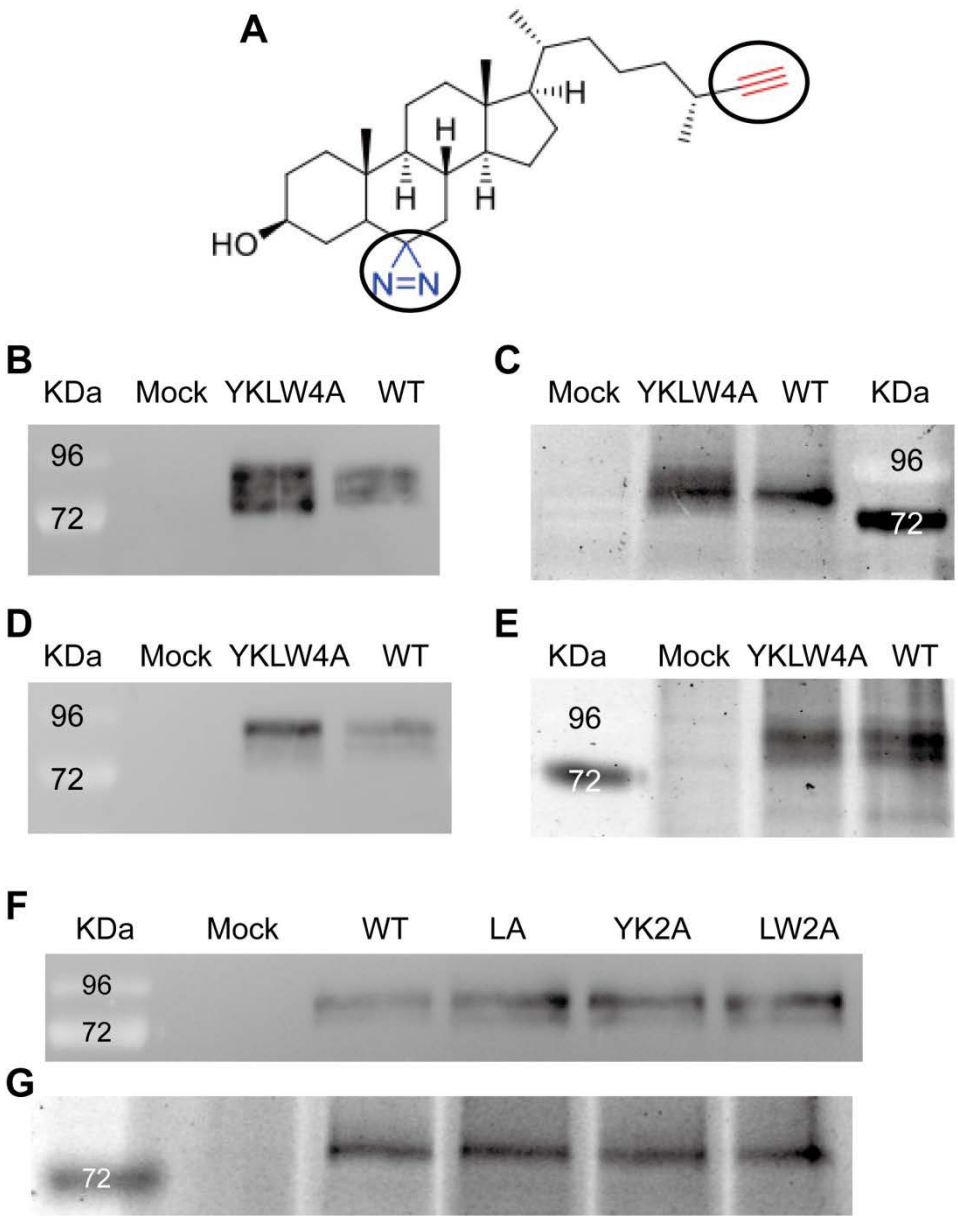

Fig. 5.2: Photocholesterol labeling with HA WT and CCM mutants. (A) Structure of click-photocholesterol (6,6-Azo-27-Alkin-Cholesterol). The encircled parts are the two functional group, diazirine (blue) and alkyne (red) group. **(B+C)** Labeling in CHO cells expressing HA WT or HA YKLW4A. CHO cells transfected with HA WT or YKLW4A were labeled with photocholesterol for 16h, exposed to UV light and lysed in 500µl 1% triton. 50µl lysate was subjected to western blot using anti-HA2 antiserum (B); the left 450µl was immunoprecipitated with the same antiserum, followed by click reaction, loaded to SDS-Gel and scanned by fluorescence scanner (C). Determination of the band intensities of this and five other experiments revealed that cholesterol-labeling of HA YKLW4A was reduced to 58 (±13%) relative to HA WT if their different expression levels are taken into account. Mock: untransfected cells. kDa: molecular weight markers. **(D+E)** Labeling with immunoprecipitated HA WT or HA YKLW4A. CHO cells were lysed in 500µl 1% triton after transfection with HA WT or YKLW4A for 24h. 50µl lysate was subjected to western blot (E). The left 450µl lysate was immunoprecipitated to get the antibody-HA complex which was then incubated with photochoesterol, exposed to UV light, clicked with azide-Cy3, subjected to SDS-PAGE and detected by fluorescence scanning (F). Quantification of this and three other experiments revealed that cholesterol-labeling of HA YKLW4A was reduced to 38 (±5%) relative to HA WT. **(F+G)** Labeling in CHO cells expressing HA WT, HA LA, HA YK2A or HA LW2A. Experiment was done the same as (B) and (C). Quantification of this and other two experiments revealed that cholesterol-labeling of HA LA was 92% (±11%) relative to HA WT, YK2A 99% (±30%) and LW2A 97% (±34%).

5.1.2 Impaired virus replication by mutations in the CCM

All previous experiments about the effect of mutations in the CCM of HA were limited to the protein level, whether virus growth might be impaired by those mutations is still in question. Therefore, I used a reverse genetics system to generate a mutant of fowl plague virus (A/FPV/Rostock/34, H7N1), named FPV*, whose multi-basic cleavage site in HA is mutated to a monobasic one. In this case, additional trypsin is required for virus growth and consequently virus could be manipulated in BSL-2 lab. I constructed the indicated HA mutants, each codon with all three nucleotide substitutions to exclude the possibility of reverting to WT. HA plasmids together with other 11 plasmids were then co-transfected into 293T cells to produce virus. The supernatant was subsequently transferred onto MDCK II cells for virus amplification and virus titer was determined by HA assay. The virus mutant YKLW4A could not be rescued in three independent trials, whereas FPV* WT and other three mutants LA, YK2A and LW2A done in parallel were successfully generated, showing HA titers of 2^5 -2^6. A virus stock was made by infection of MDCK II cells and sequencing of the HA gene segment showed the presence of desired mutations, but no other changes (data not shown).

I next analyzed the replication kinetics of virus WT and mutants by infecting MDCK II cells at a low moi of 0.0005 and the culture supernatant was harvested at indicated time points. Virus titer was determined by HA and TCID50 assay. The growth curve showed that less viruses were produced at all time points for mutants compared to WT (Fig. 5.3A) and especially LW2A had significantly lower (~1.5 log) infectious titer at 36h and 48h post infection (Fig. 5.3B).

I also compared the growth fitness of virus mutants with WT by co-infecting MDCK II cells with mutants and WT at a starting ratio of 5:1. An aliquot of culture supernatant at 24h and 48h post infection was taken from the culture dish and vRNA was extracted and sent for sequencing. Viral RNA of starting virus mixture regarded as 0h was also extracted and sequenced. The sequencing chromatograms of the mutated region in Fig. 5.3C demonstrated the presence of amino acid sequences of both WT and mutants at all times. As expected, the major virus component at 0h was mutants because of the higher inputting amount, but WT virus became predominant in the population at 24h and 48h. Although the peak height does not strictly correspond to the virus quantity, the obvious change in the sequence chromatograms suggested double mutants were quickly outgrown by WT in just a few virus generations.

Altogether, I conclude that the CCM is essential for virus replication. Substituting all the four residues of the motif impeded to rescue infectious viruses and exchanging two of them decreased virus titers and impaired their competitive fitness.

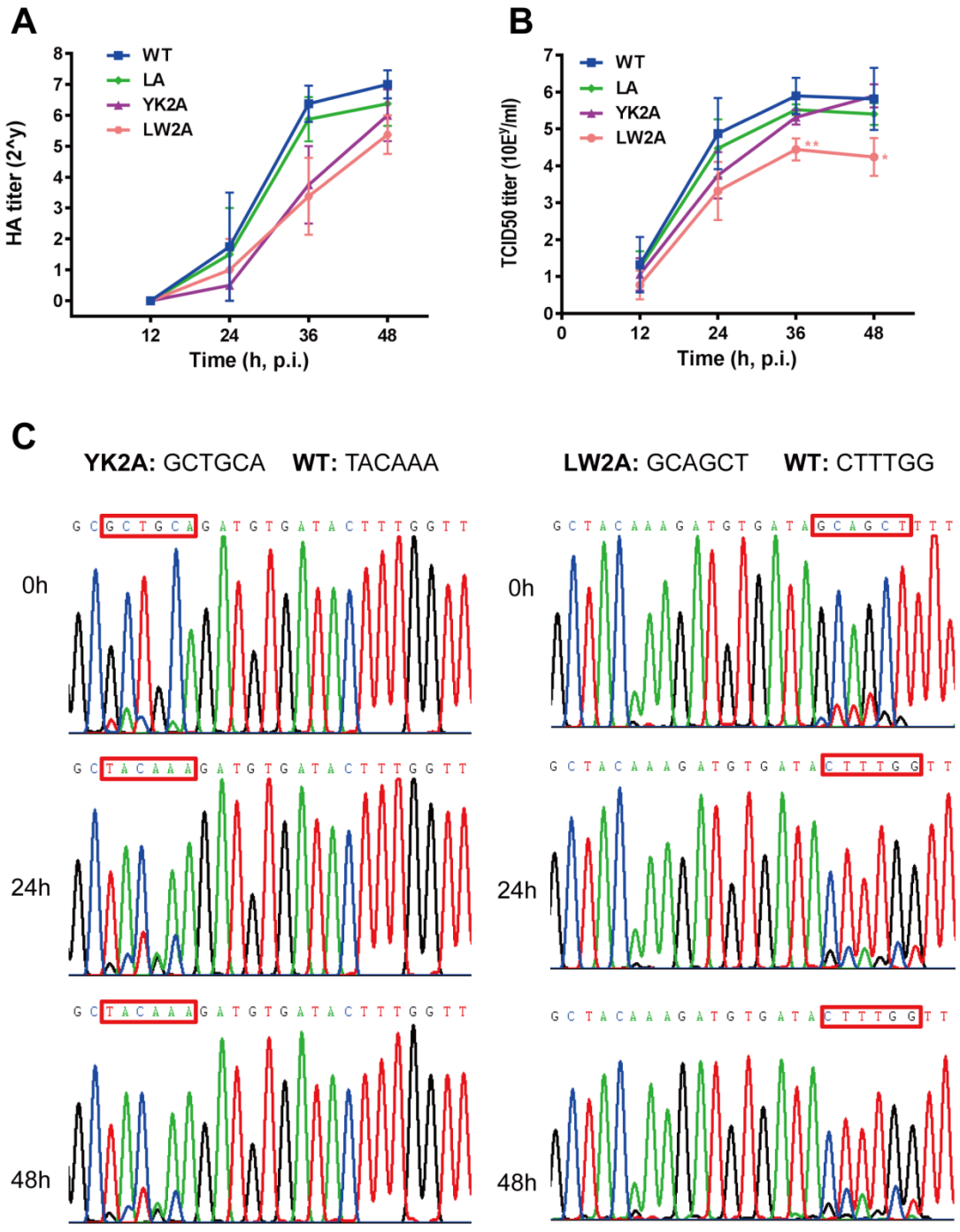

Fig. 5.3: Effect of mutations in the CCM on virus replication. (A+B) Growth curves of FPV* WT and FPV* mutants with indicated mutations. MDCK II cells were infected with viruses at an moi of 0.0005. Culture supernatants were harvested at 12h, 24h, 36h and 48h post infection and virus titer was determined by HA-assay (A) or TCID50 assay (B). Three independent experiments were done and data was displayed as means ± SD (standard deviation). Asterisk indicates statistically significant differences (* P<0.05, ** P<0.01) between FPV* WT and FPV* LW2A based on Student's t-test. **(C)** Competitive growth of FPV* WT and double mutated viruses. MDCK II cells were infected with virus mutants (left: YK2A; right: LW2A) and WT at a ratio of 5:1 (total moi of 0.0005). Culture supernatants were harvested at 24h and 48h post infection. The starting virus mixture was set as 0h. The viral RNA of all these samples was isolated, subjected to RT-PCR and sent for sequencing. Sequencing chromatograms of desired cDNA region were shown and nucleotides corresponding to the mutated amino acids were circled with red square.

5.1.3 Virus apical budding and HA apical transport is not disturbed by mutations in the CCM

In polarized epithelial cells, the assembly and budding site of IAV is in the apical membrane (114), where HA is also transported to and the apical transport signal of HA is located in the TMD (83). To determine whether mutations in the CCM might affect HA's transport to the apical surface, I infected polarized MDCK II cells grown on filter membranes for 5 days with FPV* WT and mutants LA, YK2A and LW2A at low moi. The culture medium of both upper (apical) and lower (basolateral) chamber was collected at indicated time points and the virus titer was measured by HA assay.

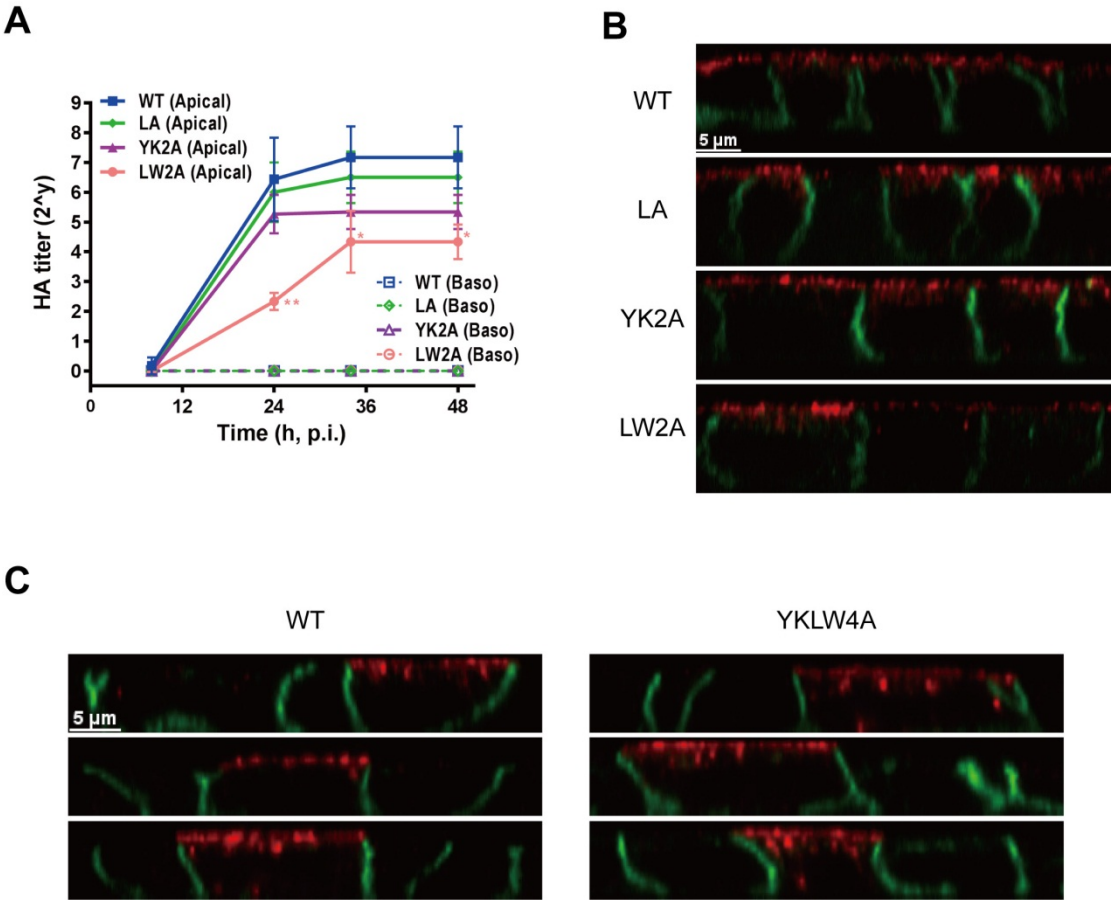

Fig. 5.4: Effect of mutations in the CCM on apical virus budding and transport of HA in polarized cells. (A) Budding of FPV* WT and mutants in polarized MDCK II cells. Polarized MDCK II cells were infected with viruses at an moi of 0.001. Culture medium was harvested from both upper (apical) and lower (basolateral) chamber at 8h, 24h, 34h and 48h after infection. Virus titer was measured by HA assay. Asterisk indicates statistically significant differences (* $P<0.05$, ** $P<0.01$) between FPV* WT and FPV* LW2A based on Student's t-test. **(B)** Apical transport of HA mutants LA, YK2A and LW2A in polarized MDCK II cells. Polarized MDCK II cells were infected with viruses at an moi of 1. After infection for 6 hours, cells were fixed, incubated with antiserum against HA2 and antibody against basolateral marker β-catenin and stained with fluorophor-coupled secondary antibody Alexa Fluor 568 (red for HA) and Alexa Fluor 488 (green for β-catenin). **(C)** Apical transport of HA YKLW4A in polarized MDCK II cells. MDCK II cells were transfected with HA YKLW4A or HA WT one day after seeded into 24mm transwell. 4 days after transfection, cells were fixed, permeablized and stained with primary and secondary antibody as explained in (B). Z-stacks with 0.5µm increments of polarized MDCK II cells were combined and shown in (B) and (C). Since cells were permeablized, intracellular staining is evident in (C), particularly for YKLW4A.

The results of the growth curve (Fig. 5.4A) revealed that both virus WT and mutants were released predominantly from apical membranes. As in the previous experiment, all the virus mutants grew to lower titers than WT, LW2A exhibiting a significant reduction. No detectable viruses were released into basolateral chamber. Nevertheless, IAVs are reported to exclusively bud from the apical membrane despite that a portion of HA is transported to the basolateral membrane (84, 85). Therefore, I also investigated the membrane location of HA mutants LA, YK2A and LW2A in virus infected cells and of HA YKLW4A in transfected cells with confocal microscopy. Nonetheless all the HA mutants were entirely localized in the apical membrane, the same as HA WT, since no colocalization of HA and β-catenin, the basolateral membrane marker, was detected (Fig. 5.4B+C). Thus, HA transport to the apical membrane is not disturbed by mutations in the CCM.

5.1.5 Reduction of HA and cholesterol incorporation into virions by mutations in the CCM

In principle, the impaired virus replication might be the result of a defect in virus entry into cells or in virus assembly and budding. Our previous studies have shown that mutations in the CCM reduced HA surface expression and association with membrane rafts (80), which might in turn affect HA incorporation into released virions. Therefore, I harvested FPV* WT and FPV* LW2A viruses from infected embryonated chicken eggs, purified them by continuous sucrose gradient centrifugation, separated them by non-reducing SDS-PAGE and stained with coomassie to analyze the viral protein composition. Viral major proteins HA, NP and M1 could be clearly seen for FPV* LW2A as FPV* WT (Fig. 5.5B). However, after analyzing the band intensity and calculating the viral protein ratios, FPV* LW2A showed less HA amount than WT, 15% reduction when normalized to NP and 18% to M1. I also analyzed viruses harvested from MDCK II cells and FPV* LW2A showed a more pronounced decrease in HA amount, 38% reduction in HA/NP ratio and 41% HA/M1 ratio. FPV* LA and YK2A also incorporated less HA compared to NP or M1 than WT although to a less extent (Fig. 5.5D).

Previous studies showed that mutations in the CCM resulted in decreased association with membrane rafts, where HA concentrates and the virus assembly and budding occurs. Fig. 5.2 also revealed a reduction in HA interaction with cholesterol by mutations in the CCM, therefore cholesterol incorporation into virions might be affected as well. Considering this, I analyzed the cholesterol content in virus mutants and WT purified by sucrose gradient. Three virus preparations were applied for analysis and the determined cholesterol amount was normalized to that of total protein. FPV* WT showed a mean value of 220 nM cholesterol per ng/µl total protein, but variations in ratio of cholesterol to protein among different preparations was seen for both WT and mutants. Nonetheless, when comparing mutants with WT of the same preparation (shown as the same color in Fig. 5.6A), virus mutants always incorporated less cholesterol than WT, except LA in one preparation. The cholesterol content was reduced to 89% of WT in LA, 88% in LW2A and to 82% in YK2A (Fig. 5.6B). One group has used mass spectrometry to analyze the lipidomics of IAVs grown in MDCK II cells, the same cell type I used in this study, and found that the cholesterol in virions is 52 mol% in relation to all other lipids (28). Based on this, the cholesterol amount in virus mutant LA and LW2A is reduced to 46 mol% and in YK2A to 43 mol%, which resembles the percentage of cholesterol in apical membranes of polarized MDCK II cells (28). Therefore, our results indicate that mutations in the CCM might render viruses to assemble and bud from the bulk phase of the surface membrane instead from the membrane nanodomains enriched in cholesterol and sphingolipids.

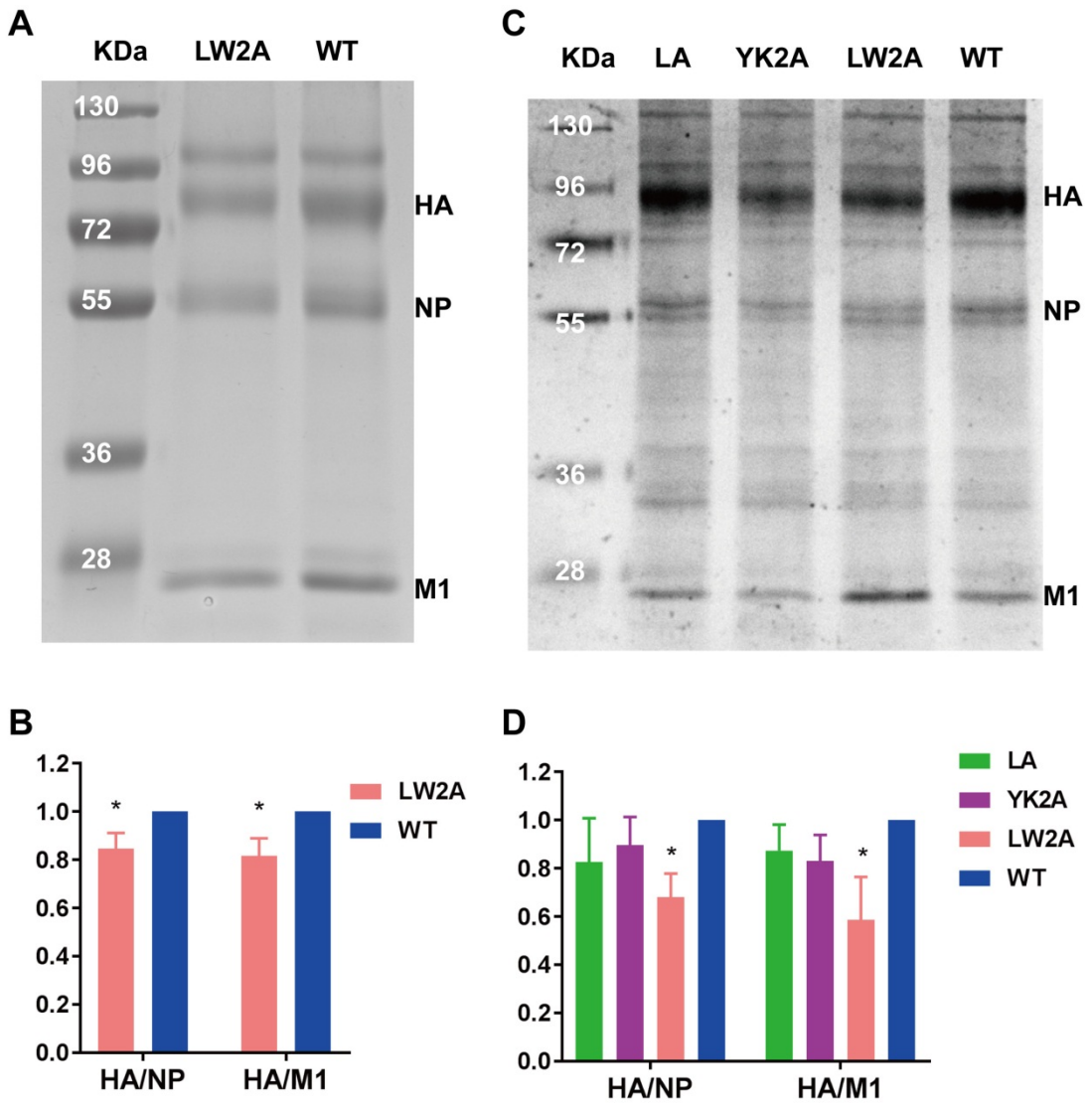

Fig. 5.5: Effect of mutations in the CCM on HA incorporation into virus particles. (A+C) Viral protein compostion of FPV* WT and indicated mutants purified from embryonated chicken eggs (A) and MDCK II cells (C). Sucrose-gradient-purified viruses were subjected to non-reducing SDS-PAGE and stained with coomassie. The position of major bands is shown at the right of the gel and molecular mass markers (kDa) at the left. **(B+D)** Comparison of relative amount of HA. Band density of HA, NP and M1 was measured by Image J. The ratio of HA/NP or HA/M1 was calculated and normalized to WT. Results from three different virus samples were shown as mean ± SD. Asterisk indicates statistically significant differences (* $P<0.05$) between FPV* WT and FPV* LW2A based on Student's t-test.

Defect in assembly might affect virus morphology, so I also analyzed the morphology of our mutants with negative staining electronic microscopy. No obvious difference in morphology and size was observed for double mutated viruses YK2A and LW2A (Fig. 5.6 D+E). Although HA spikes could be clearly seen in mutants, to measure the probable reduction in density of HA spikes in mutated virions (considering the decreased HA incorporation into purified virions by SDS-PAGE) needs more sophisticated methods, such as counting virus spikes in Cryo-EM pictures.

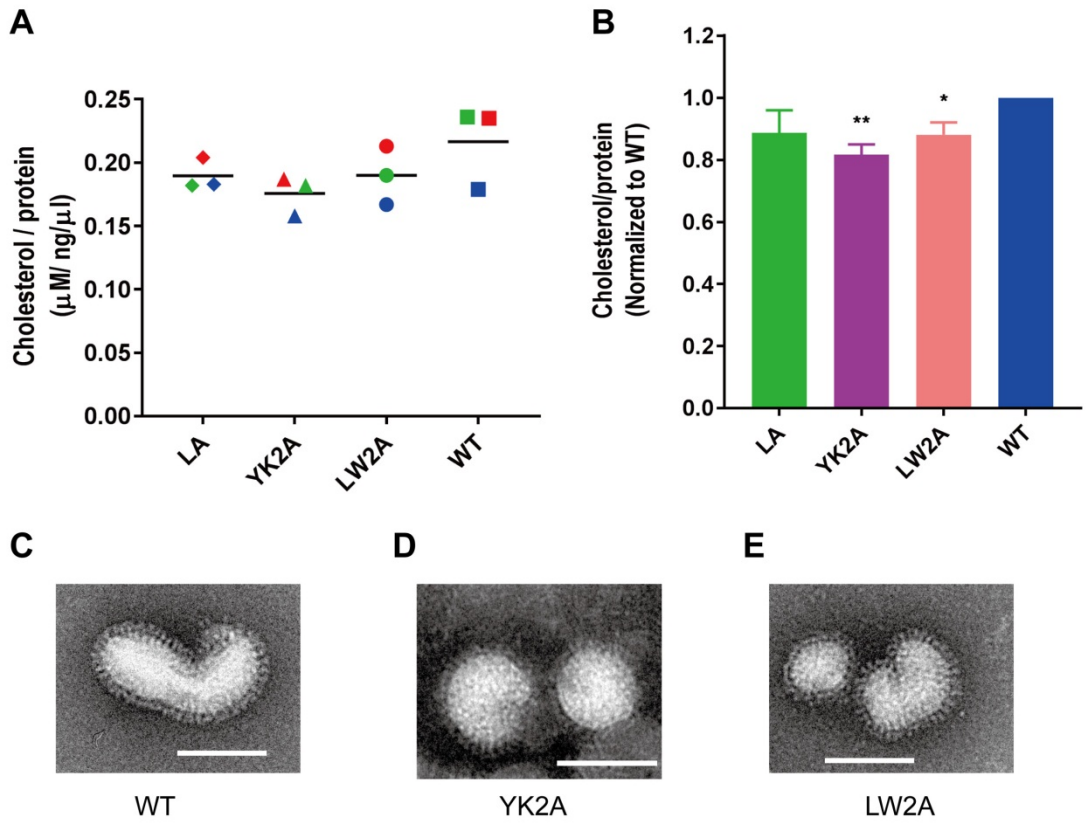

Fig. 5.6: Effect of mutations in the CCM on cholesterol content and virus morphology. **(A)** Cholesterol amount in purified FPV* WT and mutants. It is shown as the cholesterol concentration (µM) divided by viral total protein concentration (ng/µl) for each virus. The horizontal bar is the mean of three independent measurements shown with different color, whereas the same color indicates viruses were analyzed in parallel. **(B)** Normalized cholesterol amount (WT as 100%) of FPV* CCM mutants. Asterisk indicates statistically significant differences (* P<0.05, ** P<0.01) between FPV* WT and FPV* mutants YK2A and LW2A based on Student's t-test. **(C-E)** Representative images of FPV* WT (C), FPV* YK2A (D) and FPV* LW2A (E) from negative staining electron microscopy. The scale bar equals to 100 nm. Viruses were collected from MDCK II cells and purified through 20% sucrose cushion.

5.1.6 Decreased hemolysis activity by mutations in the CCM

HA mediates the fusion between viral and cell membranes. Thus, I also analyzed whether impaired growth of virus mutants might be due to their decreased fusion capability. Virus mutants and WT were diluted to the same HA titer of 2^6. This is essential since the higher HA amount in FPV* WT would lead to higher extent of membrane fusion. The fusion ability was compared by a well-established hemolysis assay where the released hemoglobin (measured in a spectrometer) is positively correlated with membrane fusion.

Firstly I analyzed the optimal fusion pH for WT and mutants by performing hemolysis at the pH range from 5 to 7. At pH below 5 erythrocytes lyse spontaneously. Virus-induced release of hemoglobin started at pH 5.7 and increased with acidification for both WT and mutants (Fig. 5.7A). However, compared to WT each mutant showed a ~70% reduction in the amount of released hemoglobin at all pH values. I next compared the hemolysis kinetics by incubating samples up to 4 hours at pH5. All the viruses showed a linear increase of hemoglobin release with time, nevertheless at each time point the amount of released hemoglobin was less for all the mutants compared to WT (Fig. 5.7B).

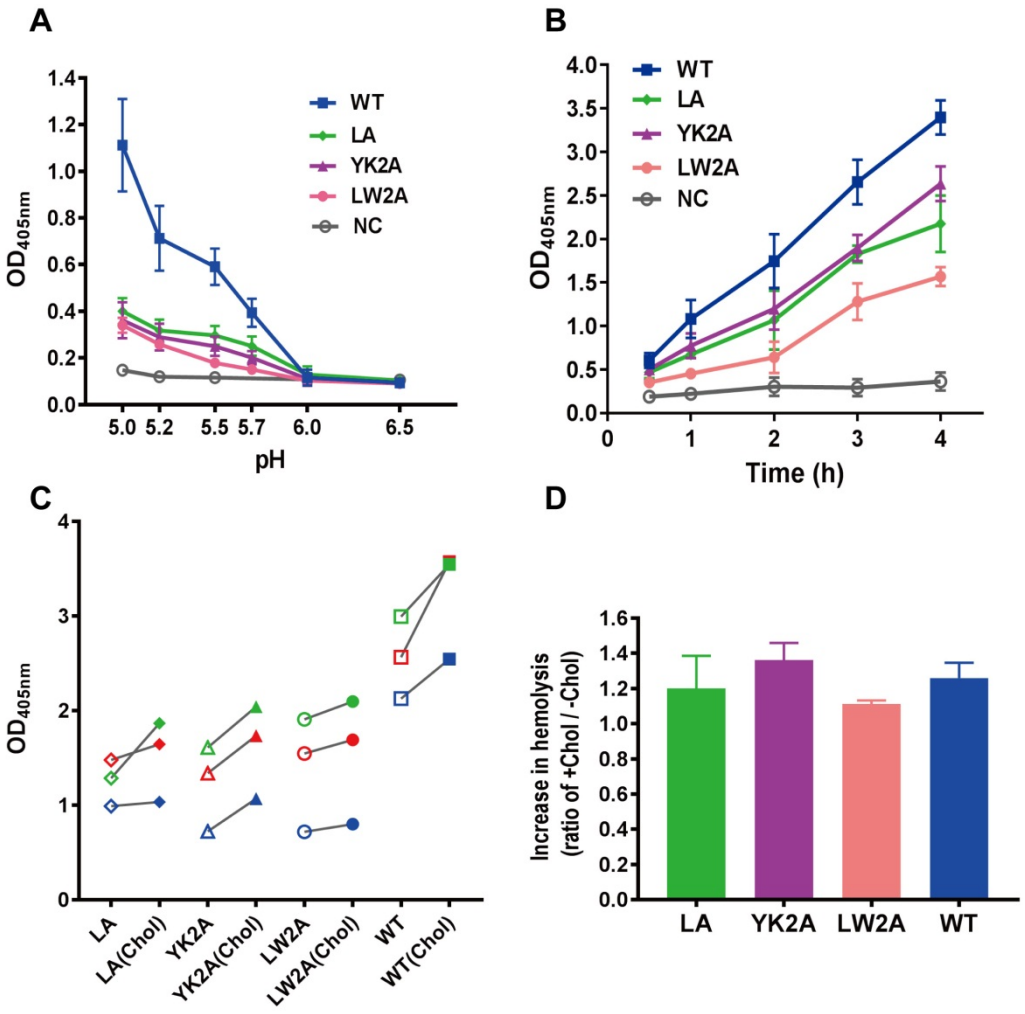

Fig. 5.7: Effect of mutations in the CCM on hemolysis. (A) pH dependence comparison between FPV* WT and mutants. Viruses diluted to the HA titer of 2^6 were added with chicken erythrocytes, adjusted to the indicated pH and incubated at 37°C for 1h. The amount of released hemoglobin (OD_{405}) was plotted against pH. PBS was used as negative control (NC). Results from three independent measurements are shown as mean ± SD. **(B)** Hemolysis kinetics comparison. Virus were incubated with chicken erythrocytes after pH5 treatment for indicated time length and the released hemoglobin was measured. Results from three independent measurements are shown as mean ± SD. **(C+D)** Comparison of hemolytic activity before and after supplemented with exogenous cholesterol for FPV* WT and mutants. Viruses with an HA titer of 2^8 were incubated with chicken erythrocytes at pH5, 37°C for 1h. (C) The exact OD_{405} value of before (open symbol) and after (filled symbol) cholesterol addition from three independent measurements. (D) Increase in hemolysis activity normalized to untreated viruses. Results from three independent measurements are shown as mean ± SD.

Depletion of cholesterol from viral membrane was shown to decrease HA's fusion activity, and vice versa (61, 63). In theory, the decreased fusion activity of mutated viruses could be due to either the changed biophysical properties of viral membrane resulting from the reduction of its cholesterol content or innate defect in HA's membrane fusion activity. To test both possibilities viral membranes were supplemented with exogenous cholesterol by incubating purified virus with cholesterol-MβCD complex. To check whether this treatment increased the cholesterol content, I measured cholesterol of virus samples before and after treatment. All the virus mutants had an increase of ~20-35% in the cholesterol amount after incubation with cholesterol-MβCD complex, reaching a similar or slightly higher content compared to untreated FPV* WT. Then I compared hemolysis kinetics of viruses before and

after addition of cholesterol. Both WT and mutants showed an increase of 10% to 35% in the amount of released hemoglobin after cholesterol addition (Fig. 5.7C), confirming that cholesterol could promote membrane fusion. However, the cholesterol-supplemented mutants still showed a lower hemolysis activity than the original WT virus (Fig. 5.7C+D), which indicates that the fusion defect remains in virus mutants in spite of the similar cholesterol content as WT virus.

5.1.7 Decreased hemifusion activity by mutations in the CCM

Hemoglobin release caused by fusion between erythrocytes and viruses demands both lipid mixing and the opening and widening of fusion pores. Thus using a hemolysis assay one could not specify which step is affected. It has been reported for some HA mutants that these two steps are not coupled. An example is the GPI-HA whose transmembrane domain is replaced by a glycolipid anchor (51). GPI-HA executes only hemifusion, but not full fusion. To investigate whether mutations in the CCM of HA would affect hemifusion, I performed R18 dequenching assay in which the lipid mixing between viruses and erythrocyte ghosts was monitored. Viral membrane was labeled with the lipophilic dye octadecyl rhodamine B Chloride (R18) at a high self-quenching concentration and viruses with an HA titer of 2^10 were incubated with erythrocyte ghosts. After exposure to acidic solution to activate HA's fusion activity, the two membranes started to mix such that R18 would spread from the small viral membrane to the much larger ghost membrane. This resulted in an increase in fluorescence intensity that was recorded by fluorescence spectrometry. When there was no further fusion, detergent was added to lyse the membrane giving a maximal (=100%) fluorescence intensity.

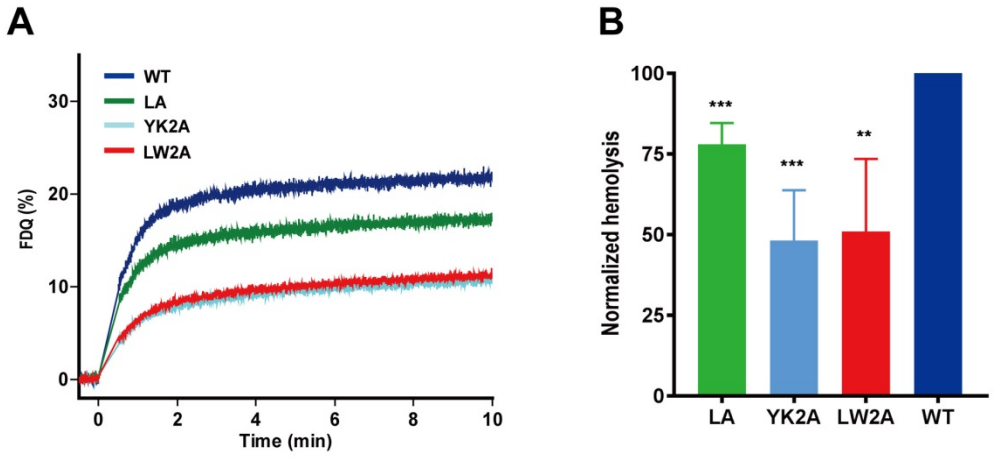

Fig. 5.8: Effect of mutations in the CCM on hemifusion. (A) R18 dequenching assay. Viruses adjusted to an HA titer of 2^10 were incubated with erythrocyte ghosts labeled with lipophilic fluorophore R18. Fusion was performed at pH5. Relative fluorescence dequenching (FDQ) is plotted against time. The graph exhibits the mean of four independent measurements with two different virus preparations. **(B)** Relative fusion extent using FDQ at 10min with WT normalized to 100%. Results from four independent measurements are shown as mean ± SD. Asterisk indicates statistically significant differences (* P<0.05, ** P<0.01, *** P<0.001) between FPV* WT and FPV* mutants based on Student's t-test.

Fig. 5.8A demonstrates the mean relative fluorescence intensity of four independent fusion measurements plotted against time. For both FPV* WT and mutants the fluorescence intensity increased rapidly after lowering the pH to 5 and became steady after ~2 min. However, the maximal fusion activity of virus mutants is much less than that of WT. When normalized to WT, double mutated viruses YK2A and LW2A showed a severe reduction to 50%, whereas in LA it was reduced to 75% (Fig. 5.8B). Similar reduction was also observed at pH 5.5 (not shown), indicating that the hemifusion activity of HA is affected by mutations in the CCM.

5.1.8 Defect in hemifusion by complete mutation of the CCM

It is of high interest now whether the HA mutant YKLW4A whose four amino acids of CCM are all exchanged to alanine exhibits any membrane fusion activity. Since no virus could be generated with this mutant, I expressed HA YKLW4A as well as HA WT in CHO cells by transfection and analyzed their fusion activity in a cell-to-erythrocyte fusion system. Erythrocytes labeled with both R18 and a water soluble fluorophore calcein-AM were incubated with HA-expressing cells. They were subsequently treated with protease to cleave HA0 into HA1 and HA2 and with acidic buffer to activate HA to the fusion state. Once fusion happens, the state of hemifusion (R18 diffuses from erythrocyte membrane to cellular membrane showing red ring in HA expressing CHO cells) and full fusion (calcein is also successfully diffused from erythrocytes to the cytosol of CHO cells giving a green color) could be identified by fluorescence microscopy.

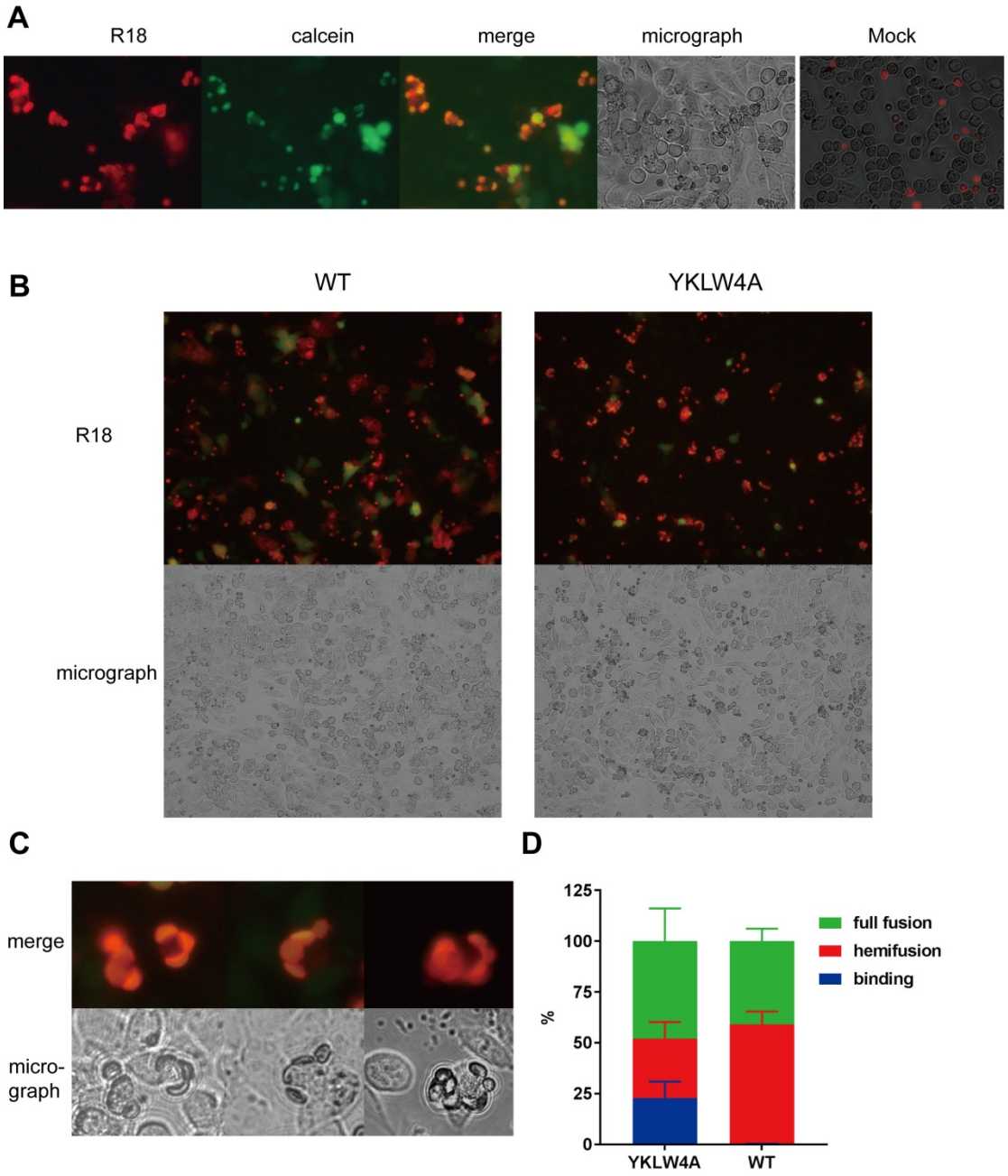

Fig. 5.9: Effect of complete exchange of the CCM on fusion of cells to erythrocytes. Cell-to-cell fusion between HA YKLW4A or WT expressed CHO cells and erythrocytes labeled with membrane marker R18 and cytosol marker calcein. 24h post transfection, HA expressed CHO cells

were treated with protease trypsin, incubated with dual-labeled erythrocytes, washed with DPBS++, treated with acidic buffer of pH5, neutralized and observed under fluorescence microscope. **(A)** Images from fluorescence microscope (40X magnification) showing diffusion of R18 (red, hemifusion) to the cellular plasma membrane and calcein (green, full fusion) to the cytosol of CHO cells expressed with HA YKLW4A. Mock: cells transfected with empty plasmid showing erythrocytes (not completely washed away) sitting randomly in the space between cells instead of binding tightly to cells. **(B)** Representative images to compare the number of fusion events between HA WT and HA YKLW4A at 20X magnification. The lower two micrograph images show similar number of erythrocytes were bound to cells expressing HA YKLW4A as those expressing HA WT. **(C)** Three different examples of HA YKLW4A expressed cells show erythrocytes only bound to cells but not proceeded to hemifusion and full fusion. **(D)** Percentage of specific fusion events of cells expressed with HA WT or HA YKLW4A. Three independent transfections were performed and in each transfection at least 100 cells bound with at least two erythrocytes were selected for analysis. Three different fusion stages, binding (=unfused erythrocytes), hemifusion and full fusion, were observed and the number of events of each stage was calculated with all the fusion events normalized to 100%. Results were shown as mean ± SD for each stage.

Both hemifusion (cells in the upper left of Fig. 5.9A) and full fusion (the cell in the right middle of Fig. 5.9A) were observed with YKLW4A-expressing cells, indicating exchanging the whole CCM to alanine does not completely abolish its full fusion activity. However, obviously less fusion events were identified with YKLW4A compared to WT as shown in Fig. 9B. One should also notice that similar numbers of erythrocytes were bound to cells expressed with YKLW4A as WT (micrograph in Fig. 9B), and thus the decreased surface expression of KLW4A is not the reason for reduced fusion events.

Additionally I observed a rather peculiar phenomenon with YKLW4A that is unfused erythrocytes still bound to transfected cells after low pH treatment, which performed neither hemifusion nor full fusion (Fig. 5.9C). Erythrocytes remained cell-bound even after an incubation time of 15min at pH5 (data not shown).

Later, I selected out more than 100 cells bound to at least two erythrocytes and determined whether they went through hemifusion, full fusion or no fusion (only bound erythrocytes). I then calculated the percentage of each fusion stage for both WT and YKLW4A and normalized the total number of analyzed cells to 100%. Cells expressing HA WT never showed binding of unfused erythrocytes after acidification, 58% of erythrocytes showed hemifusion and 42% full fusion. In cells transfected with HA YKLW4A, a similar percentage of erythrocytes (45%) proceeded to full fusion, 28% underwent hemifusion but around 20% were stuck at the binding stage (Fig. 5.9D).

I conclude from these results that complete exchange in the CCM cause a defect in HA's hemifusion activity, and probably also in steps before lipid mixing.

5.2 The replacement of amphipathic helix in M2 affects virus replication, assembly and M2's surface expression

5.2.1 The presence of an amphipathic helix in M2 cytoplasmic tail is essential for virus replication

To investigate the role of the amphipathic helix (AH) in the cytoplasmic tail (CT) of M2 for replication of the spherical Influenza virus strain A/WSN/1933 (H1N1), I constructed several M2 mutants with mutations in the AH region. To investigate whether AH is essential for virus replication, I deleted the AH-forming residues 48-62 from M2. This should cause only a slight disturbance to its proton channel activity since it only demands residues 21-51 of the protein (70). To test whether amphiphilicity of AH is important for M2's membrane-curvature-inducing function, I replaced the AH with two scrambled M2 sequences, one is from the particular WSN strain (sWSN, KYGCFRYFIKRGKLR) and the other from the Udorn strain (sUdorn, FFKLGYLEFKIFRGCRH), which is not able to cause membrane budding any more in contrast to its original unchanged peptide. To analyze whether a certain amino acids

composition of AH is required for this function, I also exchanged the residues in the region with three different amphipathic-helix-forming peptides; the curvature binding ALPS helix from ArfGAP 1 protein (ALPS, FLNSAMSSLYSGWSSFTTGASKFAS), the curvature inducing α0-helix of ENTH domain from Epsin 1 protein (Epsin, SSLRRQMKNIVHN) and a synthetic cell-penetrating peptide RW16 (RW16, RRWRRWWRRWWRRWRR) that has been shown to induce vesicle budding in GUVs (89).

A

B

	Sequence	<μH>	<H>
M2 WT	^{45}RLFFKCIYRRFKYGLKRG^{63}P	0.39	0.39
ΔAH	^{45}RLF----------P		
sWSN	^{45}RLFKYGCFRYFIKRGKLRP	0.11	0.39
sUdorn	^{45}RFFKLGYLEFKIFRGCRHP	0.32	0.52
ALPS	^{45}RLFFLNSAMSSLYSGWSSFTTGASKFASP	0.31	0.54
Epsin	^{45}RLFSSLRRQMKNIVHNP	0.61	0.25
RW16	^{45}RLFRRWRRWWRRWWRRWRRP	0.98	0.31

C

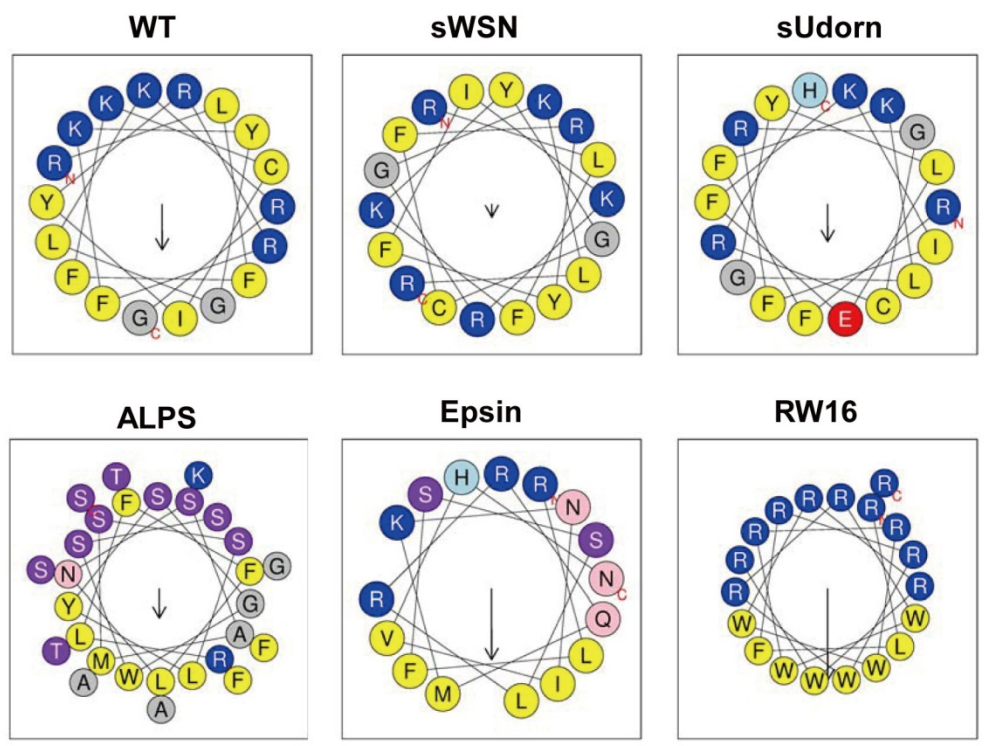

Fig. 5.10: The structure of M2 protein and characterization of amphipathic helices. (A) The structure of M2 protein with each domain indicated. **(B)** The amino acid sequences of the amphipathic helix region in M2 of WSN strain and indicated peptides used in the study. The amino acids different from M2 WT are shown in blue. Hydrophobic moment <μH> and hydrophobicity <H> were calculated in heliquest (http://heliquest.ipmc.cnrs.fr/). **(C)** Helical wheel plot of studied peptides in (B), but the residue P63 is excluded. The length of the arrow, pointing to the hydrophobic face, corresponds to the hydrophobic moment <μH>.

AH is a common feature found in many proteins and could be discriminated based on two parameters, the hydrophobic moment <μH> and the hydrophobicity <H> (115). The former parameter informs us about the amphiphilicity of a peptide presenting two opposing faces, hydryophobic and polar face. The latter suggests the general affinity of AH for lipids. Characterizing these AHs by these two parameters (Fig. 5.10B+C) revealed that M2 WT has a <μH> value of 0.39 and <H> of 0.39. The scrambled version, sWSN, though keeping the same <H> value as WT (since they share the same amino acids), holds a much lower <μH> value (0.11). The sUdorn has similar hydrophobic moment (0.32) as WT but a higher <H> value (0.52), but one should notice that the negatively charged residue glutamic acid is in its hydrophobic face. ALPS possesses similar values as sUdorn (<μH>= 0.31 and <H>= 0.54), while higher <μH> value (0.61) but lower hydrophobicity (0.25) is maintained by Epsin compared to WT. RW16, with a modest hydrophobicity (0.31), has the highest <μH> value (0.98) since the peptide is only composed of basic arginine residue and hydrophobic tryptophan residue, which are perfectly separated into the polar and hydrophobic face, respectively.

Next, I tried to generate viruses by co-transfecting the mutated M segment into 293T cells together with the other seven plasmids. Culture supernatants was harvested and passaged onto MDCK II cells for further amplification and the released virus particles were analyzed by HA assay. No virus could be rescued when the AH was deleted or replaced with sWSN in five independent transfections. In contrast, the virus with sUdorn, ALPS, Epsin and RW16 could be successfully generated as WT, giving an HA titer of 2^2 to 2^6, which indicates the structural amphipathic helix in the cytoplasmic tail is essential for virus replication.

5.2.2 Viruses show defect in replication when AH is replaced with others.

To compare the replication of virus mutants with wild type, I infected MDCK II cells with viruses at a low moi of 0.001. Culture supernatant was harvested at different time points and virus titer was measured by plaque assay (Fig. 5.11A). All the viruses showed a similar growth pattern as WT reaching the highest titer at 34h post infection (Fig. 5.11A), but they grew to statistically significant lower titer than WT, about 1 log lower for ALPS, Epsin and RW16, whereas at least 3 logs lower for sUdorn. To compare the number of total released virions at 34h post infection (which gave the highest PFU titer), I applied RT-qPCR using primers against viral RNA segment M and NA separately. The vRNA copy number from RT-qPCR was then divided by the infectious PFU titer to analyze the ratio of infectious to total virions (Fig. 5.11B), which is ~0.1 for virus WT when segment M was considered and ~0.2 with segment NA. When comparing virus mutants with WT, virus Epsin had a similar ratio, while the other three mutants was 3-5 times lower regardless of segment M or NA considered. That means the virus mutants ALPS, RW16, and sUdorn have relatively high amount of non-infectious virus, which suggests that their assembly process is less accurate.

Virus replicate several times when infecting at a low moi of 0.001, so the reduced titer of mutants could result from either a defect in virus budding, in virus entry or both. Therefore, I compared virus growth in only one replication cycle by infecting cells with a high moi of 1 and measuring the virus titer of samples collected at 6h and 9h post infection by plaque assay. In contrast to the growth with multi-replication cycle, all virus mutants revealed slight but not statistically significant reduction in virus titer, only sUdorn and ALPS showed 1 log significantly lower titer at 6h post infection than WT (Fig. 5.11C). This result suggests that AH replacement in M2 only cause minor defect in virus genome replication and virus budding. The reduction of virus titer in replication with multiple cycles might be due to the defect in virus entry, especially for virus mutant sUdorn.

The cytoplasmic tail of M2 contains a LC3 binding site and could interact with the autophagy protein LC3, which is required to maintain virus stability (116). M2 also interacts with cholesterol, a lipid promoting membrane rigidity and accordingly might maintain stability of virus. To investigate whether the stability of virus mutants is affected by AH replacement, $1x10^5$ infectious viruses were incubated in infection medium without cells at 37°C for 4 days

and one aliquot was taken out per day to measure its remaining infectivity. Nevertheless, virus WT and mutants showed much-alike stability, each day ~80% of the viruses losing their infectivity (Fig. 5.11D).

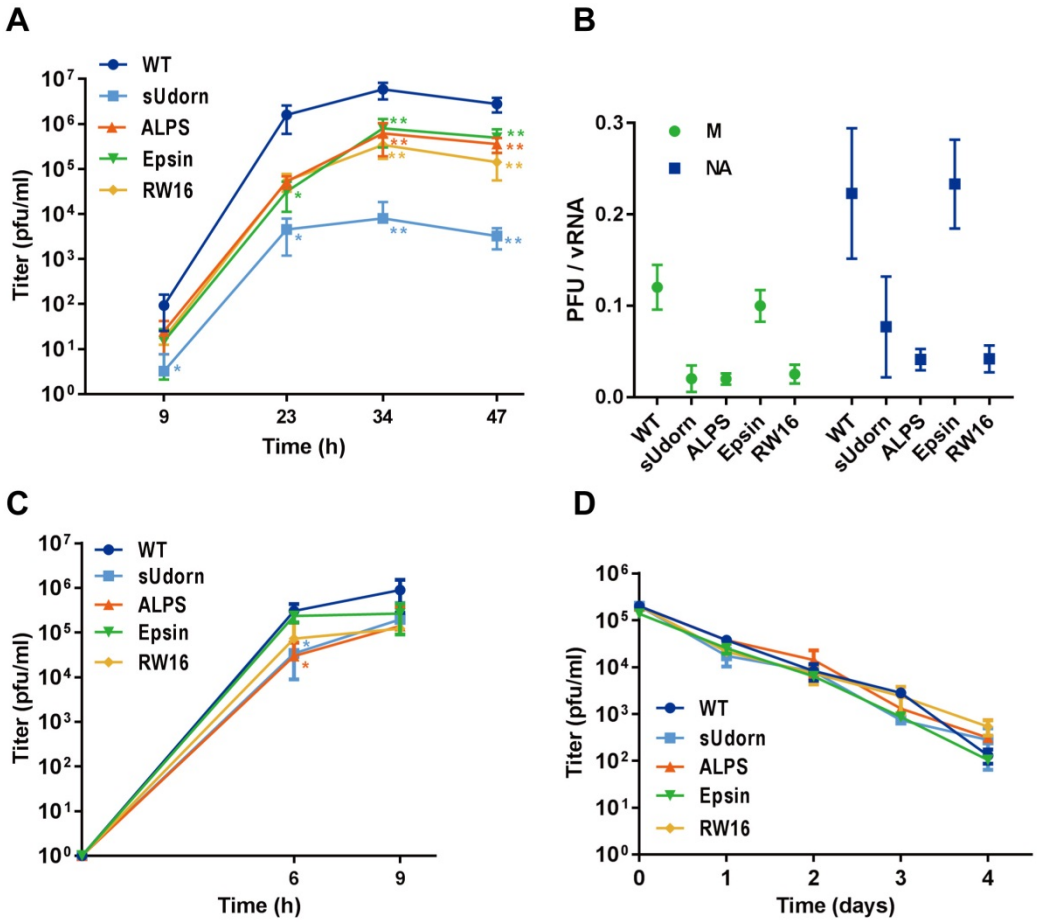

Fig. 5.11: Growth curves, specific infectivity and stability of viruses. (A) Multistep growth curves of WSN WT and mutants. MDCK II cells were infected with viruses at a low moi of 0.001. Culture supernatant was harvested at indicated time points after infection and the virus titers were determined by plaque assay. Results from three independent infection were shown as mean ± SD (standard deviation). Asterisk (*) indicates statistically significant differences between WT and mutants (* P<0.05; ** P<0.01) based on student's t-test. **(B)** Analysis of the ratio of infectious to total virus particles. Samples were collected at 34h post infection from growth curve in (A). Viral RNA from the same amount of culture supernatant was extracted and the copy number of segment M and segment NA were measured by RT-qPCR. The ratio of PFU titer to vRNA copy number from three individual infection were shown as mean ± SD. **(C)** One-step growth curve of WSN WT and mutants. MDCK II cells were infected with viruses at high moi of 1. Culture supernatant was harvested at indicated time points after infection and the virus titer was determined by plaque assay. Results from three independent infection were shown as mean ± SD. Asterisk (*) indicates statistically significant differences between WT and mutants ALPS or sUdorn (* P<0.05) based on student's t-test. **(D)** Stability of virus WT and mutants. $2x10^5$ pfu/ml viruses were put into 37°C incubator for 4 days. One aliquot of each virus was removed per day and the remaining infectivity was determined by plaque assay.

5.2.3 Membrane scission is not disrupted by replacement of AH in M2 CT.

Previous work by others suggested that the AH in the M2 CT is involved in membrane scission during virus budding, since virions with an unusual "beads on a string" morphology were released when the AH was mutated (71, 89). To investigate whether replacement with other amphipathic helices in M2 might also affect membrane scission, transmission electron microscope was applied to observe ultrathin sections of MDCK II cells harvested at 24-36h after infection with viruses at low moi. Nevertheless, none of the mutants showed "beads on

a string" morphology and the released virus particles were mainly spherical as WSN WT (Fig. 5.12), indicating the membrane scission function of M2 can be fulfilled when AH is replaced with other helices and the impaired growth of WSN mutants is not due to a defect in membrane scission.

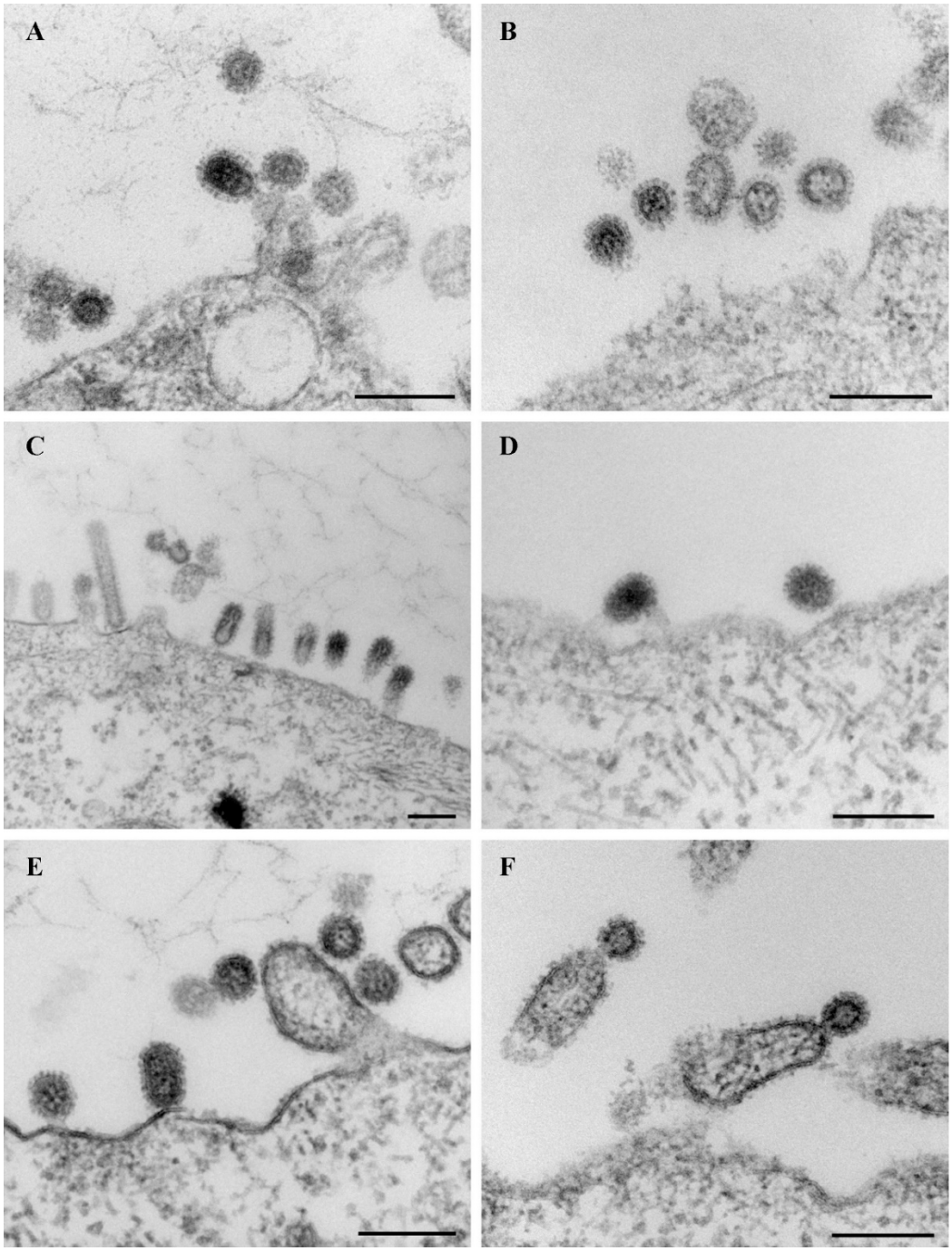

Fig. 5.12: Membrane scission is not disrupted by replacement of AH in M2 CT.

(A-F) Representative images of ultrathin sections of MDCK II cells infected with (A) WT, (B) sUdorn, (C+D) Epsin, (E) ALPS, and (F) RW16. Scale bar represents 200 nm.

5.2.4 Less M2 ALPS and M2 Epsin are expressed at the plasma membrane

The defect in growth of virus mutants might be due to a lower availability of M2 at the virus assembly and budding site. To analyze the intracellular distribution of wild-type and mutated M2 proteins, MDCK II cells infected with viruses were permeablized, stained with anti-M2

mAb 14C2 and then observed with immunofluorescence microscopy. M2 WT was seen at the plasma membrane and also in the cytosol with bright perinuclear (possibly Golgi) and weaker reticular staining (presumably ER) throughout the cell. Every M2 mutant was present at the cell surface, but their fluorescence intensities and distribution patterns within the cells were different from M2 WT (Fig. 5.13A). M2 Epsin showed a more evenly distributed intracellular pattern since cells are presented as blurry green, whereas M2 ALPS (M2 RW16 to a less extent) exhibited a very bright signal in a perinuclear compartment, suggesting a disrupted intracellular transport of M2 mutant proteins.

To analyze the amount of M2 mutant proteins at the cell surface and compare with M2 WT, MDCK II cells were infected with virus WT and mutants and then analyzed by flow cytometry. Infected cells were divided into two parts, one part was permeablized to measure the total expression of M2, the other left untreated for surface expression. Both parts were incubated with anti-M2 mAb 14C2 which recognizes an epitope in the extracellular part of M2 (72) and stained with fluorescent secondary antibody. The mean fluorescence intensity from 10^5 cells was calculated and normalized to the surface expression of M2 WT (=100%) (Fig. 13B). The results from three individual infections showed that less M2 ALPS (44%) and M2 Epsin (67%) are present at the plasma membrane, which might be partially due to decreased overall expression. The surface expression of M2 RW16 is also slightly lower than WT, while M2 sUdorn showed a slightly higher surface expression. But due to large variations in each experiment, the M2 amount of these two mutants are not statistically significantly different from WT.

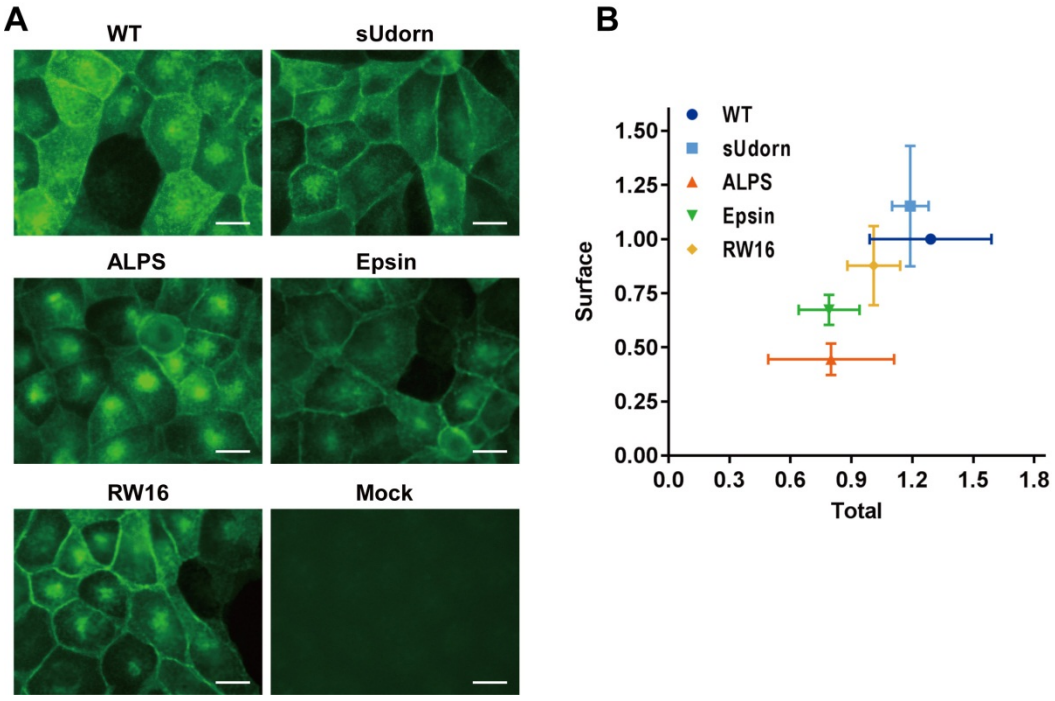

Fig. 5.13: The surface and total expression of M2 WT and mutants. (A) Fluorescence microscope images of MDCK II cells infected with WSN WT and mutants. MDCK II cells, infected with viruses at an moi of 1, were fixed and permeablized at 4.5h post infection, then stained with anti-M2 mAb 14C2 and fluorophore-coupled secondary antibody Alexa Fluor 488. Scale bar: 20 µm. **(B)** Relative expression of M2 in infected MDCK II cells by flow cytometry. MDCK II cells, infected with viruses at an moi of 1, were fixed at 4.5h post infection. They were either directly stained with anti-M2 mAb (surface expression) or permeablized before staining (total expression). At least 10^5 cells were analyzed by flow cytometry and their mean fluorescence intensity was normalized to surface expression of WSN WT (=1). Results from three independent infections are shown as mean ± SD.

5.2.5 Less M2 is incorporated into virus mutants

Since M2 mutants, especially ALPS and Epsin, showed reduction in surface expression, M2 incorporation into mutant virions might also be affected. Therefore, I analyzed the M2 amount in purified virus wild type and mutants by western blot. Two bands of M2 WT were detected under reducing condition, the major one with a mass of 15 kDa and the minor 17 kDa, as previously reported (117). However, not every M2 mutant ran to the position corresponded to the predicted molecular weight, especially M2 ALPS who ran faster than M2 WT even though it has more amino acids (Fig. 5.14A, right).

For quantification of the M2 amount, the ratio of M2 to M1 (analyzed in parallel with M2 since they were blotted to one membrane) was calculated based on the quantification of their band intensity and then normalized to WT. The results from three different virus preparations (Fig. 5.14B) revealed a significant reduction of the M2 amount in virus mutants ALPS, Epsin and RW16, only ~25% of WT. In contrast, virus sUdorn had similar relative amount of M2 as virus WT.

Nevertheless, each M2 mutant folds into disulfide-linked dimers and tetramers as M2 WT as shown by non-reducing SDS-PAGE (Fig. 5.14C), therefore the tetramer-requiring proton channel activity might not be disturbed for M2 mutants.

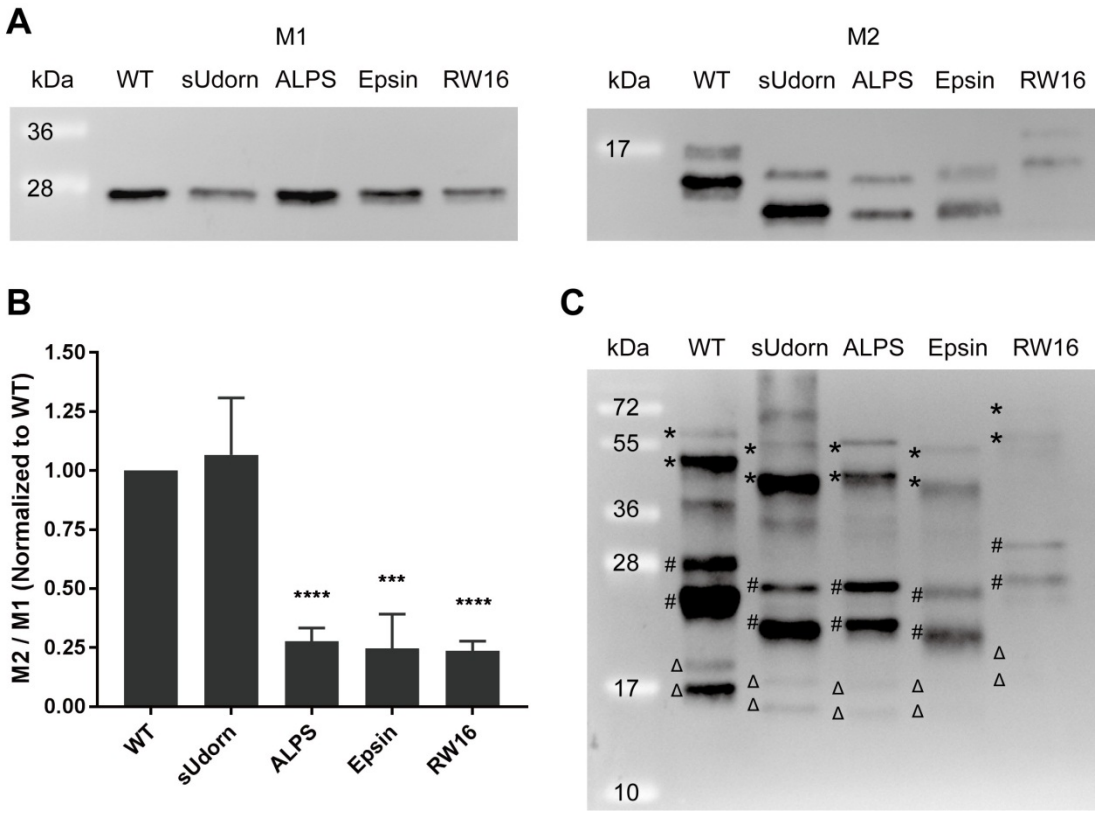

Fig. 5.14: M2 incorporation into virus particles. (A) Western blot of purified WSN WT and mutants under reducing condition. Viruses were purified through 20-60% sucrose gradient, subjected to reducing SDS-PAGE and detected by monoclonal antibody against M1 (left) and M2 (right) respectively, followed by HRP-coupled secondary antibody. The molecular mass marker (kDa) are shown on the left. **(B)** Relative quantification of ratio of M2 to M1. The denstiy of M1 and M2 bands were measured by Image J. The ratio of M2 to M1 was calculated and normalized to WT (=1). Results from three virus preparations are shown as mean ± SD. Asterisk (*) indicates statistically significant differences between WT and mutants (*** P<0.001; **** P<0.0001) based on student's t-test. **(C)** Western blot of purified WSN WT and mutants under non-reducing condition. Anti-M2 mAb was used to analyze its oligomerization. Δ: monomer; #: dimer; *: tetramer.

5.2.6 Viral protein composition is affected by replacement of AH in M2 CT

A M1 binding site is found in the cytoplasmic tail of M2, through which M1 is recruited to the virus assembly and budding site at the plasma membrane (90, 92, 118). To examine whether decreased amount of M1 is incorporated into virus mutants, I analyzed the viral protein composition of purified WSN WT and mutants with two to three virus preparation by SDS-PAGE followed by coomassie staining (Fig. 5.15A). The band intensity of three major viral proteins HA, NP and M1 were measured and their relative amount (with the three viral proteins added up to 100%) were compared (Fig. 5.15B). Obviously, viral protein composition was changed in virus mutants and they incorporated less M1 than WT, especially sUdorn who showed a severe reduction, from 27% (WT) to 14%. And the decreased amount of M1 in virus sUdorn was compensated by relatively increased percentage of NP, while in virus Epsin and RW16 compensated by HA. However one should notice that influenza viruses assembly is a process with low fidelity, large variation in viral size and protein composition (within 100 fold range) exists in virus samples produced even from single virus infection (8).

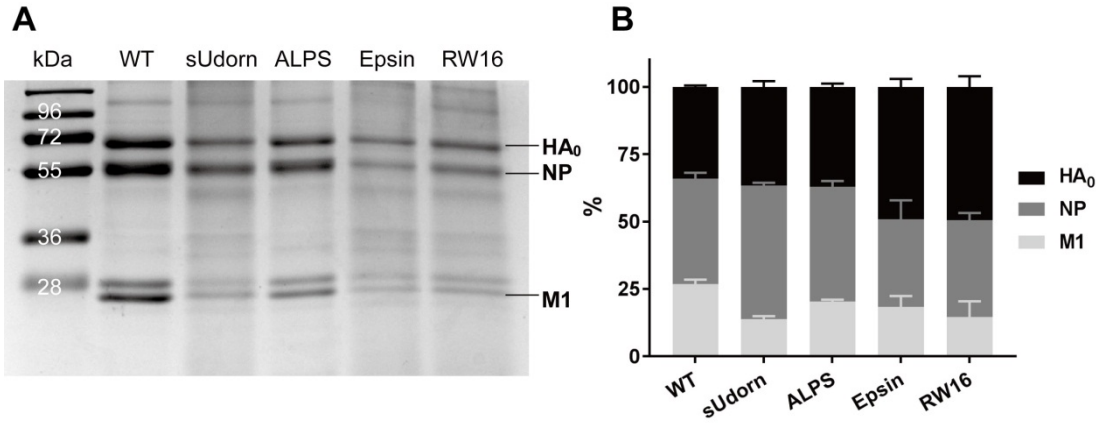

Fig. 5.15: Protein composition of virus WT and mutants. (A) Viral protein composition of WSN WT and mutants. Viruses were purified through 20-60% sucrose gradient, subjected to non-reducing SDS-PAGE and stained with coomassie. The positions of HA0, NP and M1 protein are indicated and the molecular mass marker (kDa) are shown on the left. **(B)** Determination of the relative protein composition. The density of HA0, NP and M1 bands was determined by Image J and the relative percentage of each protein was calculated with three proteins added up to 100%. Results from 2 to 3 different virus preparations are shown as mean ± SD.

6 Discussion

6.1 The role of the cholesterol consensus motif in HA

6.1.1 HA interacts with cholesterol

It has been proposed that HA interacts with cholesterol, which is based on several phenomena related to both HA and cholesterol. HA inserts into cholesterol- and sphingolipids-enriched nanodomains, demonstrated by direct isolation of HA from detergent resistant membranes (86) or by FRET measurement of HA-Cer and a raft-marker (75). HA is also accumulated in the plasma membrane to form clusters, while cholesterol depletion converts HA clusters to a random distribution and decreases HA lateral mobility and fusion activity (59, 62). However, so far no direct evidence for an interaction of HA with cholesterol has been reported.

Our studies here show for the first time that HA binds to cholesterol. This was proven by using a cholesterol analogue (photocholesterol) to label HA in CHO cells. Substitution of the whole cholesterol consensus motif Y-K-L-W to alanines reduced ~40% of photocholesterol incorporation into HA-expressing cells (Fig. 5.2B+C). In the cells, HA is embedded in the biological lipid environment so that this cholesterol analogue must compete with other lipids for binding to HA. However, direct labeling of the HA protein purified by immunoprecipitation from cell lysates also showed a similar, even larger reduction in cholesterol interaction with HA mutant YKLW4A (Fig. 5.2D+E), excluding the possibility that the reduced association observed in vivo is due to decreased integration of HA into cholesterol-rich nanodomains.

In contrast, mutations of two consecutive residues of CCM, both YK and LW, showed no effect on this interaction, indicating that these two groups act synergistically for cholesterol binding. However, it should be noted that crosslinking is mainly a qualitative technique to demonstrate binding of cholesterol to a protein, not suitable to precisely determine the affinity of this interaction. To determine the specific amino acids of HA binding to cholesterol requires more sophisticated methods, such as crystallography or NMR (97).

Contradictory to the well-known sphingolipids- and cholesterol-enriched raft domains, one recent study using high-resolution secondary ion mass spectrometry (SIMS) failed to show cholesterol-rich domains. In addition, HA clusters did not always colocalize with cholesterol (119). However, this method only analyzes the thin surface of cells and the analysis depth is less than the thickness of the plasma membrane (< 5nm) (120), Thus, it might not efficiently measure all the cholesterol in the membrane, especially considering that cholesterol inserts deep into the lipid monolayer due to its small hydroxyl headgroup. Furthermore, the HA protein in this study is an H2 subtype HA which belongs to the phylogenetic group 1 HAs that contain no Y-K-L-W motif (80). Despite the fact that clustering of HA proteins at the plasma membrane have been reported for both group 1 (e.g. subtype H2 (121)) and 2 (e.g. subtype H3 and H7 (58, 75)) HAs, their mechanism of clustering could be different.

6.1.2 CCM is found in only phylogenetic group 2 not group 1 HA subtypes

The CCM motif Y-K-L-W is found only in phylogenetic group 2 HA subtypes and within each subtype these four amino acids are even completely conserved (99%), which highlights their potential importance in maintaining HA's function (80). Indeed, when all the four amino acids were exchanged with alanine, no virus could be rescued. Viruses with double mutations in the CCM showed defects in virus replication (Fig. 5.3). They grew to lower titers than WT and they were less fit when growing in a competitive environment with virus WT, i. e. they were rapidly outgrown by WT (Fig. 5.3C). Therefore, the CCM is essential for virus replication.

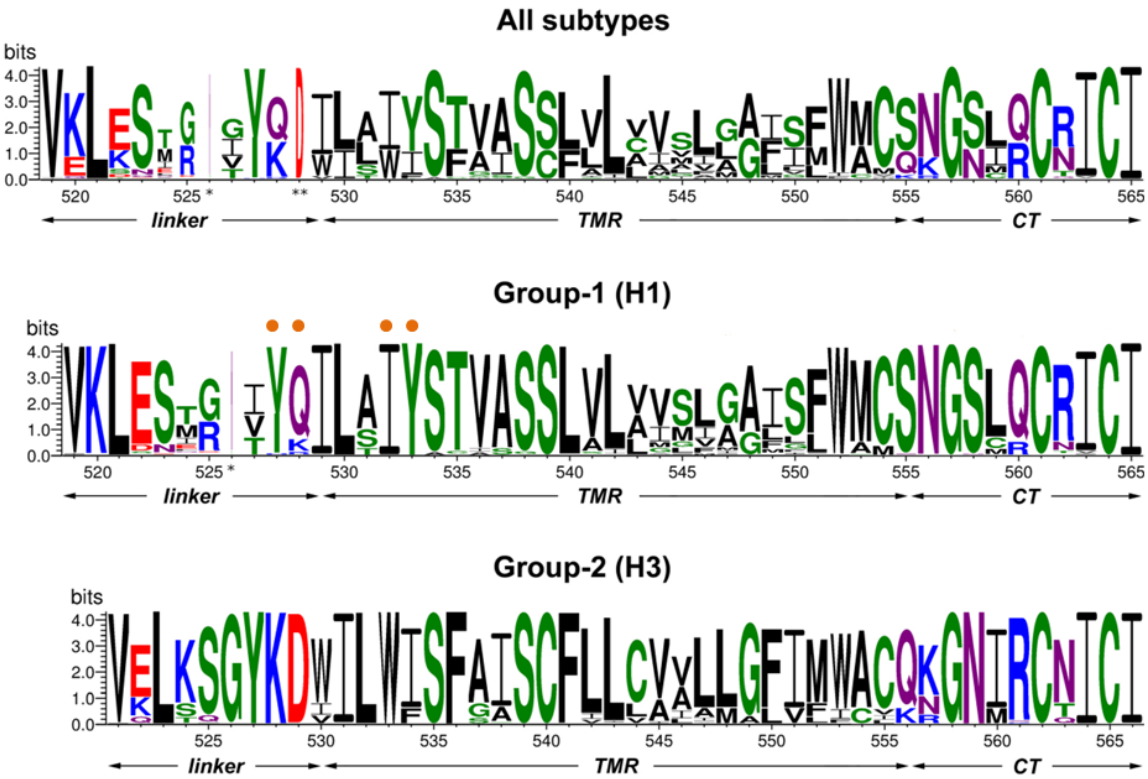

Fig. 6.1: Conservation analysis of C-terminal part of HA. The overall height of the stack represents the sequence conservation, while the height of every letter indicates the relative frequency of one amino acid at that position. The numeration of amino acids corresponds to the HA from A/WSN/33 (H1N1) for group 1 (middle panel) and from A/Udorn/72(H3N2) for group 2 (lower panel). The relative regions of linker, transmembrane region (TMR), cytoplasmic tail (CT) are indicated. The amino acids composing the potential CCM in group 1 HAs are indicated with orange circle above each letter. This figure is adapted from (122) with permission.

However, the CCM motif is not found in group 1 HA subtypes, see Fig. 6.1 above. But they possess another conserved consensus sequence Y_{12}-K/Q_{13}-I_{17}-Y_{18} (number referring to Fig. 5.1A, indicated in Fig. 6.1) , which also meets the requirement of a cholesterol binding motif, containing basic, hydrophobic and aromatic residue, a common amino acid composition pattern in all cholesterol binding motifs such as CARC, CRAC and GXXXG motif (36, 40, 43). Indeed, one study reported that simultaneously substituting alanine for Ile17 and Tyr18 in this consensus sequence greatly retarded intracellular transport of a H2 subtype HA (a group 1 HA) (83). A recent NMR structure of H1 subtype HA also highlight the importance of Tyr18 in maintaining the structure of TMD of HA (54). However, this residue Tyr is not conserved in group2 HAs, indicating that these two phylogenetic HA groups might differ in their structure of this region. Whether group1 HAs also bind to cholesterol (or to another lipid) requires further investigations.

6.1.3 The role of the CCM for (apical) membrane transport of HA

Polarized epithelial cells have two distinct surfaces, an apical and a basolateral membrane. Proteins and lipids would depend on an intricate sorting machinery to be delivered to the right membrane. It was proposed that lipid-clusters through oligomerization of raft components, such as cholesterol, could be used to generate intracellular transport vesicles at membranes of the trans Golgi-network to deliver cargo exclusively to the apical membrane (123). However, I did not observe an effect on apical transport of HA and apical virus budding when the CCM motif was mutated (Fig. 5.4B+C). HA mutants were all exclusively

transported to the apical membrane rather than to the basolateral membrane, no matter whether the cells were infected with viruses or transfected with protein. Moreover, the mutant viruses also budded from apical membrane.

Others have already shown that the apical targeting signal and raft association signal for HA are both in the transmembrane domain, but they are not strictly related. Mutations in the TMD severely inhibiting HA insertion into DRMs resulted in no obvious effect on its apical sorting and vice versa (81-83). Contradictory results of HA membrane sorting in polarized cells have been observed when cholesterol was depleted from cellular membrane by MβCD (83, 124). Mutations in the CCM retarded HA transport to the cell surface and reduced its association with rafts (80).

6.1.4 The role of the CCM for virus assembly

Influenza viral proteins assemble at the apical membrane, which is as generally supposed initiated by clustering of HA in the raft domains. However, 10% (LW2A) to 20% (YK2A) reduction in cholesterol content were observed in CCM mutant viruses (Fig. 5.6A+B). Presuming that a total of 300000 lipid molecules exist in the membrane of a spherical IAV particle (based on the calculation of HIV particles which have the same size and accordingly the lipid surface area (125)) and around 50% (=150000) of the lipids are cholesterol (29), a 10-20% reduction is thus equivalent to 15000-30000 cholesterol molecules. An IAV particle contains an average number of 300-500 trimeric HA spikes (as measured by Cryo-EM (126, 127)) and hence there are at most 1500 cholesterol recognition sites available. It is thus obvious that the 10-20% decrease in cholesterol content could not be explained by a stoichiometric (1:1) binding of cholesterol. Therefore, a cooperative effect must be involved instead, which means the mutations in the CCM lowers the cholesterol content through reducing 10-20 cholesterol molecules insertion per trimeric HA spike. One cholesterol molecule directly interacts with the CCM of HA and then recruits (probably through lipid-lipid interactions) other cholesterol molecules into virions. Evidence to support this assumption was found in the crystal structures of β-adrenergic receptors and other G-protein-coupled receptors (GPCR), which shows binding of two (or more) cholesterol molecules in the TMD, although only one CCM motif is present (42, 45).

10-20 cholesterol molecules might be sufficient to enclose the outer part of the TMD of one HA spike when assuming that the diameter of an α-helix and cholesterol is 10Å (1nm) and 5Å, respectively. Such small but condensed lipid shells have been postulated to target transmembrane proteins to raft-like lipid domains or to induce the formation of such domains (128, 129). Indeed, HA mutants YK2A and LW2A exhibited reduced association with the raft-marker Myr-Pal–YFP in transfected cells by FRET (80). And raft-dependent oligomerization at the plasma membrane of a H3 subtype HA was prevented by mutations of the first three residues of TMD (58). This mistargeting of HA would probably cause virus budding through the (cholesterol-depleted) bulk phase of the membrane. Indeed, the 10-20% decrease of cholesterol content in CCM mutant viruses (Fig. 5.6 A+B) generates a total cholesterol concentration of 45%, which is in perfect correspondence with the measured concentration of cholesterol in the apical membrane of polarized MDCK cells (28).

Exchanges in the CCM not only influence the lipids in the viral membrane, but also decrease incorporation of HA protein (relative to M1 or NP) into virions (Fig. 5.5). This was observed in virions released from MDCK II cells as well as those (but less distinct) grown in embryonated chicken eggs and the virus mutant LW2A showed the most obvious reduction. A similar phenomenon has been reported in a H3 virus (also belonging to group 2 HAs) when three amino acids (WIL) at the beginning of the TMD of HA were changed to alanine (58).

Among the CCM mutant viruses, LW2A showed the strongest defect in virus replication and HA's incorporation into virions. However, the incorporation of cholesterol was decreased to a larger extent in YK2A than in LW2A. Nevertheless, one should note that the data from virus composition analysis revealed, that considerable variation exists in individual experiment, which is at least partially because of IAVs' pleomorphic nature. A very recent study using

fluorescence microscopy showed that even progeny virions produced from virus infection of a single cell exhibited large variation in virus size and protein composition, with HA, NA and M2 content in individual virions varying within a ~100 fold range (8). This low-fidelity assembly process makes it very difficult to precisely measure the effect of mutations in the CCM on the morphology of IAVs particles when even a wild type exhibits such a large variation between individual particles.

One open question is whether there is a functional relation between these two raft targeting signals in HA, the CCM motif in the linker and at the beginning of TMD and S-acylation at conserved cysteine in the cytoplasmic tail. Deleting either signal would sufficiently impair HA association with raft (75). Both signals are indispensable for virus replication since no virus could be rescued with completely removal of either signal (this study and (55, 79, 130). Viruses bearing partial deletion of signals replicated less efficiently and showed defects in membrane fusion and virus budding. Despite causing those similar consequences, mutating these two signals do however exhibit different effects. Substitution of the conserved cysteine residues would not slow down the intracellular transport of HA (79) nor affect the lipid composition (cholesterol amount) of the viral membrane, at least in the case of virus-like particles (131). Therefore, whether there is any mutual interplay between these two raft-targeting signals to define the virus assembly and budding site is still unclear.

However, it is highly unlikely that HA association with cholesterol happens only at the plasma membrane given that HA mutants showed significantly delayed transport through Golgi, a compartment of secretory pathway along which cholesterol concentration increases from ~5% (ER) to ~40% (plasma membrane)(29).

6.1.5 The role of the CCM for HA´s membrane fusion activity

I demonstrate in this study that changes in the CCM of HA affect not only the kinetics but also the extent of HA's fusion activity with three different experiments performed with either virus particles or HA-expressing cells (Fig. 5.7-5.9). A similar phenomenon has been observed in a H3 subtype HA when the first three amino acids of the TMD were changed (58). One possible reason for the decreased fusion activity could be the reduced amount of HA at the plasma membrane of transfected cells or in the viral membrane. However, by adjusting both virus WT and mutants to the same HA titer, the effect of the smaller amount of HA in virus mutants should be at least partly compensated. Therefore, the decreased fusion activity is rather a direct consequence from changes in the CCM of HA.

The R18 fluorescence dequenching assay with the virus mutants YK2A and LW2A plus the quantification of fusion event in cells transfected with HA YKLW4A demonstrated that the fusion stage of lipid mixing is disturbed by mutations in the CCM (Fig. 5.7-5.9). In the YKLW4A-expressing cells a peculiar phenomenon was observed, i.e. the erythrocytes remain only bound to but not fused with the cells after acidic pH treatment (Fig. 5.9). In theory, there are several reasons for this. One would be that a part of HA YKLW4A molecules are not activated after low pH treatment so that they keep the structural conformation at neutral pH, which cannot perform membrane fusion. Another one might be that a certain number of HA YKLW4A molecules undergo an incorrect conformational change, i. e. the fusion peptide could not insert into the membrane of host cells or the HA2 stem could not properly bend to put the two membrane in close proximity to allow lipid mixing. In this case the phenomenon of bound but not fused erythrocytes to HA-expressing cells might correspond to those early stages of HA-mediated membrane fusion recently revealed by cryo-EM, such as HA-bridging contacts, membrane dimpling and/or tightly docked membrane-membrane contacts (48, 49). In any case, this phenomenon suggests that a membrane fusion step before lipid mixing is disturbed in HA YKLW4A.

The decreased fusion activity of HA could be also the result of a general effect of alanine substitutions in the CCM on the membrane of the virus. Progeny virions incorporate less cholesterol, which might profoundly influence the biophysical properties of viral membrane beneficial to fusion process. In fact, the leucine residue of the CCM has been shown to be

very important for the TMD of a H3 subtype HA to induce the formation of highly ordered membrane domains (132). This, together with insertion of the fusion peptide into host cell membrane, causes membrane dehydration, as recently proposed. This removes repulsive forces between the two opposite membranes and hence promotes the initialization of membrane fusion (133). Moreover, when I supplemented the mutant virions with exogenous cholesterol, they showed increased hemolysis activity (Fig. 5.7D). However, their hemolysis value was still below that of original virus WT without extra cholesterol despite their similar cholesterol content (Fig. 5.7C). One should also notice that the virus mutant YK2A contained the lowest cholesterol amount in its membrane (Fig. 5.6B), but LW2A showed the most severe defect in virus replication and hemolysis activity (Fig. 5.3 +5.7). Therefore, a disturbed phase separation (raft-formation) in the membrane and/or membrane ordering might result in only minor effects on the fusion activity of HA CCM mutants.

On the contrary, I would prefer a model proposed recently, which highlights the importance of the local interaction between cholesterol and the TMD of HA for membrane fusion (134). One might envision that cholesterol is recruited from the cytoplasmic leaflet to the extracellular side of the viral membrane through an interaction with CCM of HA at the fusion site, especially prior to hemifusion. The unique shape of cholesterol (small headgroup while large hydrophobic part) is beneficial to the formation of a highly curved membrane intermediates. However, this happens only if cholesterol is localized in the outer leaflet not the inner leaflet of the viral membrane (135, 136) (Fig. 6.2). On the other hand, cholesterol association with the amino acids in the CCM might disturb the flexibility of HA's linker region, which would then affect the conformational change of HA at acidic pH required for membrane fusion as recently proposed (54).

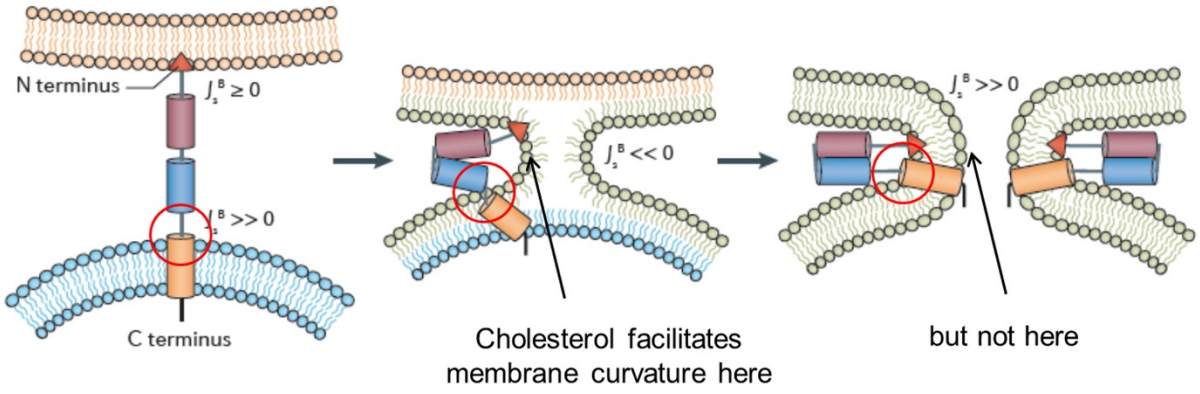

Fig. 6.2: The HA-mediated fusion process between viral and cellular membranes. The CCM region in HA is marked with a red circle. The potential position of cholesterol is indicated with an arrow. This figure is adapted from (137) with permission.

In summary, mutations in the cholesterol consensus motif (CCM) of a group 2 HA affect various functionalities of this protein, such as its transport along the secretory pathway, its insertion into rafts domains of the plasma membrane, incorporation of HA and cholesterol into progeny virions, and virus entry through membrane fusion, especially the stage of lipid mixing and probably an earlier step.

6.2 The amphipathic helix in the cytoplasmic tail of M2

6.2.1 An amphipathic helix in the cytoplasmic tail of M2 is essential for virus replication

The study here shows that the amphipathic helix (AH) in the cytoplasmic tail of M2 is essential for virus replication of the spherical WSN strain. I demonstrated that deletion of the AH or exchanging it with a scrambled version, which has the same composition of amino

acids but a lower hydrophobic moment and thus is not amphiphilic abolished the possibility to rescue viruses. In contrast, virus can tolerate the AH replacement with three different types of amphipathic helices, Epsin, ALPS and RW16, showing only minor defect in virus replication with around 1-2 logs reduction in virus titers compared to the original wild-type virus (Fig. 5. 11). Viruses could be successfully generated even with the scrambled version of the AH peptide from Udorn strain. The replication of this virus mutant (sUdorn) is severely impaired, exhibiting 3 logs reduction in virus titer. However, this sUdorn AH peptide has only a slightly lower hydrophobic moment and a higher hydrophobicity compared to the M2 AH WT (Fig. 5.10), indicating that it might also effectively interact with lipids. Therefore, the membrane proximal part of cytoplasmic tail in M2 could be replaced with other peptides as long as they could form an amphipathic helix.

6.2.2 Amphipathic helix replacement affects virus assembly but probably not membrane scission

Other studies demonstrated that virions with an unique “beads on a string” morphology could be observed when five hydrophobic amino acids in the helix region of M2 from the WSN or Udorn strain were substituted with alanine (89, 98) or generally when viruses with defects in assembly and budding were analyzed (87). However, for none of our mutant viruses, I observed such (or any other) altered morphology when ultrathin sections of MDCK II cells infected with virus mutants were analyzed by transmission electronic microscopy (Fig. 5.12). Therefore, I speculate that the mutant M2 protein in this study could also effectively perform its function in virus budding and membrane scission, i. e. inducing membrane curvature, whereas the decreased titers of mutant viruses might mainly result from other defects in this protein.

In fact, I did observe several different defects in M2 when the AH was replaced, although there are variations among these M2 mutants. Two of them, ALPS and Epsin, showed a reduction in their expression at the plasma membrane of infected cells, which is due to a decreased total expression in the cells as well as its retarded intracellular transport through the ER or Golgi (Fig. 5.13). Recent studies reported that M2 transport to the cell surface along the secretory pathway is modulated by host cellular proteins, such as the putative ubiquitin ligase UBR4, transport protein particle complex 6A (TRAPPC6A and its isoform TRAPPC6AΔ) and Rab11 (138, 139). Therefore, it is likely that M2 mutants might not be able to interact with one of these or other cellular proteins to be efficiently transported to the cell surface, which would then partly account for the decreased virus titers shown in the growth curves. Consistent with this assumption, a recent study also reported that limiting M2 protein in the ER or targeting it wrongly to the basolateral membrane to reduce its apical expression greatly impaired virus replication (140).

Both M2 mutant proteins ALPS and Epsin are also less efficiently incorporated into progeny virions since their amount in purified viruses (relative to M1 protein) is greatly reduced to ~25% of WT (Fig. 5.14B). Virus mutant RW16 also showed the same reduction in M2 incorporation although no (statistically significant) defect in plasma membrane expression was observed. It is possible that M2 RW16, though present at the plasma membrane, is not enriched at the viral assembly and budding site, and therefore not efficiently incorporated into virions. The signals for M2 co-clustering with other viral proteins, such as HA are amino acids in the hydrophobic face of the amphipathic helix, such as Ile, Phe and Tyr (71). The helix RW16 comprises only charged residue Arg and apolar residue Trp, which might make it less efficiently to be inserted into the virus assembly site.

Whether M2 mutant protein ALPS and Epsin are clustered at the virus budding site could not be answered based on our results. However, the α0-helix of Epsin I studied here binds with the membrane lipid PtdIns(4,5)P2 (105), while the latter is found also co-localized with HA (141). Thus, the potential affinity of both HA and M2 Epsin to this charged lipid located only at the cytoplasmic leaflet of the membrane might promote their co-localization.

No explanation has been achieved so far for the abundant expression of M2 at the plasma

membrane of infected cells, yet M2 is, compared to HA protein, largely excluded from released virions (72). One possible reason for its high expression level would be to facilitate M1 transport to the plasma membrane and further to the assembly site. M1 is the most abundant protein of influenza virus, but it has no intrinsic membrane targeting signal (118). M2 contains a M1 binding site at its cytoplasmic tail and I observed in this study that in all purified mutant virus particles M1 content was decreased, no matter whether the M2 amount in those virions was reduced or not (Fig. 5.15). Therefore it is likely that changes in the amphipathic helix of M2 disrupt to some extent its binding to M1 and the following translocation to the virus assembly site at the plasma membrane.

Additionally, replacement of this helix also decrease the specific infectivity for all mutant viruses (except for Epsin); the ratio of infectious to total virus particles was reduced by around 50% (Fig. 5.11B). This indicates that the normal virus assembly process is disturbed to a certain degree, thus comparatively more non-infectious progeny mutant virions are released.

6.2.3 The possible effect of AH replacement on virus entry

M2 transports protons from the endosome into the virus interior to mediate disassociation between the matrix protein and vRNPs and this process should happen before the HA-mediated membrane fusion triggered by acidic pH in the endosome. Otherwise, protons could diffuse from endosome into virions through the fusion pore, which should be faster than M2-mediated proton influx. Despite that M2 is highly expressed in infected cells, one wild-type virus particle incorporates only 14-68 M2 monomers, that is 3.5-17 M2 ion channels per virion (72). In this case, there might be 1-4 M2 proton channels in mutant viruses ALPS, Epsin and RW16, since their M2 content decreased severely to ~25% relative to that of WT (Fig. 5.14B). Consequently, a proportion of mutant progeny viruses might not contain even a single M2 proton channel, so that they are not infectious. Thus, that the mutant viruses grow to lower titer might be due to a defect in virus entry, which might be due to no or insufficient number of proton channel to acidify the virus interior ahead of low-pH triggered HA-mediated membrane fusion, despite that the proton channel activity of M2 mutant proteins is almost fully preserved.

To sum this part up, I obtained no evidence that membrane scission of IAVs is disturbed if the amphipathic helix in the cytoplasmic tail of M2 is replaced by other helices with similar biophysical properties. Nevertheless, I observed several different deficiencies in M2 mutant proteins, such as defects in transport to the cell surface, decreased incorporation into progeny virions, disrupted assembly process, which might account for the marginally reduced virus titers. On the other hand, I could not rescue viruses if this amphipathic helix region was deleted or replaced by a scrambled version, which has a very low hydrophobic moment. This accordingly supports the concept that this amphipathic helix of M2 inserts into the edge of virus budding site, induces membrane curvature and mediates membrane scission.

7 Outlook

This study showed that mutating the four amino acids of the CCM motif significantly reduced click-labeling of HA with photocholesterol in HA-transfecting cells and with the immunoprecipitated protein, but this interaction is not completely abolished. It might be due to the abundant presence of cholesterol in the plasma membrane (45%), i. e. there is always plentiful cholesterol in close proximity to HA even in the absence of a binding site.

Alternatively, other amino acids might be also involved in binding to cholesterol. Although no structural data of the transmembrane region of a group 2 HAs is available, the latter seems possible if I envision this interaction based on structural data of cholesterol binding sites of other proteins.

The thickness of a lipid bilayer is about 4-5nm and thus a monolayer is around 2-2.5nm thick. Cholesterol is oriented parallel to phospholipids, but inserts slightly deeper into the monolayer due to its small hydroxyl group. Cholesterol has a length of 17Å (1.7nm), the steroid rings are ~9Å (Fig. 7.1A).

Along the axis of a α-helix each amino acid is located 1.5Å above the previous residue with a rotation of 100°. This means that the helix has 3.6 residues per turn and the distance between two residues at equivalent position is 5.4Å (Fig. 7.1C). Thus, amino acids, which bind to cholesterol through hydrophobic interaction with the sterol ring and/or apolar tail should at least cover 2 helical turns (see Ile and Trp in Fig. 7.1A) and should be located inside the lipid monolayer. The basic residue forming a hydrogen bond with the hydroxyl head of cholesterol should be located at the membrane interface or slightly inside the membrane but facing upwards (e.g. the Arg of the CCM in human β2-Adrenergic receptor, Fig. 7.1A).

Therefore, I want to propose an alternative model of cholesterol binding to HA, in which an aromatic residue (Phenylalanine, Phe, F) is added to the original CCM. This model is similar to the old version, the basic residue arginine (K) interacts with the headgroup of cholesterol (both are red in Fig. 7.1C), while the aromatic residue Tyrosine (Y) interacts with the sterol ring A (the first ring). The other two hydrophobic amino acids Leucine (L) and Tryptophan (W) are just three or four amino acids below the membrane surface. Since these two residues L and W are located next to each other, both of them should interact with the sterol ring A and B of cholesterol but from two different helices (Fig. 7.1C, similar to the Tyr in Fig. 7.1A). In this case, the three apolar residues, L, W and Y of the old CCM which make the major contributions to interact with the hydrophobic part of cholesterol only cover its upper part. Therefore, another hydrophobic or aromatic residue down below the helix could also be involved. In fact, an highly conserved (~100%) aromatic amino acid (Phenylalanine, F) is two amino acids away from residue W (three residues away from L) and thus might perfectly fit for the distance (Fig. 7.1C).

Additionally, a study on the H3 subtype HA reported that substitution of the residues Phe and Ile of the TMD severely impaired HA insertion into DRMs (58). Therefore, it would be worthwhile to include residue F into the cholesterol binding motif of HA and make mutations to analyze the labeling with photochesterol. Such a mutant might even completely lose the ability to perform membrane fusion. However, a high resolution structures of a full-length group 2 HA (Cryo-EM, crystallography or NMR) is required to directly identify the amino acids that contact cholesterol.

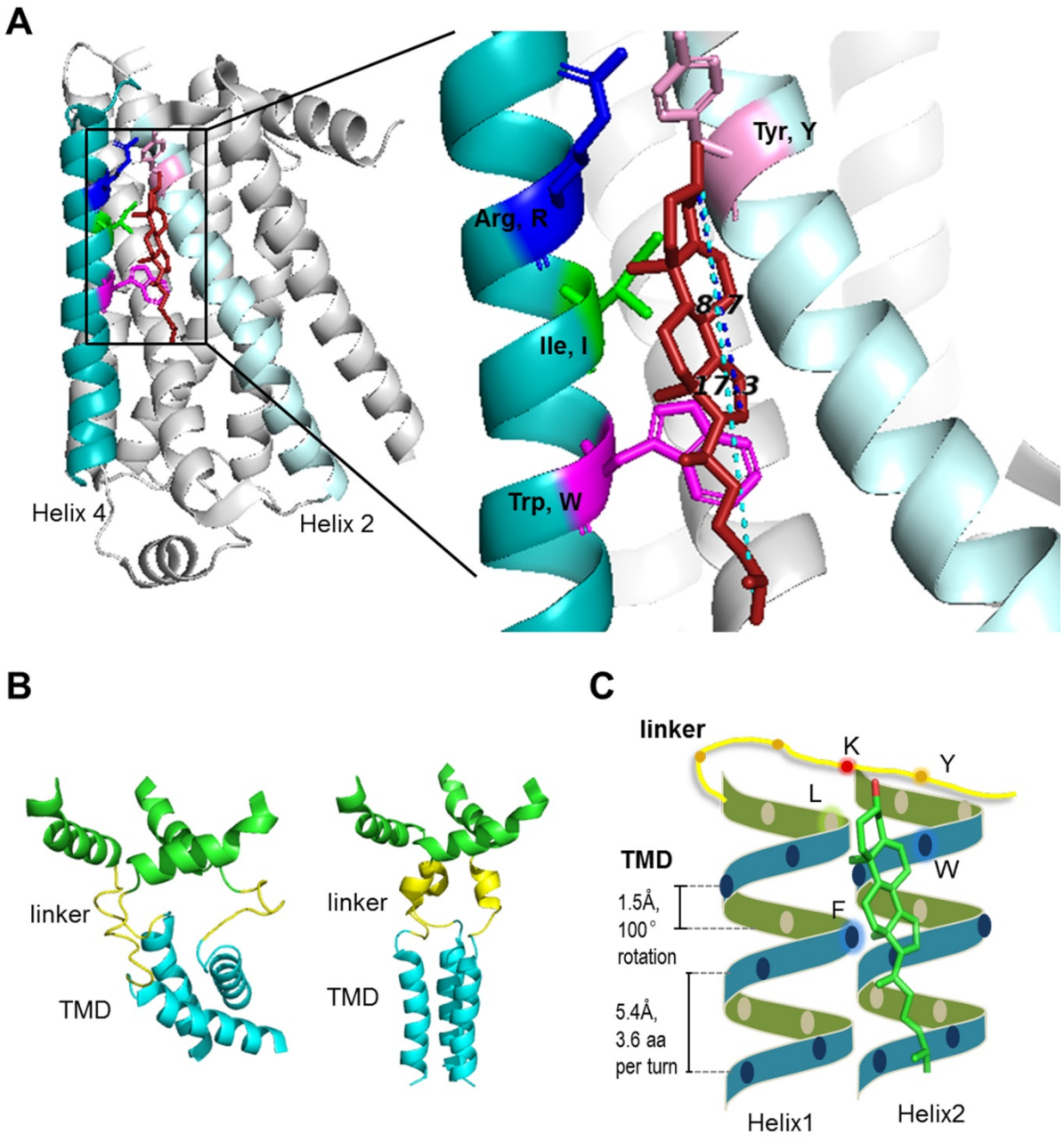

Fig. 7.1: Proposed CCM Y-K-L-W-F for binding to cholesterol. (A) Cholesterol binding to the human β2-Adrenergic receptor (45). On the left is the cholesterol binding to 7-transmembrane helices region of human β2-Adrenergic receptor. The indications are the same as Fig. 1.6C. The boxed region is magnified on the right. The length of the steroid ring and the whole cholesterol are shown and were measured by pymol. **(B)** Two structure of the linker region (yellow) and 19 aa of the TMD (cyan) of a H1 subtype HA (the same as in Fig. 1.7 D+E). **(C)** Proposed binding of cholesterol to CCM Y-K-L-W-F of group 2 HAs. The linker region is in yellow, the transmembrane domain in blue (front) and green (back). Each dot represents one amino acid. Cholesterol is in green and its hydroxyl group is red. The basic residue K is also red. The residues proposed to bind to cholesterol are in glow.

Zusammenfassung

Der Effekt des Cholesterin-Konsensus-Motivs in HA und der amphipathischen Helix in M2 auf die Replikation des Influenza-A-Virus

Influenza A Viren sind umhüllte Viren mit einer sphärischen oder filamentösen Morphologie. In ihrer Membran befinden sich zwei Glykoproteine, das Hämagglutinin (HA) und die Neuraminidase (NA) sowie der nicht glykosylierte Protonenkanal M2. Der Viruseintritt in Wirtszellen hängt von der Fusionsaktivität von HA und der Protonenleitfähigkeit von M2 ab, wohingegen die Virusassemblierung und -knospung durch Akkumulation von HA in mit Cholesterin und Sphingolipiden angereicherten Nanodomänen an der Plasmamembran ausgelöst wird. Darüber hinaus ist eine amphipathische Helix in der zytoplasmatischen Domäne von M2 an der Virusknospung beteiligt.

In dieser Studie wurde die Auswirkung von Mutationen in einem konservierten Cholesterinkonsensusmotiv (CCM) von HA auf die Virusassemblierung und die HA-Fusionsaktivität untersucht. HAs der phylogenetische Gruppe 2 enthalten das konservierte CCM Y-K-L-W in der Transmembranregion. Zuvor in unserer Gruppe durchgeführte Arbeiten zeigten, dass Mutationen in der CCM den intrazellulären Transport von HA verzögerten und dessen Assoziation mit cholesterinreichen Nanodomänen verringerten. Hier analysierte ich zunächst, ob Cholesterin mit dem CCM interagiert. Die Markierung von HA mit photoaktivierbarem Cholesterin war signifikant verringert, wenn die gesamte CCM durch Alanin ersetzt wurde, sowohl wenn immunpräzipitiertes HA als auch HA eingebettet in der zellulären Membran markiert wurde. Es konnten keine rekombinanten Viren generiert werden, wenn das gesamte CCM-Motiv ersetzt wurde (Mutante YKLW4A). Viren mit einem (LA) oder zwei Austauschen (YK2A und LW2A) in der CCM zeigten reduzierte Titer und einen Fitnessnachteil. Der apikale Transport von HA und das apikale Knospen von Viren in polarisierten Zellen wurden durch diese Mutationen nicht gestört. Reduzierte Mengen an HA und Cholesterin wurden jedoch in die Virusmembran eingebaut. Viren mit mutiertem HA zeigten eine verminderte Fusionsaktivität, wie durch Hämolyse- und Fluoreszenztests gezeigt wurde. Zell-Zell-Fusions-Assays unter Verwendung von doppelt markierten Erythrozyten und HA-exprimierenden Zellen zeigten, dass HA-YKLW4A mit Erythrozyten fusionieren kann, aber die Anzahl der Ereignisse war verringert. Auch nach der Ansäuerung blieben einige fusionierte Erythrozyten zellgebunden, ein Phänomen, das in HA-WT-exprimierenden Zellen nicht beobachtet wurde. Somit hat die Cholesterinbindung an HA Auswirkungen auf die Membranfusion, hauptsächlich auf den Schritt der Hemifusion und möglicherweise auf einen vorhergehenden Schritt.

Die amphipathische Helix in der zytoplasmatischen Domäne von M2 ist von entscheidender Bedeutung für die Virusassemblierung und -knospung. Da eine Vielzahl von amphipathischen Peptiden eine Membrankrümmung induzieren kann, habe ich untersucht, ob diese die M2-Helix ersetzen können. Es konnte kein Virus erzeugt werden, wenn die Helix von M2 deletiert wurde oder gegen ein Peptid ausgetauscht wurde, dass keine amphipathische Helix ausbilden kann. Im Gegensatz dazu konnten Viren hergestellt werden, wenn die M2-Helix durch Helices ersetzt wurden, von denen bekannt ist, dass sie eine Membrankrümmung induzieren. Diese Viren zeigten auch nur geringfügig verringerte Titer. Elektronenmikroskopische Aufnahmen von Schnitten infizierter Zellen zeigten keine nicht abgelösten mutierten Virionen mit einer "Bead-on-a-String" Morphologie, ein Kennzeichen für Viren mit fehlgeschlagener Membranspaltung. Die mutierten Viren zeigten andere Defekte in M2, wie eine reduzierte Oberflächenexpression und einen verringerten Einbau in Viruspartikel. Die Proteinzusammensetzung und die spezifische Infektiosität waren auch für die meisten mutierten Viruspartikel geändert. Ich schließe daraus, dass das Vorhandensein einer amphipathischen Helix in M2 für die Virusreplikation wesentlich ist, aber durch andere krümmungsinduzierende Helices aus zellulären Proteinen ersetzt werden kann.

Summary

Influenza A virus are enveloped viruses with a spherical or filamentous morphology. In their membrane are two glycoproteins, the hemagglutinin and the neuraminidase as well as the unglycosylated proton channel M2. Virus entry into host cells depends on the fusion activity of HA and the proton conductance activity of M2, whereas virus assembly and budding is supposed to be initiated by accumulation of HA in cholesterol- and sphingolipid-enriched nanodomains at the plasma membrane. Furthermore, the amphipathic helix in the cytoplasmic tail of M2 is engaged in virus budding and membrane scission to release progeny virions from the host membrane.

In this study the effect of mutations in a conserved cholesterol consensus motif (CCM) of HA on virus assembly and HA's fusion activity was investigated. Phylogenetic group 2 HAs contain the conserved CCM motif Y-K-L-W in the transmembrane region. Studies previously done in our group reported that mutations in the CCM retarded intracellular transport of HA and reduced its association with cholesterol-rich nanodomains. Here I firstly analyzed whether cholesterol interacts with the CCM. The click-labeling with photocholesterol was significantly reduced when the whole CCM was substituted by alanine, both using immunoprecipitated HA and when HA was embedded in cellular membranes. In the content of virus replication, no virus was rescued if the whole motif is replaced (mutant YKLW4A); single (LA) or double (YK2A and LW2A) mutated virus exhibited reduced titers and a comparative fitness disadvantage. The apical transport of HA and apical budding of viruses in polarized cells were not disturbed by these mutations. However, reduced amounts of HA and cholesterol were incorporated into the viral membrane. Mutant viruses showed decreased fusion activity as demonstrated by hemolysis and fluorescence dequenching assays. Cell-cell fusion assay using dual-labelled erythrocytes and HA-expressing cells revealed that HA-YKLW4A can fuse with erythrocytes, but the number of events was reduced. Even after acidification unfused erythrocytes remained cell-bound, a phenomenon not observed in HA-WT expressing cells. Thus, cholesterol binding to HA has effects on membrane fusion, mainly on lipid mixing and possibly a preceding step.

Being also crucial in virus assembly and budding, the amphipathic helix in the cytoplasmic tail of M2 was also investigated. Since a variety of amphipathic peptides mediate membrane deformation and induce their vesicularisation, I used reverse genetics to investigate whether they can substitute for M2's helix. No virus could be generated if M2's helix was deleted or exchanged to a peptide predicted not to form an amphipathic helix. In contrast, viruses could be rescued if the M2 helix was replaced by helices known to induce membrane curvature, but they showed only slightly decreased virus titers. Transmission EM of infected cells did not exhibit undetached mutant virions with a "bead-on-a-string" morphology, a hallmark of viruses with failed membrane scission. Nevertheless, individual mutant viruses exhibit other defects in M2, such as reduced surface expression and decreased incorporation into virions. The protein composition and specific infectivity was altered as well for most mutant virus particles. I conclude that the presence of an amphipathic helix in M2 is essential for virus replication, but it can be replaced by other curvature-inducing helices from cellular proteins.

References

1. **Webster RG, Bean WJ, Gorman OT, Chambers TM, Kawaoka Y.** 1992. Evolution and ecology of influenza A viruses. Microbiological reviews **56:**152-179.
2. **Su S, Fu X, Li G, Kerlin F, Veit M.** 2017. Novel Influenza D virus: Epidemiology, pathology, evolution and biological characteristics. Virulence **8:**1580-1591.
3. **Medina RA, Garcia-Sastre A.** 2011. Influenza A viruses: new research developments. Nat Rev Microbiol **9:**590-603.
4. **Dou D, Revol R, Ostbye H, Wang H, Daniels R.** 2018. Influenza A Virus Cell Entry, Replication, Virion Assembly and Movement. Front Immunol **9:**1581.
5. **Paules C, Subbarao K.** 2017. Influenza. The Lancet **390:**697-708.
6. **Long JS, Mistry B, Haslam SM, Barclay WS.** 2019. Host and viral determinants of influenza A virus species specificity. Nat Rev Microbiol **17:**67-81.
7. **Zheng W, Tao YJ.** 2013. Structure and assembly of the influenza A virus ribonucleoprotein complex. FEBS letters **587:**1206-1214.
8. **Vahey MD, Fletcher DA.** 2019. Low-Fidelity Assembly of Influenza A Virus Promotes Escape from Host Cells. Cell **176:**281-294 e219.
9. **Harrison SC.** 2008. Viral membrane fusion. Nat Struct Mol Biol **15:**690-698.
10. **Pinto LH, Lamb RA.** 2006. The M2 proton channels of influenza A and B viruses. The Journal of biological chemistry **281:**8997-9000.
11. **Nayak DP, Hui EK, Barman S.** 2004. Assembly and budding of influenza virus. Virus Res **106:**147-165.
12. **Veit M, Thaa B.** 2011. Association of influenza virus proteins with membrane rafts. Adv Virol **2011:**370606.
13. **Noda T, Murakami S, Nakatsu S, Imai H, Muramoto Y, Shindo K, Sagara H, Kawaoka Y.** 2018. Importance of the 1+7 configuration of ribonucleoprotein complexes for influenza A virus genome packaging. Nature communications **9:**54.
14. **Rossman JS, Lamb RA.** 2011. Influenza virus assembly and budding. Virology **411:**229-236.
15. **Wilson IA, Skehel JJ, Wiley DC.** 1981. <1981_Wilson_Nat._HA structure.pdf>. Nature.
16. **Nobusawa E, Aoyama T, Kato H, Suzuki Y, Tateno Y, Nakajima K.** 1991. Comparison of complete amino acid sequences and receptor-binding properties among 13 serotypes of hemagglutinins of influenza A viruses. Virology **182:**475-485.
17. **Pleschka S.** 2013. Overview of influenza viruses. Current topics in microbiology and immunology **370:**1-20.
18. **Skehel JJ, Wiley DC.** 2000. Receptor Binding And Membrane Fusion In Virus Entry: The Influenza Hemagglutinin. Annu Rev Biochem.
19. **Garten W, Braden C, Arendt A, Peitsch C, Baron J, Lu Y, Pawletko K, Hardes K, Steinmetzer T, Bottcher-Friebertshauser E.** 2015. Influenza virus activating host proteases: Identification, localization and inhibitors as potential therapeutics. European journal of cell biology **94:**375-383.
20. **Manzoor R, Igarashi M, Takada A.** 2017. Influenza A Virus M2 Protein: Roles from Ingress to Egress. International journal of molecular sciences **18**.
21. **Schnell JR, Chou JJ.** 2008. Structure and mechanism of the M2 proton channel of influenza A virus. Nature **451:**591-595.
22. **Tian CL, Gao PF, Pinto LH, Lamb RA, Cross TA.** 2003. Initial structural and dynamic characterization of the M2 protein transmembrane and amphipathic helices in lipid bilayers. Protein Sci. **12:**2597-2605.
23. **Hatada E, Hasegawa M, Mukaigawa J, Shimizu K, Fukuda R.** 1989. CONTROL OF INFLUENZA-VIRUS GENE-EXPRESSION - QUANTITATIVE-ANALYSIS OF EACH VIRAL-RNA SPECIES IN INFECTED-CELLS. J. Biochem. **105:**537-546.
24. **Valcarcel J, Portela A, Ortin J.** 1991. REGULATED M1 MESSENGER-RNA SPLICING IN INFLUENZA VIRUS-INFECTED CELLS. J. Gen. Virol. **72:**1301-1308.

25. **Hull JD, Gilmore R, Lamb RA.** 1988. INTEGRATION OF A SMALL INTEGRAL MEMBRANE-PROTEIN, M2, OF INFLUENZA-VIRUS INTO THE ENDOPLASMIC-RETICULUM - ANALYSIS OF THE INTERNAL SIGNAL-ANCHOR DOMAIN OF A PROTEIN WITH AN ECTOPLASMIC NH2 TERMINUS. J. Cell Biol. **106:**1489-1498.
26. **Holsinger LJ, Lamb RA.** 1991. Influenza virus M2 integral membrane protein is a homotetramer stabilized by formation of disulfide bonds. Virology **183:**32-43.
27. **Castrucci MR, Hughes M, Calzoletti L, Donatelli I, Wells K, Takada A, Kawaoka Y.** 1997. The cysteine residues of the M2 protein are not required for influenza A virus replication. Virology **238:**128-134.
28. **Gerl MJ, Sampaio JL, Urban S, Kalvodova L, Verbavatz JM, Binnington B, Lindemann D, Lingwood CA, Shevchenko A, Schroeder C, Simons K.** 2012. Quantitative analysis of the lipidomes of the influenza virus envelope and MDCK cell apical membrane. J Cell Biol **196:**213-221.
29. **van Meer G, Voelker DR, Feigenson GW.** 2008. Membrane lipids: where they are and how they behave. Nature reviews. Molecular cell biology **9:**112-124.
30. **Lange Y.** 1991. Disposition of intracellular cholesterol in human fibroblasts. Journal of lipid research **32:**329-339.
31. **Simons K, van Meer G.** 1988. Lipid sorting in epithelial cells. Biochemistry **27:**6197-6202.
32. **Ackerman DG, Feigenson GW.** 2015. Lipid bilayers: clusters, domains and phases. Essays in biochemistry **57:**33-42.
33. **Subczynski WK, Pasenkiewicz-Gierula M, Widomska J, Mainali L, Raguz M.** 2017. High Cholesterol/Low Cholesterol: Effects in Biological Membranes: A Review. Cell biochemistry and biophysics **75:**369-385.
34. **Yang ST, Kreutzberger AJB, Lee J, Kiessling V, Tamm LK.** 2016. The role of cholesterol in membrane fusion. Chemistry and physics of lipids **199:**136-143.
35. **Harris R.** 2010. Cholesterol Binding and cholesterol Transport proteins. Subcell Biochem **51:**77-108.
36. **Li H, Papadopoulos V.** 1998. Peripheral-Type Benzodiazepine Receptor Function in Cholesterol Transport. Identification of a Putative Cholesterol Recognition/Interaction Amino Acid Sequence and Consensus Pattern. Endocrinology **139:**4991-4997.
37. **Vincent N, Genin C, Malvoisin E.** 2002. Identification of a conserved domain of the HIV-1 transmembrane protein gp41 which interacts with cholesteryl groups. Biochim Biophys Acta **1567:**157-164.
38. **Thaa B, Levental I, Herrmann A, Veit M.** 2011. Intrinsic membrane association of the cytoplasmic tail of influenza virus M2 protein and lateral membrane sorting regulated by cholesterol binding and palmitoylation. Biochem J **437:**389-397.
39. **C. S.** 2010. Chol binding viral Pros in virus entry and morphogenesis _Schroeder_2010.
40. **Baier CJ, Fantini J, Barrantes FJ.** 2011. Disclosure of cholesterol recognition motifs in transmembrane domains of the human nicotinic acetylcholine receptor. Scientific reports **1:**69.
41. **Song Y, Kenworthy AK, Sanders CR.** 2014. Cholesterol as a co-solvent and a ligand for membrane proteins. Protein science : a publication of the Protein Society **23:**1-22.
42. **Bukiya AN, Dopico AM.** 2017. Common structural features of cholesterol binding sites in crystallized soluble proteins. Journal of lipid research **58:**1044-1054.
43. **Barrett PJ, Song Y, Van Horn WD, Hustedt EJ, Schafer JM, Hadziselimovic A, Beel AJ, Sanders CR.** 2012. The amyloid precursor protein has a flexible transmembrane domain and binds cholesterol. Science **336:**1168-1171.
44. **Jamin N, Neumann JM, Ostuni MA, Vu TK, Yao ZX, Murail S, Robert JC, Giatzakis C, Papadopoulos V, Lacapere JJ.** 2005. Characterization of the cholesterol recognition amino acid consensus sequence of the peripheral-type benzodiazepine receptor. Molecular endocrinology **19:**588-594.

45. **Hanson MA, Cherezov V, Griffith MT, Roth CB, Jaakola VP, Chien EY, Velasquez J, Kuhn P, Stevens RC.** 2008. A specific cholesterol binding site is established by the 2.8 A structure of the human beta2-adrenergic receptor. Structure **16:**897-905.
46. **Bizebard T, Gigant B, Rigolet P, Rasmussen B, Diat O, Bosecke P, Wharton SA, Skehel JJ, Knossow M.** 1995. Structure of influenza virus haemagglutinin complexed with a neutralizing antibody. Nature **376:**92-94.
47. 1994. <1994_Wiley D.C_Nature_Structure of HA.pdf>. Nature.
48. **Calder LJ, Rosenthal PB.** 2016. Cryomicroscopy provides structural snapshots of influenza virus membrane fusion. Nat Struct Mol Biol **23:**853-858.
49. **Gui L, Ebner JL, Mileant A, Williams JA, Lee KK.** 2016. Visualization and Sequencing of Membrane Remodeling Leading to Influenza Virus Fusion. Journal of virology **90:**6948-6962.
50. **Ivanovic T, Choi JL, Whelan SP, van Oijen AM, Harrison SC.** 2013. Single particle viral fusion_Harrison_eLife. Elife **2:**e00333.
51. **Kemble GW, Danieli T, White JM.** 1994. Lipid-anchored influenza hemagglutinin promotes hemifusion, not complete fusion. Cell **76:**383-391.
52. **Armstrong RT, Kushnir AS, White JM.** 2000. The transmembrane domain of influenza hemagglutinin exhibits a stringent length requirement to support the hemifusion to fusion transition. J Cell Biol **151:**425-437.
53. **Li ZN, Lee BJ, Langley WA, Bradley KC, Russell RJ, Steinhauer DA.** 2008. Length requirements for membrane fusion of influenza virus hemagglutinin peptide linkers to transmembrane or fusion peptide domains. Journal of virology **82:**6337-6348.
54. **Benton DJ, Nans A, Calder LJ, Turner J, Neu U, Lin YP, Ketelaars E, Kallewaard NL, Corti D, Lanzavecchia A, Gamblin SJ, Rosenthal PB, Skehel JJ.** 2018. Influenza hemagglutinin membrane anchor. Proc Natl Acad Sci U S A **115:**10112-10117.
55. **Wagner R, Herwig A, Azzouz N, Klenk HD.** 2005. Acylation-mediated membrane anchoring of avian influenza virus hemagglutinin is essential for fusion pore formation and virus infectivity. Journal of virology **79:**6449-6458.
56. **Melikyan GB, Lin S, Roth MG, Cohen FS.** 1999. Amino acid sequence requirements of the transmembrane and cytoplasmic domains of influenza virus hemagglutinin for viable membrane fusion. Molecular biology of the cell **10:**1821-1836.
57. **Kozerski C, Ponimaskin E, Schroth-Diez B, Schmidt MF, Herrmann A.** 2000. Modification of the cytoplasmic domain of influenza virus hemagglutinin affects enlargement of the fusion pore. Journal of virology **74:**7529-7537.
58. **Takeda M, Lamb, R.A.** 2003. Influenza virus hemagglutinin concentrates in lipid raft microdomains for efficient viral fusion. Journal of virology.
59. **Sun X, Whittaker GR.** 2003. Role for Influenza Virus Envelope Cholesterol in Virus Entry and Infection. Journal of virology **77:**12543-12551.
60. **Chlanda P, Mekhedov E, Waters H, Schwartz CL, Fischer ER, Ryham RJ, Cohen FS, Blank PS, Zimmerberg J.** 2016. The hemifusion structure induced by influenza virus haemagglutinin is determined by physical properties of the target membranes. Nature Microbiology **1:**16050.
61. **Domanska MK, Wrona D, Kasson PM.** 2013. Multiphasic effects of cholesterol on influenza fusion kinetics reflect multiple mechanistic roles. Biophysical journal **105:**1383-1387.
62. **Domanska MK, Dunning RA, Dryden KA, Zawada KE, Yeager M, Kasson PM.** 2015. Hemagglutinin Spatial Distribution Shifts in Response to Cholesterol in the Influenza Viral Envelope. Biophysical journal **109:**1917-1924.
63. **Biswas S, Yin SR, Blank PS, Zimmerberg J.** 2008. Cholesterol promotes hemifusion and pore widening in membrane fusion induced by influenza hemagglutinin. J Gen Physiol **131:**503-513.

64. **Cady SD, Schmidt-Rohr K, Wang J, Soto CS, Degrado WF, Hong M.** 2010. Structure of the amantadine binding site of influenza M2 proton channels in lipid bilayers. Nature **463:**689-692.
65. **Sharma M, Yi M, Dong H, Qin H, Peterson E, Busath DD, Zhou HX, Cross TA.** 2010. Insight into the mechanism of the influenza A proton channel from a structure in a lipid bilayer. Science **330:**509-512.
66. **Stouffer AL, Acharya R, Salom D, Levine AS, Di Costanzo L, Soto CS, Tereshko V, Nanda V, Stayrook S, DeGrado WF.** 2008. Structural basis for the function and inhibition of an influenza virus proton channel. Nature **451:**596-599.
67. **Hong M, DeGrado WF.** 2012. Structural basis for proton conduction and inhibition by the influenza M2 protein. Protein science : a publication of the Protein Society **21:**1620-1633.
68. **Tobler K, Roberts KL.** 1999. Effect of Cytoplasmic Tail Truncations on the Activity of the M2 Ion Channel of Influenza A Virus. J Virol.
69. **Kwon B, Tietze D, White PB, Liao SY, Hong M.** 2015. Chemical ligation of the influenza M2 protein for solid-state NMR characterization of the cytoplasmic domain. Protein science : a publication of the Protein Society **24:**1087-1099.
70. **Ma C, Polishchuk AL, Ohigashi Y, Stouffer AL, Schon A, Magavern E, Jing X, Lear JD, Freire E, Lamb RA, DeGrado WF, Pinto LH.** 2009. Identification of the functional core of the influenza A virus A/M2 proton-selective ion channel. Proceedings of the National Academy of Sciences of the United States of America **106:**12283-12288.
71. **Roberts KL, Leser GP, Ma C, Lamb RA.** 2013. The amphipathic helix of influenza A virus M2 protein is required for filamentous bud formation and scission of filamentous and spherical particles. J Virol **87:**9973-9982.
72. **Zebedee SL, Lamb RA.** 1988. Influenza A virus M2 protein: monoclonal antibody restriction of virus growth and detection of M2 in virions. J Virol **62:**2762-2772.
73. **Scheiffele P, Rietveld A, Wilk T, Simons K.** 1999. Influenza viruses select ordered lipid domains during budding from the plasma membrane. J. Biol. Chem. **274:**2038-2044.
74. **Ono A, Freed EO.** 2001. Plasma membrane rafts play a critical role in HIV-1 assembly and release. Proc Natl Acad Sci U S A **98:**13925-13930.
75. **Engel S, Scolari S, Thaa B, Krebs N, Korte T, Herrmann A, Veit M.** 2010. FLIM-FRET and FRAP reveal association of influenza virus haemagglutinin with membrane rafts. Biochem J **425:**567-573.
76. **Hess ST, Gould TJ, Gudheti MV, Maas SA, Mills KD, Zimmerberg J.** 2007. Dynamic clustered distribution of hemagglutinin resolved at 40 nm in living cell membranes discriminates between raft theories. Proc Natl Acad Sci U S A **104:**17370-17375.
77. **Leser GP, Lamb RA.** 2017. Lateral Organization of Influenza Virus Proteins in the Budozone Region of the Plasma Membrane. Journal of virology.
78. **Chen BJ, Leser GP, Morita E, Lamb RA.** 2007. Influenza virus hemagglutinin and neuraminidase, but not the matrix protein, are required for assembly and budding of plasmid-derived virus-like particles. Journal of virology **81:**7111-7123.
79. **Engel S, de Vries M, Herrmann A, Veit M.** 2012. Mutation of a raft-targeting signal in the transmembrane region retards transport of influenza virus hemagglutinin through the Golgi. FEBS Lett **586:**277-282.
80. **de Vries M, Herrmann A, Veit M.** 2015. A cholesterol consensus motif is required for efficient intracellular transport and raft association of a group 2 HA from influenza virus. Biochem J **465:**305-314.
81. **Nayak DP, Barman S.** 2002. Role of lipid rafts in virus assembly and budding, p. 1-28. *In* Maramorosch K, Murphy FA, Shatkin AJ (ed.), Advances in Virus Research, Vol 58, vol. 58. Elsevier Academic Press Inc, San Diego.

82. **Tall RD, Alonso MA, Roth MG.** 2003. Features of influenza HA required for apical sorting differ from those required for association with DRMs or MAL. Traffic **4:**838-849.
83. **Lin SS, Naim HY, Rodriguez AC, Roth MG.** 1998. Mutations in the middle of the transmembrane domain reverse the polarity of transport of the influenza virus hemagglutinin in MDCK epithelial cells. J. Cell Biol. **142:**51-57.
84. **Barman S, Adhikary L, Kawaoka Y, Nayak DP.** 2003. Influenza A virus hemagglutinin containing basolateral localization signal does not alter the apical budding of a recombinant influenza A virus in polarized MDCK cells. Virology **305:**138-152.
85. **Mora R, Rodriguez-Boulan E, Palese P, Garcia-Sastre A.** 2002. Apical budding of a recombinant influenza A virus expressing a hemagglutinin protein with a basolateral localization signal. Journal of virology **76:**3544-3553.
86. **Zhang J, Pekosz A, Lamb RA.** 2000. Influenza virus assembly and lipid raft microdomains: a role for the cytoplasmic tails of the spike glycoproteins. Journal of virology **74:**4634-4644.
87. **Jin H, Leser GP, Zhang J, Lamb RA.** 1997. Influenza virus hemagglutinin and neuraminidase cytoplasmic tails control particle shape. Embo Journal **16:**1236-1247.
88. **Thaa B, Herrmann A, Veit M.** 2010. Intrinsic Cytoskeleton-Dependent Clustering of Influenza Virus M2 Protein with Hemagglutinin Assessed by FLIM-FRET. Journal of Virology **84:**12445-12449.
89. **Rossman JS, Jing X, Leser GP, Lamb RA.** 2010. Influenza virus M2 protein mediates ESCRT-independent membrane scission. Cell **142:**902-913.
90. **McCown MF, Pekosz A.** 2006. Distinct domains of the influenza a virus M2 protein cytoplasmic tail mediate binding to the M1 protein and facilitate infectious virus production. J Virol **80:**8178-8189.
91. **Iwatsuki-Horimoto K, Horimoto T, Noda T, Kiso M, Maeda J, Watanabe S, Muramoto Y, Fujii K, Kawaoka Y.** 2006. The cytoplasmic tail of the influenza A virus M2 protein plays a role in viral assembly. J Virol **80:**5233-5240.
92. **Chen BJ, Leser GP, Jackson D, Lamb RA.** 2008. The influenza virus M2 protein cytoplasmic tail interacts with the M1 protein and influences virus assembly at the site of virus budding. J Virol **82:**10059-10070.
93. **Enami M, Enami K.** 1996. Influenza virus hemagglutinin and neuraminidase glycoproteins stimulate the membrane association of the matrix protein. Journal of virology **70:**6653-6657.
94. **Zhang J, Lamb RA.** 1996. Characterization of the membrane association of the influenza virus matrix protein in living cells. Virology **225:**255-266.
95. **Schroeder C, Heider H, Moncke-Buchner E, Lin TI.** 2005. The influenza virus ion channel and maturation cofactor M2 is a cholesterol-binding protein. Eur Biophys J **34:**52-66.
96. **Thaa B, Tielesch C, Moller L, Schmitt AO, Wolff T, Bannert N, Herrmann A, Veit M.** 2012. Growth of influenza A virus is not impeded by simultaneous removal of the cholesterol-binding and acylation sites in the M2 protein. J Gen Virol **93:**282-292.
97. **Elkins MR, Hong M.** 2017. Cholesterol-binding site of the influenza M2 protein in lipid bilayers from solid-state NMR. Proc Natl Acad Sci U S A.
98. **Rossman JS, Jing X, Leser GP, Balannik V, Pinto LH, Lamb RA.** 2010. Influenza virus m2 ion channel protein is necessary for filamentous virion formation. J Virol **84:**5078-5088.
99. **Stewart SM, Pekosz A.** 2011. Mutations in the membrane-proximal region of the influenza A virus M2 protein cytoplasmic tail have modest effects on virus replication. J Virol **85:**12179-12187.
100. **Martyna A, Bahsoun B, Badham MD, Srinivasan S, Howard MJ, Rossman JS.** 2017. Membrane remodeling by the M2 amphipathic helix drives influenza virus membrane scission. Sci Rep **7:**44695.

101. **Wang T, Cady SD, Hong M.** 2012. NMR determination of protein partitioning into membrane domains with different curvatures and application to the influenza M2 peptide. Biophysical journal **102:**787-794.
102. **Drin G, Antonny B.** 2010. Amphipathic helices and membrane curvature. FEBS Lett **584:**1840-1847.
103. **Antonny B.** 2011. Mechanisms of membrane curvature sensing. Annu Rev Biochem **80:**101-123.
104. **Horvath CA, Vanden Broeck D, Boulet GA, Bogers J, De Wolf MJ.** 2007. Epsin: inducing membrane curvature. Int J Biochem Cell Biol **39:**1765-1770.
105. **Ford MG, Mills IG, Peter BJ, Vallis Y, Praefcke GJ, Evans PR, McMahon HT.** 2002. Curvature of clathrin-coated pits driven by epsin. Nature **419:**361- 366.
106. **J. B, Antonny B.** 2005. ArfGAP1 responds to membrane curvature through the folding of a lipid packing sensor motif. EMBO J.
107. **Murriel CL, Dowdy SF.** 2006. Influence of protein transduction domains on intracellular delivery of macromolecules. Expert Opin Drug Deliv **3:**739-746.
108. **Frankel AD, Pabo CO.** 1988. Cellular uptake of the tat protein from human immunodeficiency virus. Cell **55:**1189-1193.
109. **Green M, Loewenstein PM.** 1988. Autonomous functional domains of chemically synthesized human immunodeficiency virus tat trans-activator protein. Cell **55:**1179-1188.
110. **Palm-Apergi C, Lonn P, Dowdy SF.** 2012. Do cell-penetrating peptides actually "penetrate" cellular membranes? Mol Ther **20:**695-697.
111. **Maniti O, Piao HR, Ayala-Sanmartin J.** 2014. Basic cell penetrating peptides induce plasma membrane positive curvature, lipid domain separation and protein redistribution. Int J Biochem Cell Biol **50:**73-81.
112. **Lamaziere A, Burlina F, Wolf C, Chassaing G, Trugnan G, Ayala-Sanmartin J.** 2007. Non-metabolic membrane tubulation and permeability induced by bioactive peptides. PLoS One **2:**e201.
113. **Schindelin J, Arganda-Carreras I, Frise E, Kaynig V, Longair M, Pietzsch T, Preibisch S, Rueden C, Saalfeld S, Schmid B, Tinevez JY, White DJ, Hartenstein V, Eliceiri K, Tomancak P, Cardona A.** 2012. Fiji: an open-source platform for biological-image analysis. Nature methods **9:**676-682.
114. **Rodriguez-Boulan E, Paskiet KT, Salas PJ, Bard E.** 1984. Intracellular transport of influenza virus hemagglutinin to the apical surface of Madin-Darby canine kidney cells. J Cell Biol **98:**308-319.
115. **Eisenberg D, Weiss RM, Terwilliger TC.** 1982. The helical hydrophobic moment: a measure of the amphiphilicity of a helix. Nature **299:**371-374.
116. **Beale R, Wise H, Stuart A, Ravenhill BJ, Digard P, Randow F.** 2014. A LC3-interacting motif in the influenza A virus M2 protein is required to subvert autophagy and maintain virion stability. Cell host & microbe **15:**239-247.
117. **Lamb RA, Zebedee SL, Richardson CD.** 1985. Influenza virus M2 protein is an integral membrane protein expressed on the infected-cell surface. Cell **40:**627-633.
118. **Wang D, Harmon A, Jin J, Francis DH, Christopher-Hennings J, Nelson E, Montelaro RC, Li F.** 2010. The lack of an inherent membrane targeting signal is responsible for the failure of the matrix (M1) protein of influenza A virus to bud into virus-like particles. Journal of virology **84:**4673-4681.
119. **Wilson RL, Frisz JF, Klitzing HA, Zimmerberg J, Weber PK, Kraft ML.** 2015. Hemagglutinin clusters in the plasma membrane are not enriched with cholesterol and sphingolipids. Biophysical journal **108:**1652-1659.
120. **Frisz JF, Lou K, Klitzing HA, Hanafin WP, Lizunov V, Wilson RL, Carpenter KJ, Kim R, Hutcheon ID, Zimmerberg J, Weber PK, Kraft ML.** 2013. Direct chemical evidence for sphingolipid domains in the plasma membranes of fibroblasts. Proc Natl Acad Sci U S A **110:**E613-622.

121. **Hess ST, Kumar M, Verma A, Farrington J, Kenworthy A, Zimmerberg J.** 2005. Quantitative electron microscopy and fluorescence spectroscopy of the membrane distribution of influenza hemagglutinin. J Cell Biol **169:**965-976.
122. **Siche S, Brett K, Moller L, Kordyukova LV, Mintaev RR, Alexeevski AV, Veit M.** 2015. Two Cytoplasmic Acylation Sites and an Adjacent Hydrophobic Residue, but No Other Conserved Amino Acids in the Cytoplasmic Tail of HA from Influenza A Virus Are Crucial for Virus Replication. Viruses **7:**6458-6475.
123. **Schuck S, Simons K.** 2004. Polarized sorting in epithelial cells: raft clustering and the biogenesis of the apical membrane. Journal of cell science **117:**5955-5964.
124. **Keller P, Simons K.** 1998. Cholesterol is required for surface transport of influenza virus hemagglutinin. J. Cell Biol. **140:**1357-1367.
125. **Brugger B, Glass B, Haberkant P, Leibrecht I, Wieland FT, Krausslich HG.** 2006. The HIV lipidome: a raft with an unusual composition. Proc Natl Acad Sci U S A **103:**2641-2646.
126. **Harris A, Cardone G, Winkler DC, Heymann JB, Brecher M, White JM, Steven AC.** 2006. Influenza virus pleiomorphy characterized by cryoelectron tomography. Proc Natl Acad Sci U S A **103:**19123-19127.
127. **Moules V, Terrier O, Yver M, Riteau B, Moriscot C, Ferraris O, Julien T, Giudice E, Rolland JP, Erny A, Bouscambert-Duchamp M, Frobert E, Rosa-Calatrava M, Pu Lin Y, Hay A, Thomas D, Schoehn G, Lina B.** 2011. Importance of viral genomic composition in modulating glycoprotein content on the surface of influenza virus particles. Virology **414:**51-62.
128. **Anderson RG, Jacobson K.** 2002. A role for lipid shells in targeting proteins to caveolae, rafts, and other lipid domains. Science **296:**1821-1825.
129. **Jacobson K, Mouritsen OG, Anderson RG.** 2007. Lipid rafts: at a crossroad between cell biology and physics. Nature cell biology **9:**7-14.
130. **Chen BJ, Takeda M, Lamb RA.** 2005. Influenza virus hemagglutinin (H3 subtype) requires palmitoylation of its cytoplasmic tail for assembly: M1 proteins of two subtypes differ in their ability to support assembly. Journal of virology **79:**13673-13684.
131. **Chlanda P, Mekhedov E, Waters H, Sodt A, Schwartz C, Nair V, Blank PS, Zimmerberg J.** 2017. Palmitoylation Contributes to Membrane Curvature in Influenza A Virus Assembly and Hemagglutinin-Mediated Membrane Fusion. Journal of virology **91**.
132. **Ge M, Freed JH.** 2011. Two conserved residues are important for inducing highly ordered membrane domains by the transmembrane domain of influenza hemagglutinin. Biophysical journal **100:**90-97.
133. **Boonstra S, Blijleven JS, Roos WH, Onck PR, van der Giessen E, van Oijen AM.** 2018. Hemagglutinin-Mediated Membrane Fusion: A Biophysical Perspective. Annual review of biophysics **47:**153-173.
134. **Zawada KE, Wrona D, Rawle RJ, Kasson PM.** 2016. Influenza viral membrane fusion is sensitive to sterol concentration but surprisingly robust to sterol chemical identity. Sci Rep **6:**29842.
135. **Chernomordik LV, Kozlov MM.** 2003. Protein-lipid interplay in fusion and fission of biological membranes. Annu Rev Biochem **72:**175-207.
136. **Zimmerberg J, Kozlov MM.** 2006. How proteins produce cellular membrane curvature. Nature reviews. Molecular cell biology **7:**9-19.
137. **Vigant F, Santos NC, Lee B.** 2015. Broad-spectrum antivirals against viral fusion. Nat Rev Microbiol **13:**426-437.
138. **Tripathi S, Pohl MO, Zhou Y, Rodriguez-Frandsen A, Wang G, Stein DA, Moulton HM, DeJesus P, Che J, Mulder LC, Yanguez E, Andenmatten D, Pache L, Manicassamy B, Albrecht RA, Gonzalez MG, Nguyen Q, Brass A, Elledge S, White M, Shapira S, Hacohen N, Karlas A, Meyer TF, Shales M, Gatorano A, Johnson JR, Jang G, Johnson T, Verschueren E, Sanders D, Krogan N, Shaw M, Konig R, Stertz S, Garcia-Sastre A, Chanda SK.** 2015. Meta- and Orthogonal

Integration of Influenza "OMICs" Data Defines a Role for UBR4 in Virus Budding. Cell host & microbe **18:**723-735.

139. **Zhu P, Liang L, Shao X, Luo W, Jiang S, Zhao Q, Sun N, Zhao Y, Li J, Wang J, Zhou Y, Zhang J, Wang G, Jiang L, Chen H, Li C.** 2017. Host Cellular Protein TRAPPC6ADelta Interacts with Influenza A Virus M2 Protein and Regulates Viral Propagation by Modulating M2 Trafficking. Journal of virology **91**.
140. **Wohlgemuth N, Lane AP, Pekosz A.** 2018. Influenza A Virus M2 Protein Apical Targeting Is Required for Efficient Virus Replication. J Virol **92**.
141. **Curthoys NM, Mlodzianoski MJ, Parent M, Butler MB, Raut P, Wallace J, Lilieholm J, Mehmood K, Maginnis MS, Waters H, Busse B, Zimmerberg J, Hess ST.** 2019. Influenza Hemagglutinin Modulates Phosphatidylinositol 4,5-Bisphosphate Membrane Clustering. Biophysical journal **116:**893-909.

Publications

1) **Hu B**, Siche S, Möller L, Veit M. 2019. Amphipathic helices of cellular proteins can replace the helix in M2 of Influenza A virus with only small effects on virus replication. **(In revision)**

2) **Hu B**, Hofer CT, Thiele C, Veit M. 2019. Cholesterol binding to the transmembrane region of a group 2 HA of Influenza virus is essential for virus replication affecting both virus assembly and HA's fusion activity. **Journal of virology**.

3) **Hu B**, Du T, Li C, Luo S, Liu Y, Huang X, Hu Q. 2015. Sensitivity of transmitted and founder human immunodeficiency virus type 1 envelopes to carbohydrate-binding agents griffithsin, cyanovirin-N and Galanthus nivalis agglutinin. **J Gen Virol** 96:3660-3666.

4) Wang P, Hu K, Luo S, Zhang M, Deng X, Li C, Jin W, **Hu B**, He S, Li M, Du T, Xiao G, Zhang B, Liu Y, Hu Q. 2016. DC-SIGN as an attachment factor mediates Japanese encephalitis virus infection of human dendritic cells via interaction with a single high-mannose residue of viral E glycoprotein. **Virology** 488:108-119.

5) Li C, Guan X, Du T, Jin W, Wu B, Liu Y, Wang P, **Hu B**, Griffin GE, Shattock RJ, Hu Q. 2015. Inhibition of HIV-1 infection of primary CD4+ T-cells by gene editing of CCR5 using adenovirus-delivered CRISPR/Cas9. **J Gen Virol** 96:2381-2393.

6) Liu Y, Luo S, He S, Zhang M, Wang P, Li C, Huang W, **Hu B**, Griffin GE, Shattock RJ, Hu Q. 2015. Tetherin restricts HSV-2 release and is counteracted by multiple viral glycoproteins. **Virology** 475:96-109.

Acknowledgements

Quick as always four years of my PhD study is coming to an end. Along the way I have received many help, support and caring from different people, to whom I need to express my appreciation.

I would like to express my deep gratitude to my supervisor, Dr. Michael Veit. He has guided and supported me all the way from planning the research project until finishing the thesis. With much knowledge and experience, he always offered useful suggestions whenever I had problems with my research work. I have learned a lot from him and obtained much knowledge during my study. I would also like to thank my second supervisor Dr. Benedikt Kaufter and my mentor Dr. Kasten Tedin for their supports, enthusiasm in each discussion and valuable suggestions.

I am particularly grateful to Dr. Kai Ludwig for performing negative staining electronic microscopy and Dr. Lars Möller for transmission electronic microscopy.

I greatly appreciate the assistance from all the members in Dr. Veit's lab. Thanks to Dr. Chris Höfer for her unselfish support and guidance during her three years in the lab. Thanks to Dr. Ludwig Krabben, Dr. Susanne Kaufer, Dr. Minze Zhang, PhD students Xuejiao Han, Mohamed Rasheed Gadalla, Atika Hadiati for all the discussions in each lab meeting and daily work. Thanks to technician Mrs. Elke Dyrks and Mrs. Angelika Thomele for their supportive work in the lab. We have shared four years of bitter and happy life and they are going to be a treasure of my memory.

I would also like to extend my thanks to all the members of Institute of Virology for their suggestions and assistance in work. Thanks to Prof. Klaus Osterrieder and PD. Kerstin Borchers for hosting me in the institute. Thanks to Darren and Oleksandr for the help in confocal microscopy and to Kathrin and Nicole for the help in RT-qPCR. Thanks to Ahmed, Anirban, Cosima, Dusan, Ibrahim, Jakob, Luca, Mohamed Kamel, Na, Pavulraj, Renato, Tereza, Timo, Viviane, Walid and Yu. Thanks to technicians Annett, Ann and Michaela, secretary Kia and some others.

I want to express my special thanks to the support from my friends, my brother and my most important parents. Life stays colorful knowing that you are always there.

Lastly, I owe my appreciation to the China Scholarship Coucil (CSC). Without their financial assistance, I could not pursue my study in Berlin from the beginning.

Selbständigkeitserklärung

Hiermit bestätige ich, dass ich die vorliegende Arbeit selbständig angefertigt habe. Ich versichere, dass ich ausschließlich die angegebenen Quellen und Hilfen Anspruch genommen habe.

Berlin, am 22.08.2019

Bodan HU